UNIVERSITY OF CALIFORNIA
RIVERSIDE

Thermal and Electronic Transport in Graphene-Based Nanostructures and Applications in Electrical Sensors

A Dissertation submitted in partial satisfaction
of the requirements for the degree of

Doctor of Philosophy

in

Chemical and Environmental Engineering

by

Pankaj Ghanshyam Ramnani

December 2016

Dissertation Committee:
Dr. Ashok Mulchandani, Chairperson
Dr. Philip Christopher
Dr. Ruoxue Yan

The Dissertation of Pankaj Ghanshyam Ramnani is approved:

_____

_____

_____

Committee Chairperson

University of California, Riverside

ACKNOWLEDGEMENTS

I thank my adviser, Professor Ashok Mulchandani, for accepting me into his research group and being the best mentor I could have wished for during my PhD. I am deeply grateful to him for the time he has invested in me, his guidance and constructive suggestions, which have significantly helped me to grow as a researcher during the last four years. His commitment and diligence have had a great influence on me and without his support this thesis could never be materialized. I would also like to extend my gratitude to my thesis committee members, Dr. Philip Christopher and Dr. Ruoxue Yan, for their kind encouragements and advices. I acknowledge the support and guidance from Professor Roger Lake and Professor Alexander Balandin for allowing me to collaborate with their research groups and the valuable discussions on our collaborative research projects.

I am thankful to all my labmates and colleagues−Tapan Sarkar, Nuvia Saucedo, Yingning Gao, Trupti Terse, Thien-Toan Tran, Tung Pham, Claudia Chaves, Xuejun Yu, Hui Wang, Mahesh Neupane and Hoda Malekpour for their collaborations and discussions. Dr. Tapan Sarkar and Dr. Yingning Gao, I thank you for the all the help and training at the beginning of my PhD. Dr. Nuvia Saucedo, thank you being a great friend and colleague. Your friendship and support made the four years of graduate school much easier. Thien-Toan Tran, our insightful discussions over coffee really helped me direct my research and it is something I will cherish for a long time. Tung Pham, I admire your dedication and work ethic. I have learnt a lot from you. I cannot enumerate all of the friendships that I have developed over the last few years but a special mention goes to Indrajeet Singh,

Anumeha Bhaskar, Samarthya Bhagia and Abhishek Patri. I would also like to thank my tennis and football group of friends for helping me stay active and providing the much needed stress relief.

I am grateful to the Center for Nanoscale Science and Engineering (CNSE) facility, Central Facility for Advanced Microscopy and Microanalysis (CFAMM) and Analytical Chemistry Instrumentation Facility (ACIF) at UC Riverside for providing me the scope to develop hands-on skills in semiconductor processing technology. I also appreciate help of Mark Heiden, Dexter Humphrey, Dong Yan and Frank Lee in training with all the tools in the Cleanroom.

Lastly, I would like to thank my parents and my brother, Manan, for all their continuous support throughout my life. I am deeply indebted to you for all the sacrifices you have made and the patience and confidence you shown in me.

The text of this dissertation, in part or in full, is a reprint of the material as it appears in: “Thermal conductivity of graphene with defects induced by electron beam irradiation”, Nanoscale 2016; “Carbon nanomaterial-based electrochemical biosensors for label-free sensing of environmental pollutants”, Chemosphere 2016; “Electronic detection of microRNA at attomolar level with high specificity”, Analytical Chemistry 2013; and “An oligonucleotide-functionalized carbon nanotube chemiresistor for sensitive detection of mercury in saliva” Analyst 2016. The co-author Dr. Ashok Mulchandani listed in all of these publications directed and supervised the research which forms the basis for this dissertation.

Dedication

To my parents

Ghanshyam and Sonu Ramnani

ABSTRACT OF THE DISSERTATION

Thermal and Electronic Transport in Graphene-based Nanostructures and Applications in Electrical Sensors

by

Pankaj Ghanshyam Ramnani

Doctor of Philosophy, Graduate Program in Chemical and Environmental Engineering
University of California, Riverside, December 2016
Professor Ashok Mulchandani, Chairperson

It is a general consensus that silicon metal–oxide–semiconductor FET (MOSFET) is approaching its scaling limits due to issues including high power dissipation, short channel effects and degraded electrostatics. In recent years, a significant amount of research has been directed towards exploring novel materials like graphene and other two-dimensional atomic crystals to replace Si. Graphene is an ideal candidate owing to its exceptional properties including high carrier mobility (exceeding 15,000 $cm^2 V^{-1} s^{-1}$), high charge carrier concentration (~10^{12} cm^{-2}), low contact resistance due to tunable fermi level, excellent thermal conductivity (~5000W $m^{-1} K^{-1}$), optical transparency (~97.7%) and flexibility. Despite all these intriguing properties, the absence of a bandgap in graphene has limited its potential applications owing to large off-state currents and low I_{on}/I_{off} ratios observed in graphene-based field effect transistors (FETs). Additionally, most of these experimental studies are conducted using pristine graphene isolated by mechanical exfoliation of graphite, which is not a practical approach for large scale synthesis of graphene.

In this dissertation, a scalable method of synthesizing high quality single-layer and bilayer graphene was developed using ambient pressure chemical vapor deposition (AP-CVD). The crystalline nature and physical properties were characterized using electron microscopy and spectroscopic techniques. We investigated the effects of point defects—typically introduced during material characterization and device fabrication steps—on thermal transport in CVD grown single-layer graphene. Furthermore, we investigated methods to engineer a bandgap in graphene by nanopatterning graphene into pseudo one-dimensional nanostructures called graphene nanoribbons (GNRs) using two different top-down approaches. The edge defects in GNRs, which limit carrier mobility and induce p-doping, were characterized using Raman spectroscopy and x-ray photoelectron spectroscopy (XPS), and thermal treatments to repair these defects were explored. Finally, the applications of these graphene-based nanostructures as FET-based electrical nano chemical/bio-sensors were explored. The GNR-FET device showed a significant increase in sensitivity for detection of NO_2 as compared to its graphene counterpart. Analogous to GNRs, single-walled carbon nanotubes (SWNTs) based chemiresistive sensors were also developed for detection of microRNA, a cancer biomarker, and detection of mercury ions in saliva samples.

CONTENTS

CHAPTER 4

BAND-GAP ENGINEERING OF GRAPHENE

CHAPTER 5

APPLICATIONS OF CARBON NANOTUBES AS FET/CHEMIRESISTIVE BASED ELECTRICAL BIOSENSORS

List of Figures

CHAPTER 1

Introduction: Graphene-based nanomaterials

1.1. Issues with scaling of Silicon-based devices

The classic metal–oxide–semiconductor field-effect transistor (MOSFET) has been the workhorse of the semiconductor industry.[1,2] Interestingly, the basic building block of all digital integrated circuits (ICs) including microprocessors and memory chips, is just one single semiconductor, Si, and one single transistor type, the Si MOSFET. A typical n-channel MOSFET device, shown in Fig. 1.1, consists of two n-type semiconductor regions called the source and the drain, which are separated by a region of p-type semiconductor called the substrate. A thin layer of insulating material, typically silicon dioxide, covers the region between source and drain, and this layer is topped by a metal electrode called the gate. Under typical bias conditions, the source and the p-type substrate are grounded, and a positive voltage is applied to the drain. Under these conditions, the drain p–n junction is reverse biased, and no current flows between the drain and the substrate. Because the bias

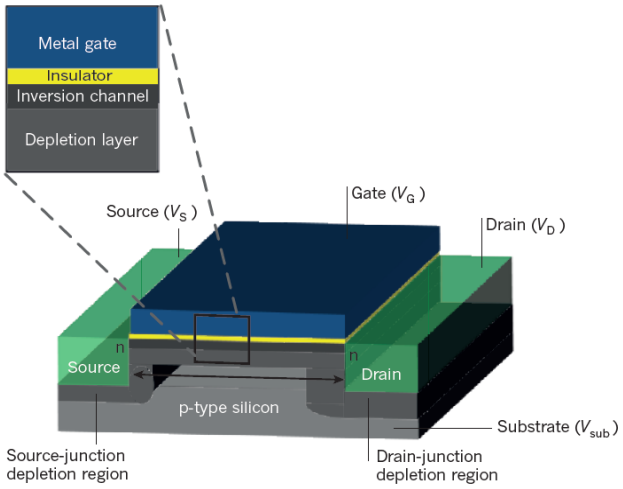

Figure 1.1. A schematic view of a classical bulk n-channel MOSFET.[1]

across the source p–n junction is zero, there is also no current flowing from the substrate to the source. As a result, there is no current flow between the source and the drain, and the transistor is turned off. When a large enough positive voltage is applied to the gate, then electrons spill out of the n-type semiconductor source and drain regions, forming an electron-rich layer, called the channel, underneath the gate oxide. The channel forms a continuous electron bridge between the source and the drain causing current to flow between these two electrodes and the transistor is then turned on.[1,3]

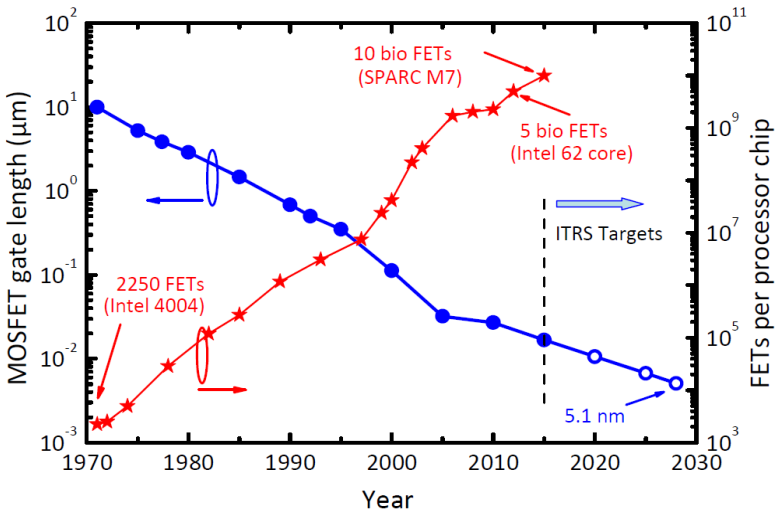

Figure 1.2. Evolution of MOSFET gate length and number of MOSFETs integrated on a single microprocessor chip.[3,35]

The ever-growing demands for faster and cheaper microprocessors have been the driving force for development of new and improved materials, processes and design methodologies that allow for progressive miniaturization of transistors and increasing the transistor density.[3-6] Keeping the chip size constant, reducing the transistor size allows for increase in density of transistors and thereby increase in functionality of the circuit. For example, a modern microprocessor typically contains over than 2 billion MOSFETs

assembled on a chip area no larger than a few square centimeters, and a 32-gigabyte memory card weighing only 0.5 g contains a staggering 256 billion transistors.[1] As shown in Fig. 1.2, the last two decades have witnessed tremendous advancements in the field of electronic devices, with characteristic dimensions of devices shrinking past the microscale and down into the nanoscale regime. In a classic paper by Gordon Moore published in 1965,[7] he predicted that the density of transistors on a chip would double every 18 months. Though empirical, Moore's law has held remarkably well for the past 45 years. This trend of continuous device miniaturization and increasing circuit complexity is called Moore's Law.

1.1.1. Thermal management issues

After many years of successful scaling, it is now becoming increasingly difficult to achieve the required performance improvements by shrinking the Si MOSFET. The enhancement of computing capabilities by escalating the transistor density comes at the cost of increasing power dissipation across the device.[8-11] These issues are evident at the individual microprocessor (CPU) level that operate at a frequency of few GHz (Fig. 1.3), where the typical dissipated power has reached 100 W cm^{-2},[10] an order of magnitude higher than a typical hot plate. Fig. 1.4 shows the average temperature rise for generic bulk and

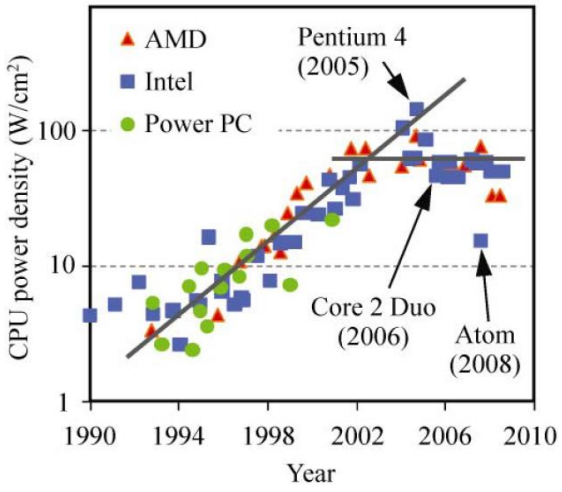

Figure 1.3. Near-exponential increase of CPU power density in recent decades has flattened with the introduction of multi-core CPUs.[9]

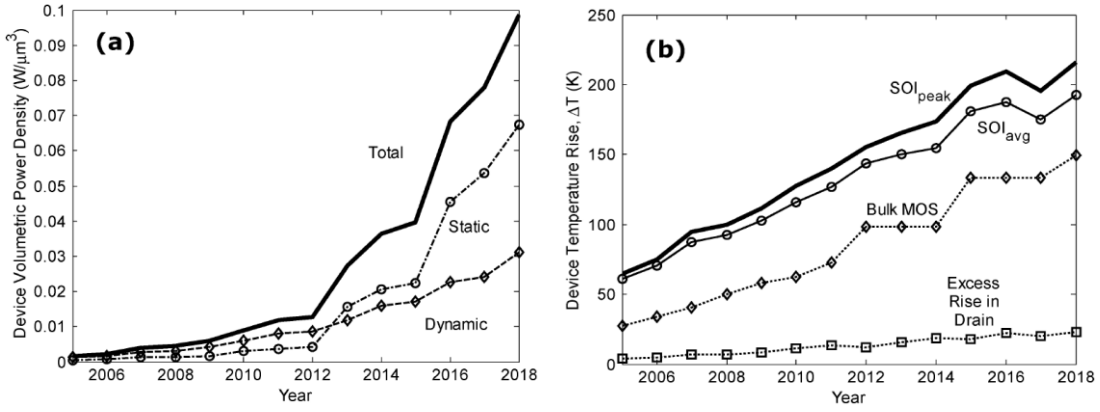

Figure 1.4. (a) Power dissipated per unit volume in a device. **(b)** Average temperature rise in a device under saturation conditions shown for generic bulk and silicon-on-insulator MOSFETs.[9]

silicon-on-insulator MOSFETs operating under saturation conditions. These power-dense regions can produce localized hot-spots – regions where local temperatures are significantly higher than the average device temperature and the size of these hot spots may range anywhere from ~500 μm^2 up to ~5 mm^2.[10,12-14] Hot-spot formation can cause degradation of drain current, gain in output power, as well as an increase in the gate-leakage current and poor reliability of ICs. Additionally, such electronic power and thermal issues also have a negative impact on new and upcoming applications like wearable devices, medical instrumentation, and portable electronics. For portable devices there is a basic trade-off between the available functionality and the need to carry heavy batteries to power it. Hence, in order to minimize the influence of these hot spots on the device performance and to keep up with the scaling trend, it is has become increasingly desirable to have efficient heat spreading capabilities at both the 'local' single transistor device level as well as at the global packaging levels.

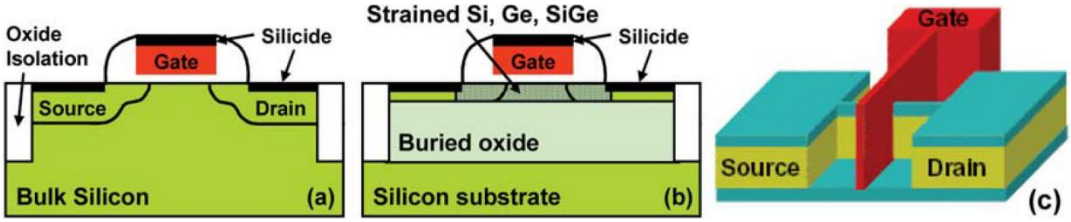

Figure 1.5. Evolution of transistor designs from: (a) bulk silicon (b) to (strained) silicon or germanium on insulator to (c) multiple-gate or FinFET devices.[9]

The evolution of transistor designs from the conventional bulk silicon transistor to the more recent three-dimensional FINFETs is shown in Fig. 1.7[10,15]. However, irrespective of the device architecture, these transistors typically incorporate only a few materials into the transistor design. The effectiveness of a material to spread the heat generated and prevent excessive rise in temperature is directly related to its thermal conductivity. The thermal conductivities of the materials used in semiconductor device fabrication are fairly low.[9] For the thin film silicon based transistors, the thicknesses are of the same order as the phonon mean free path and since phonons are primarily responsible for the transport of heat, it leads to further degradation of the thermal conductivity.

1.1.2. Effect of scaling transistor size on electrical characteristics

As discussed in the previous section, the basic operation of a MOSFET is to act like a switch. A perfect switch would have zero current flowing in the channel when the switch is off, and zero resistance to charge carriers when the switch is turned on. Additionally, it is desirable that the MOSFET should be capable of switching instantly from 'off' to 'on', and vice versa with minimum subthreshold swing. However, MOSFETs are imperfect switches in the sense that the current in off-state is not zero, the current in the on-state is limited and switching between the two states requires some time.[1,16] Furthermore,

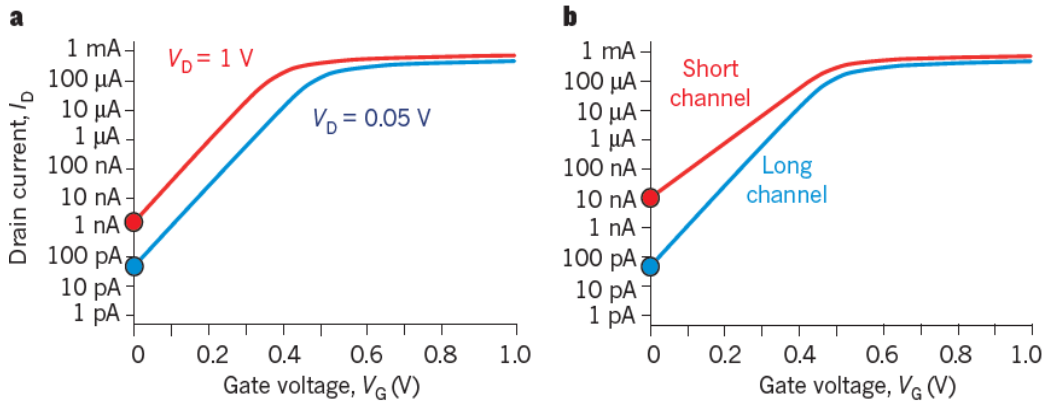

Figure 1.6. Illustration of short-channel effects**: (a)** DIBL effect shifts the electrical characteristics of the transistor to the left when the drain voltage is increased. (**b**) The subthreshold slope increases, which slows down the variation of current with gate voltage. Both of these effects increase the off currents, which are indicated by the blue and red circles.[1]

switching does not occur at a precise gate voltage but rather takes place gradually over a range of gate voltage values. When the transistor size is scaled down, these switching characteristics deteriorate further.[16] Due to these issues, the rules of conventional scaling as predicted by Moore's law are no longer applicable and this has led to a plateau with regards to improvement in microprocessor clock frequency. This saturation if caused by short-channel effects which arise when the effect channel length is of the order of the lattice constant of a silicon crystal. Briefly, these short-channel effects arise when the gate loses control of the charge carriers in channel region. This results in: (i) drain-induced barrier lowering (DIBL),[17] which causes the threshold voltage to decrease when the drain voltage increases (Fig. 1.6(a)); (ii) degradation of the subthreshold slope (Fig. 1.6(b)), and (iii) velocity saturation of charge carriers in the channel.[16,17] As illustrated in Fig. 1.7, these issues eventually lead to increase of leakage current of the transistors and this is a serious roadblock to further scaling of MOSFETs.[1,16]

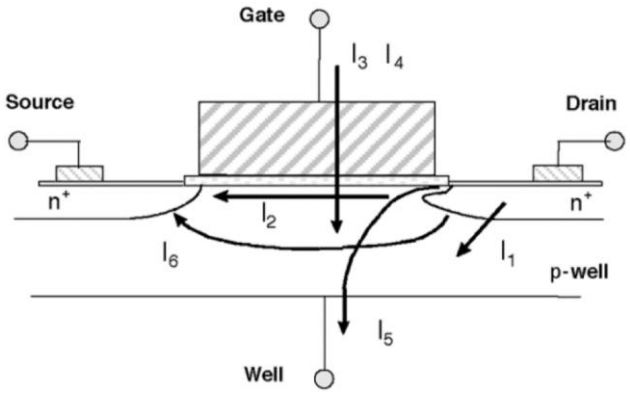

Figure 1.7. Summary of leakage current mechanisms in deep-submicrometer transistors. I_1 is the reverse-bias pn junction leakage; I_2 is the subthreshold leakage; I_3 is the oxide tunneling current; I_4 is the gate current due to hot-carrier injection; I_5 is the gate induced drain leakage; and I_6 is the channel punch-through current.[15]

In order to overcome the thermal and electrical issues with scaling, different measures with regards to device architecture and the materials used have been explored: (i) modification of the transistor architecture, such as ultra-thin body silicon on insulator MOSFETs and multiple-gate MOSFETs with small body cross section (Fig. 1.5),[17-19] and (ii) incorporating novel two-dimensional thin films as channel materials in the transistor design (Fig. 1.8).[20-23] The scaling theory predicts that FETs with a thin gate-controlled region will be more robust against short-channel effects. Hence, significant research is directed towards exploring newer materials and device concepts ensure improvement in device performance. This opens up

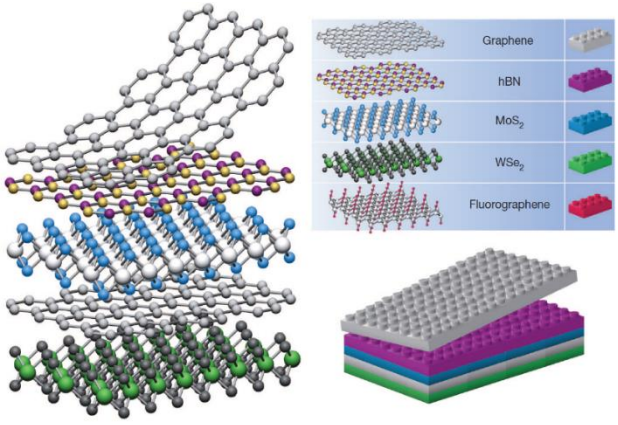

Figure 1.8. Novel two-dimensional van der Waals materials and heterostructures for future transistors.[22]

possibilities for FETs with two-dimensional van der Waals materials such as graphene and transition metal dichalcogenides (TMDs), which are one atomic layer thick.[23]

Before discussing the scope of novel materials in fabrication of FETs, it is necessary to realize that today's chip industry is focused on Si MOSFET to such an extent that it will be extremely difficult for a new material or device concept to compete with the Si MOSFET world unless the new concept offers a really significant edge. Some of the desired properties for an ideal semiconductor would include the following features: (i) high thermal conductivity in order to dissipate the power and prevent excessive rise in local temperature, (ii) sizable bandgap for achieving a high I_{ON}/I_{OFF} ratio, combined with high carrier mobility and low subthreshold swing ; (iii) commercially producible on a large scale, process friendly, and compatible with Si MOSFET technology; and (iv) good long term stability and low defect density not affecting carrier transport in the semiconductor close to the interface.

1.2. Introduction: Graphene based FETs

Among the large library of novel materials that have been studied in the past decade, the ones that have particularly attracted the most attention include carbon-based nanomaterials including graphene and carbon nanotubes. The rise of the 2D materials began in 2004 when graphene was first experimentally isolated by mechanical exfoliation of highly ordered pyrolytic graphite (HOPG).[24,25] Graphene is a one atom thick planar sheet of sp^2 hybridized carbon atoms tightly packed into a two-dimensional (2D) hexagonal honeycomb network. As shown in Fig. 1.9, graphene is the basic building block for all other carbon allotropes including graphite, carbon nanotubes and fullerenes.[25] The

intriguing properties of graphene that have made it a potential material to replace silicon include ambipolar electric field effect with mobilities of charge carriers exceeding 15,000-200,000 $cm^2\ V^{-1}\ s^{-1}$ even at room temperature,[26] high charge carrier concentration for an atomically thin film (~10^{12} cm^{-2}),[26] low contact resistance due to tunable fermi level,[27] excellent thermal conductivity (~5000 $W\ m^{-1}K^{-1}$),[28] optical transparency (~97.7%)[29] and flexibility.[30]

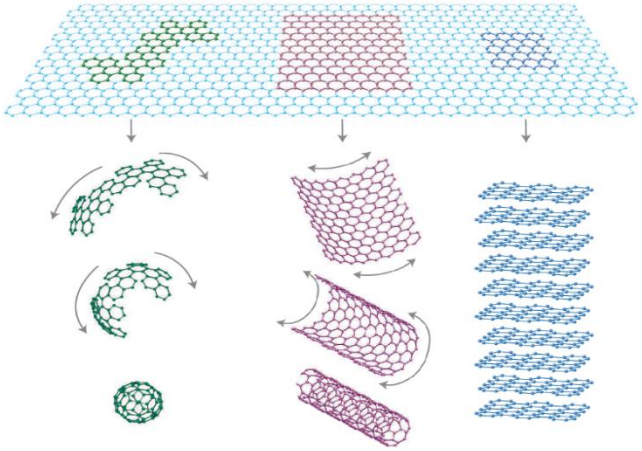

Figure 1.9. Graphene is a 2D building material for carbon materials of all other dimensionalities. It can be wrapped up into 0D buckyballs, rolled into 1D nanotubes or stacked into 3D graphite.[24]

The first graphene-based FET was reported in 2007,[31] and since then a large number of groups have successfully fabricated graphene transistors with cutoff frequencies in the 100–300 GHz range.[32,33] The first study by Novoselov and Geim reported a high room-temperature mobility of 10,000–15,000 $cm^2\ V^{-1}\ s^{-1}$,[23] and since then the measured record mobilities in graphene have exceeded 100,000 $cm^2\ V^{-1}\ s^{-1}$ at 4 K.[34] However, the primary focus of most of the earlier experimental studies was the high carrier mobility of graphene (Fig. 1.10). High carrier mobility is an important but not the only prerequisite for fast

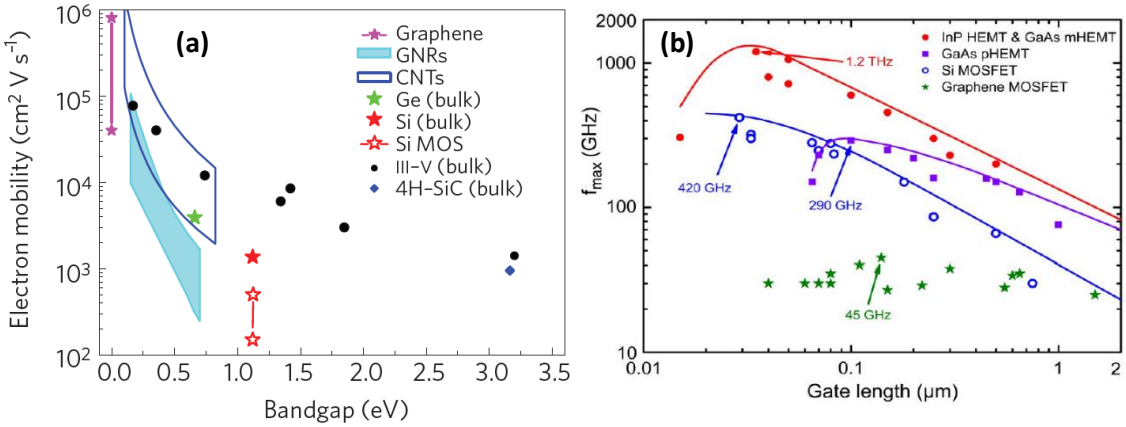

Figure 1.10. (a) Electron mobility versus bandgap in low electric fields for different materials.[35] **(b)** Maximum frequency of oscillation of graphene MOSFETs versus gate length. Also shown is the f_{max} performance of three classes of competing RF FETs: InP HEMTs and GaAs mHEMTs, GaAs pHEMTs, and Si MOSFETs.[20]

transistors, and this led to misleading assessments of the potential of graphene as the perfect material for ultrafast high-performance transistors.[20] Apart from high carrier mobility, another prerequisite for MOSFETs is presence of a sizable bandgap, which provides a high on-off ratio I_{ON}/I_{OFF}. I_{ON} is the on-current flowing when both V_{GS} and the drain–source voltage V_{DS} are equal to V_{DD} and I_{OFF} is current in the off-state (V_{GS} = 0 and V_{DS} = V_{DD}). The conventional semiconductors such as Si and Ge possess a sizable bandgap and exhibit on-off ratios in the range of $10^4 - 10^7$. In spite of all the intriguing properties of graphene, a roadblock that limits the operation of graphene based FETs is that natural graphene is a zero-gap material. Graphene transistors, due to the absence of a bandgap, cannot be switched off and are, therefore, not suited for complex logic circuits. This issue of absence of a bandgap has received increasing attention in recent years and efforts have been made to engineer a bandgap in graphene by different techniques.[36] Some of these techniques include confinement of charge carriers in one dimensional structures like graphene

nanoribbons[37,38] and graphene nanomesh,[39] biasing bilayer graphene,[40] applying strain[41] and applying chemical modifications to graphene.[42]

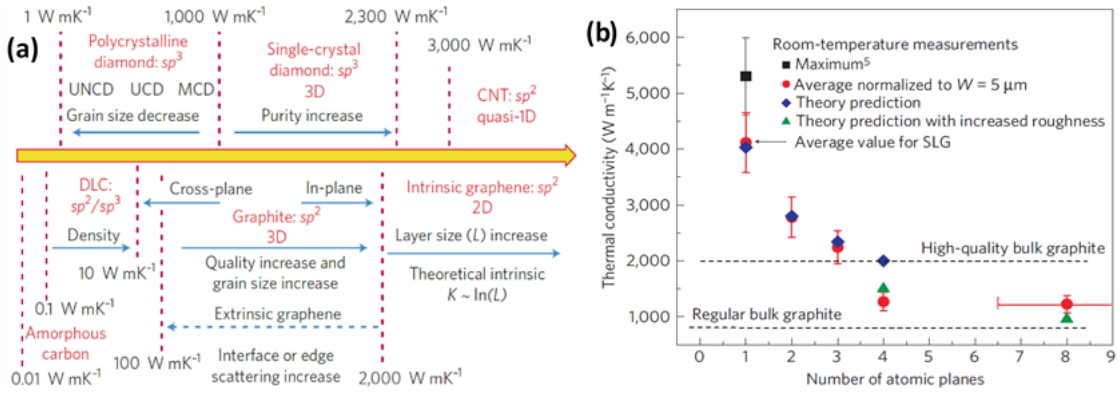

Figure 1.11. (a) Thermal conductivity of different carbon allotropes based on average values reported in literature;[43] (**b**) Thermal conductivity of graphene as a function of number of layers.[45]

Apart from the studies investigating carrier mobility and bandgap engineering in graphene-based FETs, the thermal conduction in graphene has also been an area of intense research from a practical need and also a fundamental science point of view.[28,43] As discussed in the section 1.1.1, heat removal has become a critical issue for continuing progress in the electronic industry owing to increased levels of dissipated power. Similar thermal issues have also been encountered in optoelectronic and photonic devices. Bulk graphite has a high basal plane thermal conductivity of graphite in the range of ~1500–2000 W m^{-1} K^{-1} at room temperature.[43] However, the thermal properties of all materials, including graphene, change when they are structured on a nanometer scale.[44] Experimental studies have examined the evolution of thermal properties of graphene as a function of number of layers (*n*), crystallinity, grain size and quality of graphene films.[45] As shown in Fig. 1.11, it was found that the thermal conductivity *K* of few-layer graphene decreases

with increasing *n*, approaching the bulk graphite limit.[43,45] This evolution of *K* was explained by considering the phonon Umklapp scattering,[46] i.e. when *n* in few-layer graphene increases, the phonon dispersion changes and more phase-space states become available for phonon scattering leading to a decrease in *K*. For suspended single layer graphene the thermal conductivity was found to be >5000 W m^{-1} K^{-1}, which is roughly two orders of magnitude higher compared to thin film Si. The planar geometry of graphene results in better coupling to the substrate and this allows for easier incorporation of graphene into the chip design. Additionally, the ease of patterning large area graphene into desired 1D and 2D nanostructures offers great potential for integration of graphene as device channel or interconnects.

However, it should be noted that most of these experimental studies investigating the carrier mobility, I_{ON}/I_{OFF} ratios and thermal conductivity of graphene are conducted using highly pristine graphene samples that are mechanically exfoliated from HOPG. Though the quality of the graphene isolated using exfoliation is superior, it does not offer control over the size, number of layers and is not reproducible. A more scalable and practical way of synthesizing graphene is via chemical vapor deposition (CVD).[47,48] Studies have shown growth of high quality large area films graphene with desired control over grain size and number of layers using transition metals as growth substrates. The resultant graphene films consist of individual single crystalline grains that merge together to form a polycrystalline film that inevitably contains grain boundaries. Furthermore, the various processing steps such as (a) transfer of graphene from growth substrate to a desired substrate, (b) material characterization steps involving electron microscopy, and (c) device

fabrication steps using photolithography, electron-beam lithography and plasma etching, can introduce defects in graphene films. These grain boundaries and defects act as scattering points and lower the electron mobility and thermal conductivity of graphene.

Thus, based on the results of preliminary studies carried on pristine, defect-free samples, graphene has proven its worth as a viable candidate to replace silicon and mitigate the scaling issues. However, there is still a lot of scope for further research to investigate how the extrinsic factors including grain boundaries and point defects affect the properties of graphene. Based on the current research studies, it is safe to assume that high-performance integrated logic circuits using graphene as a planar channel material are unlikely to make their way within the next decade. Consequently, a new direction being pursued in graphene research is towards complimenting the conventional semiconductors and using graphene in applications where other materials fail or perform poorly.[25,49] Intensive research is being conducted to explore applications of graphene as transparent electrodes,[50] touch screens, flexible and printable electronics,[30] photovoltaics and solar cells,[51] and chemical sensors.[52]

1.3. Objectives of this work

As per the discussion in above section with respect to current limitations in scalable synthesis of graphene and the effects of extrinsic factors on thermal and electrical transport properties, the objectives of this thesis are:

a) **Objective 1:** Develop a synthesis route based on chemical vapor deposition (CVD) for synthesis of high-quality single-layer graphene films with large grain size and to investigate effect of growth parameters such as annealing time, partial pressure of precursor

gases, C/H ratio in feedstock, gas flow rates and growth time on the grain size, crystallinity and number of layers in resultant graphene films. Discuss methods of transferring this graphene from metal substrate to different substrates such as TEM grids and Si/SiO2. Extensive characterization of morphological and crystalline structure using material characterization tools including Raman spectroscopy and electron microscopy.

b) Objective 2: Experimentally investigate the thermal conductivity and phonon dispersion in graphene films synthesized via CVD using opto-thermal Raman measurements and molecular dynamics (MD) simulations. Study the effect of point defects introduced in single-layer graphene via electron-beam irradiation on thermal properties.

c) Objective 3: Fabricate field-effect transistors (FETs) using large area single-layer graphene as the channel material and investigate the transport characteristics such as channel resistance, carrier mobility and I_{ON}/I_{OFF} ratio. Fabrication of graphene nanoribbons (GNRs) arrays using electron-beam lithography and superlattice nanowire pattern (SNAP) transfer process to engineer a bandgap in graphene by quantum confinement of charge carriers into one-dimensional nanostructures. Characterize the edge defect sites introduced using GNR fabrication process using Raman spectroscopy and x-ray photoelectron spectroscopy. Investigate thermal treatments for repairing these edge defects and restoring the mobility of GNR FET devices.

d) Objective 4: Explore the applications of carbon-based nanomaterials for fabrication of electrical nanobiosensors. Develop FET/chemiresistive-type sensors with carbon nanotubes as the transducer material and functionalized with a biological receptor

molecule for highly sensitive, selective, rapid and label-free detection of chemicals and biological species.

1.4. Organization of this thesis

Chapter 2 discusses CVD-synthesis and characterization of single-layer graphene (SLG) and twisted bilayer graphene (tBLG). Chapter 3 describes thermal transport in CVD graphene and effect of extrinsic factors on thermal conductivity. Chapter 4 describes the fabrication of graphene FET devices, bandgap engineering of graphene by synthesizing graphene nanoribbons (GNRs), characterization of edge defects in GNRs and application of GNR FETs as a gas sensor. Chapter 5 discusses the applications of carbon nanomaterials as electrical sensors for detection of chemicals and biomolecules. Finally, chapter 6 presents the concluding remarks of this dissertation along with suggestions for future work.

1.5. References

1. Ferain, Isabelle, Cynthia A. Colinge, and Jean-Pierre Colinge. "Multigate transistors as the future of classical metal-oxide-semiconductor field-effect transistors." Nature 479, no. 7373 (2011): 310-316.
2. Theis, Thomas N., and Paul M. Solomon. "In quest of the “next switch”: prospects for greatly reduced power dissipation in a successor to the silicon field-effect transistor." Proceedings of the IEEE 98, no. 12 (2010): 2005-2014.
3. ITRS, International Technology Working Groups International Technology Roadmap for Semiconductors〈http://www.itrs.net/Links/2010ITRS/Home2010.htm〉 (ITRS, 2010)

4. Iwai, H. I. R. O. S. H. I. "Roadmap for 22nm and beyond." Microelectronic Engineering 86, no. 7 (2009): 1520-1528.
5. Colinge, Jean-Pierre. "Multiple-gate soi mosfets." Solid-State Electronics 48, no. 6 (2004): 897-905.
6. Moore, Gordon E. "Cramming more components onto integrated circuits, Reprinted from Electronics, volume 38, number 8, April 19, 1965, pp. 114 ff." IEEE Solid-State Circuits Newsletter 3, no. 20 (2006): 33-35.
7. Schelling, Patrick K., Li Shi, and Kenneth E. Goodson. "Managing heat for electronics." Materials Today 8, no. 6 (2005): 30-35.
8. Moore, Arden L., and Li Shi. "Emerging challenges and materials for thermal management of electronics." Materials Today 17, no. 4 (2014): 163-174.
9. Pop, Eric, Sanjiv Sinha, and Kenneth E. Goodson. "Heat generation and transport in nanometer-scale transistors." Proceedings of the IEEE 94, no. 8 (2006): 1587-1601.
10. Krishnan, Shankar, Suresh V. Garimella, Greg M. Chrysler, and Ravi V. Mahajan. "Towards a thermal Moore's law." In ASME 2005 Pacific Rim Technical Conference and Exhibition on Integration and Packaging of MEMS, NEMS, and Electronic Systems collocated with the ASME 2005 Heat Transfer Summer Conference, pp. 591-603. American Society of Mechanical Engineers, 2005.
11. Mahajan, Ravi, Chia-pin Chiu, and Greg Chrysler. "Cooling a microprocessor chip." Proceedings of the IEEE 94, no. 8 (2006): 1476-1486.
12. Hamann, Hendrik F., Alan Weger, James A. Lacey, Zhigang Hu, Pradip Bose, Erwin Cohen, and Jamil Wakil. "Hotspot-limited microprocessors: Direct temperature and

power distribution measurements." IEEE Journal of Solid-State Circuits 42, no. 1 (2007): 56-65.

13. Sri-Jayantha, Sri M., Gerald McVicker, Kerry Bernstein, and John U. Knickerbocker. "Thermomechanical modeling of 3D electronic packages." IBM Journal of Research and Development 52, no. 6 (2008): 623-634.
14. Park, J-T., C. A. Colinge, and J-P. Colinge. "Comparison of gate structures for short-channel SOI MOSFETs." In SOI Conference, 2001 IEEE International, pp. 115-116. IEEE, 2001.
15. Roy, Kaushik, Saibal Mukhopadhyay, and Hamid Mahmoodi-Meimand. "Leakage current mechanisms and leakage reduction techniques in deep-submicrometer CMOS circuits." *Proceedings of the IEEE* 91, no. 2 (2003): 305-327.
16. Skotnicki, Thomas, and Frederic Boeuf. "How can high mobility channel materials boost or degrade performance in advanced CMOS." In VLSI Symp. Tech. Dig, pp. 153-154. 2010.
17. Hisamoto, Digh, Toru Kaga, Yoshifumi Kawamoto, and Eiji Takeda. "A fully depleted lean-channel transistor (DELTA)-a novel vertical ultra thin SOI MOSFET." In Electron Devices Meeting, 1989. IEDM'89. Technical Digest., International, pp. 833-836. IEEE, 1989.
18. Huang, Xuejue, Wen-Chin Lee, Charles Kuo, Digh Hisamoto, Leland Chang, Jakub Kedzierski, Erik Anderson et al. "Sub 50-nm finfet: Pmos." In Electron Devices Meeting, 1999. IEDM'99. Technical Digest. International, pp. 67-70. IEEE, 1999.

19. Doyle, B. S., S. Datta, M. Doczy, S. Hareland, B. Jin, J. Kavalieros, T. Linton, A. Murthy, R. Rios, and R. Chau. "High performance fully-depleted tri-gate CMOS transistors." IEEE Electron Device Letters 24, no. 4 (2003): 263-265.
20. Schwierz, Frank. "Graphene transistors: status, prospects, and problems." *Proceedings of the IEEE* 101, no. 7 (2013): 1567-1584.
21. Radisavljevic, Branimir, Aleksandra Radenovic, Jacopo Brivio, I. V. Giacometti, and A. Kis. "Single-layer MoS_2 transistors." *Nature nanotechnology* 6, no. 3 (2011): 147-150.
22. Geim, Andre K., and Irina V. Grigorieva. "Van der Waals heterostructures." Nature 499, no. 7459 (2013): 419-425.
23. Novoselov, Kostya S., Andre K. Geim, Sergei V. Morozov, D. Jiang, Y_ Zhang, Sergey V. Dubonos, Irina V. Grigorieva, and Alexandr A. Firsov. "Electric field effect in atomically thin carbon films." *science* 306, no. 5696 (2004): 666-669.
24. Geim, Andre K., and Konstantin S. Novoselov. "The rise of graphene." Nature materials 6, no. 3 (2007): 183-191.
25. Novoselov, Konstantin S., V. I. Fal, L. Colombo, P. R. Gellert, M. G. Schwab, and K. Kim. "A roadmap for graphene." Nature 490, no. 7419 (2012): 192-200.
26. Novoselov, K. S. A., Andre K. Geim, SVb Morozov, Da Jiang, MIc Katsnelson, IVa Grigorieva, SVb Dubonos, and AAb Firsov. "Two-dimensional gas of massless Dirac fermions in graphene." nature 438, no. 7065 (2005): 197-200.
27. Venugopal, A., L. Colombo, and E. M. Vogel. "Contact resistance in few and multilayer graphene devices." Applied Physics Letters 96, no. 1 (2010): 013512.

28. Balandin, Alexander A., Suchismita Ghosh, Wenzhong Bao, Irene Calizo, Desalegne Teweldebrhan, Feng Miao, and Chun Ning Lau. "Superior thermal conductivity of single-layer graphene." *Nano letters* 8, no. 3 (2008): 902-907.
29. Mak, Kin Fai, Matthew Y. Sfeir, Yang Wu, Chun Hung Lui, James A. Misewich, and Tony F. Heinz. "Measurement of the optical conductivity of graphene." *Physical review letters* 101, no. 19 (2008): 196405.
30. Bae, Sukang, Hyeongkeun Kim, Youngbin Lee, Xiangfan Xu, Jae-Sung Park, Yi Zheng, Jayakumar Balakrishnan et al. "Roll-to-roll production of 30-inch graphene films for transparent electrodes." Nature nanotechnology 5, no. 8 (2010): 574-578.
31. M. C. Lemme, T. J. Echtermeyer, M. Baus, and H. Kurz, ‘‘A graphene field-effect device,’’ IEEE Electron Device Lett., vol. 28, no. 4, pp. 282–284, Apr. 2007.
32. Y.-M. Lin, C. Dimitrakopoulos, K. A. Jenkins, D. B. Farmer, H.-Y. Chiu, A. Grill, and P. Avouris, ‘‘100-GHz transistors from wafer-scale epitaxial grapheme,’’ Science, vol. 327, p. 662, 2010.
33. L. Liao, Y.-C. Lin, M. Bao, R. Cheng, J. Bai, Y. Liu, Y. Qu, K. L. Wang, Y. Huang, and X. Duan, ‘‘High-speed graphene transistors with a self-aligned nanowire gate,’’ Nature, vol. 467, pp. 305–308, 2010.
34. A. S. Mayorov, R. V. Gorbachev, S. V. Morozov, L. Britnell, R. Jalil, L. A. Ponomarenko, P. Blake, K. S. Novoselov, K. Watanabe, T. Taniguchi, and A. K. Geim, ‘‘Micrometer-scale ballistic transport in encapsulated graphene at room temperature,’’ Nano Lett., vol. 11, pp. 2396–2399, 2011.

35. Schwierz, Frank. "Graphene transistors." Nature nanotechnology 5, no. 7 (2010): 487-496.
36. Marmolejo-Tejada, Juan M., and Jaime Velasco-Medina. "Review on graphene nanoribbon devices for logic applications." Microelectronics Journal 48 (2016): 18-38.
37. Han, Melinda Y., Barbaros Özyilmaz, Yuanbo Zhang, and Philip Kim. "Energy band-gap engineering of graphene nanoribbons." Physical review letters 98, no. 20 (2007): 206805.
38. Li, Xiaolin, Xinran Wang, Li Zhang, Sangwon Lee, and Hongjie Dai. "Chemically derived, ultrasmooth graphene nanoribbon semiconductors." Science 319, no. 5867 (2008): 1229-1232.
39. Paul, Rajat Kanti, Sushmee Badhulika, Nuvia M. Saucedo, and Ashok Mulchandani. "Graphene nanomesh as highly sensitive chemiresistor gas sensor." Analytical chemistry 84, no. 19 (2012): 8171-8178.
40. Zhang, Yuanbo, Tsung-Ta Tang, Caglar Girit, Zhao Hao, Michael C. Martin, Alex Zettl, Michael F. Crommie, Y. Ron Shen, and Feng Wang. "Direct observation of a widely tunable bandgap in bilayer graphene." Nature 459, no. 7248 (2009): 820-823.
41. Ni, Zhen Hua, Ting Yu, Yun Hao Lu, Ying Ying Wang, Yuan Ping Feng, and Ze Xiang Shen. "Uniaxial strain on graphene: Raman spectroscopy study and band-gap opening." ACS nano 2, no. 11 (2008): 2301-2305.
42. Liu, Hongtao, Yunqi Liu, and Daoben Zhu. "Chemical doping of graphene." Journal of materials chemistry 21, no. 10 (2011): 3335-3345.

43. Balandin, Alexander A. "Thermal properties of graphene and nanostructured carbon materials." *Nature materials* 10, no. 8 (2011): 569-581.
44. Nika, Denis L., Artur S. Askerov, and Alexander A. Balandin. "Anomalous size dependence of the thermal conductivity of graphene ribbons." Nano letters 12, no. 6 (2012): 3238-3244.
45. Ghosh, Suchismita, Wenzhong Bao, Denis L. Nika, Samia Subrina, Evghenii P. Pokatilov, Chun Ning Lau, and Alexander A. Balandin. "Dimensional crossover of thermal transport in few-layer graphene." *Nature materials* 9, no. 7 (2010): 555-558.
46. Nika, D. L., E. P. Pokatilov, A. S. Askerov, and A. A. Balandin. "Phonon thermal conduction in graphene: Role of Umklapp and edge roughness scattering." *Physical Review B* 79, no. 15 (2009): 155413.
47. Choi, Wonbong, Indranil Lahiri, Raghunandan Seelaboyina, and Yong Soo Kang. "Synthesis of graphene and its applications: a review." *Critical Reviews in Solid State and Materials Sciences* 35, no. 1 (2010): 52-71.
48. Avouris, Phaedon, and Christos Dimitrakopoulos. "Graphene: synthesis and applications." *Materials today* 15, no. 3 (2012): 86-97.
49. Ferrari, Andrea C., Francesco Bonaccorso, Vladimir Fal'Ko, Konstantin S. Novoselov, Stephan Roche, Peter Bøggild, Stefano Borini et al. "Science and technology roadmap for graphene, related two-dimensional crystals, and hybrid systems." *Nanoscale* 7, no. 11 (2015): 4598-4810.
50. Kim, Keun Soo, Yue Zhao, Houk Jang, Sang Yoon Lee, Jong Min Kim, Kwang S. Kim, Jong-Hyun Ahn, Philip Kim, Jae-Young Choi, and Byung Hee Hong. "Large-

scale pattern growth of graphene films for stretchable transparent electrodes." *Nature* 457, no. 7230 (2009): 706-710.

51. Park, Hyesung, Jill A. Rowehl, Ki Kang Kim, Vladimir Bulovic, and Jing Kong. "Doped graphene electrodes for organic solar cells." *Nanotechnology* 21, no. 50 (2010): 505204.
52. Shao, Yuyan, Jun Wang, Hong Wu, Jun Liu, Ilhan A. Aksay, and Yuehe Lin. "Graphene based electrochemical sensors and biosensors: a review." *Electroanalysis* 22, no. 10 (2010): 1027-1036.

CHAPTER 2

Chemical vapor deposition (CVD) synthesis and Raman spectroscopy of single layer and twisted bilayer graphene

2.1. Introduction

Integration of graphene into the current MOSFET device fabrication requires development of scalable synthesis protocols and wafer scale deposition processes using existing fabrication techniques. In order to fully realize the potential of graphene for practical applications, there has been a lot of research dedicated to deposition of high quality and uniform graphene films over large areas with controllable thickness.[1,2] Unlike other nanomaterials, the advantage with graphene is that it can be deposited on large scale in a cost-effective manner using bottom-up[3] (atom by atom growth) or top-down (exfoliation from bulk) techniques.[4] The highest quality graphene, in terms of structural integrity and material properties, is obtained by mechanical exfoliation of highly oriented pyrolytic graphite (HOPG).[5] Thus, the efficacy of any synthesis technique is evaluated by comparing the material properties to mechanically exfoliated graphene. Among the several techniques that have been explored for large scale synthesis of graphene including liquid phase exfoliation,[6] reduction of graphene oxide (GO) growth on SiC[7] and chemical vapor deposition (CVD).[8,9] In particular, CVD is considered to be the most promising, scalable and economical approach. CVD has been extensively employed for deposition of thin films and is considered as the workhorse tool for semiconductor device fabrication, and thus it is readily accessible and compatible with the current MOSFET fabrication techniques.

CVD synthesis of graphene has been demonstrated on a variety of transition metals substrates including Ru,[10] Ir,[11], Pt[12] and Ni.[13] The growth mechanism on these substrates involves thermal decomposition of the hydrocarbon feedstock, typically methane, on the surface or surface segregation of carbon upon cooling from a metastable carbon–metal solid solution. However, the relatively high solubility of carbon in these metals often leads to non-homogenous graphene films as the segregation of carbon from metal-carbide solution occurs rapidly within the grains and heterogeneously at the grain boundaries.[9] Due to these limitations, use of copper as a growth substrate has gathered the most interest due to low solubility of carbon in copper. The growth of graphene on copper is a surface-limited process which results in self-limiting single-layer graphene films.[14,15] The nucleation density of graphene grains can be controlled by adjusting the annealing time and partial pressure of the carbon feedstock, i.e. methane, and the gas flow rates and growth time can be controlled to obtain individual single crystal grains or large-area polycrystalline films of graphene. Additionally, this process is economically feasible and scalable due to ease of availability and low cost of polycrystalline copper foils.

Unlike exfoliation or epitaxial growth that results in AB-stacked graphene, bilayer (or few layer) graphene grown by CVD has a relative mis-orientation between the individual layers. Such a bilayer graphene system where the two atomic planes are rotated relative to each other is often referred to as turbostatic, misoriented, or twisted bilayer graphene (tBLG). When one layer of graphene is rotated with respect to the other, they form a Moiré pattern, the periodicity of which represents a new structural length scale of

the system.[16,17] The resulting electrical, vibrational, thermal and optical properties depend on the relative twist angle between the layers.[18]

The electrical and phonon properties of AB-BLG have been extensively studied both experimentally[19,20] and theoretically.[21] The electronic structure of AB-stacked bilayer graphene consists of quadratic dispersion with two parallel parabolic conduction bands situated above another two parallel parabolic valence bands with zero bandgap.[19] For tBLG with twist angles beyond a few degrees, the low-energy states in each layer electronically decouple, and the low-energy dispersion becomes linear although with reduced velocity for angles below 10°.[22] In an experimental study it was found that tBLG had lower thermal conductivity as compared to AB-BLG and SLG.[23] This suggests that, unlike electrons, phonons which are the primary heat carriers, do not propagate in tBLG as in two independent SLG planes, and there is a finite degree of van der Waals interaction between the atomic planes of tBLG.[23] Raman spectroscopy has been the primary experimental tool for analyzing the vibrational properties of graphene-based systems such as AB-BLG and tBLG.[24,25]

In this work, we present a detailed analysis of synthesis of high quality single layer graphene (SLG) and twisted bilayer graphene (tBLG) using ambient pressure chemical vapor deposition (AP-CVD). The grain size and number of layers were controlled by varying growth parameters such as partial pressure of carbon precursor, annealing time and growth time. The quality of the graphene films was characterized using material characterization tools including scanning electron microscopy (SEM), transmission electron microscopy and Raman spectroscopy. We report a detailed analysis of phonon

dispersion and vibrational properties in tBLG using Raman spectroscopy as the experimental tool to study evolution of peak intensity, width and position for G and 2D bands as a function of relative twist angle between the graphene layers. Finally, we look into the details of the low frequency ZO′ (or ZA) modes, which correspond to inter-layer breathing modes,[26] and new modes that are observed in frequency range of 90 - 200 cm^{-1}. We compared the frequency of the experimentally observed low frequency modes with the theoretical frequencies calculated using large scale molecular dynamics (MD) simulations. This work provides an improved understanding of angle-dependent vibrational properties and inter-layer coupling in two-dimensional van der Waals (vdW) materials and this could be important for exploring new potential applications of vdW heterostructures.

2.2. Experimental details

2.2.1. Graphene synthesis

Single-layer graphene (SLG) and twisted-bilayer graphene (tBLG) samples were synthesized using ambient pressure chemical vapor deposition (AP-CVD) on a polycrystalline copper foil using methane as a carbon feedstock. Briefly, a polycrystalline Cu foil (*Alfa Aesar*, 99.8% purity, 0.025mm thickness) was cleaned in 10% acetic acid,

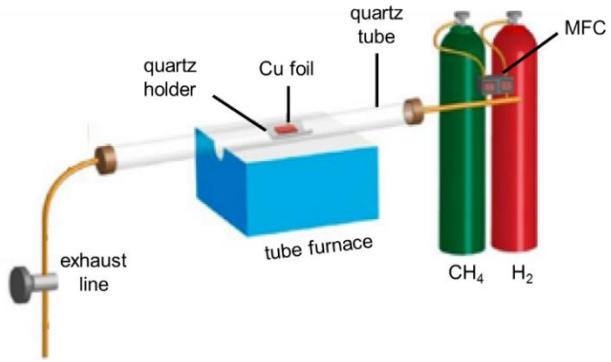

Figure 2.1. A schematic representation of the CVD setup used for synthesis of graphene.

acetone and isopropyl alcohol (IPA) for 10 minutes to remove any surface oxides. The cleaned Cu foil was loaded into the quartz tube (1″ diameter) and the furnace temperature was ramped to 1030˚C while flowing Ar and H_2. The schematic of the set-up in shown in Fig. 2.1. For the growth of graphene, three different conditions were used:

(A) **Condition A:** The Cu foil was annealed at 1030˚C for 30 minutes while flowing Ar (180 sccm) and H_2 (10 sccm). For the growth of graphene, CH_4 (5 sccm) was introduced along with Ar (180 sccm) and H_2 (5 sccm) for 7 min. The furnace was then turned off and cooled to room temperature while keeping the Ar and H_2 flow rates constant.

(B) **Condition B:** The Cu foil was annealed at 1030˚C for 2 hours under flowing Ar (300 sccm) and H_2 (15 sccm). For the growth of graphene, low concentration CH_4 (90 ppm in Ar, 375 sccm) and H_2 (15 sccm) were introduced into the chamber for 20 minutes. Following the growth, the furnace was turned off and cooled to room temperature in Ar and H_2 atmosphere.

(C) **Condition C:** For synthesis of tBLG, the annealing parameters and growth temperature were same as Condition B. In order to obtain single crystalline tBLG grains instead of a polycrystalline film, the methane flow rate and growth time were lowered. Low concentration CH_4 (90 ppm in Ar, 300 sccm) and H_2 (15 sccm) were introduced into the chamber for 12 minutes.

The morphology, grain size and the number of layers in the graphene synthesized using the three conditions were examined using scanning electron microscopy (SEM) of the copper foil with graphene.

2.2.2. Transfer of graphene from Cu foil to a substrate

The graphene grown on the Cu foil was transferred to a TEM grid and a Si/SiO_2 substrate using two different techniques. For the transfer of graphene on Si/SiO_2 substrate, a commonly used method based on a polymer support layer was employed. Briefly, the Cu foil with graphene was spin-c oated with a layer of poly(methyl methacrylate) (4% in anisole) at 2000 rpm and baked at 180˚C for 10 min. The copper foil was then etched in 0.2 M ammonium persulfate $(NH_4)_2S_2O_8$ solution and washed repeatedly with DI water. The resulting PMMA/graphene film floating on the surface of DI water was transferred to a Si/SiO_2 chip (pre-cleaned in ammonium hydroxide NH_4OH) and dried in air. The PMMA layer was dissolved in acetone and graphene chip was annealed at 250˚C in air to remove the polymer residues and improve the contact between the graphene film and substrate.

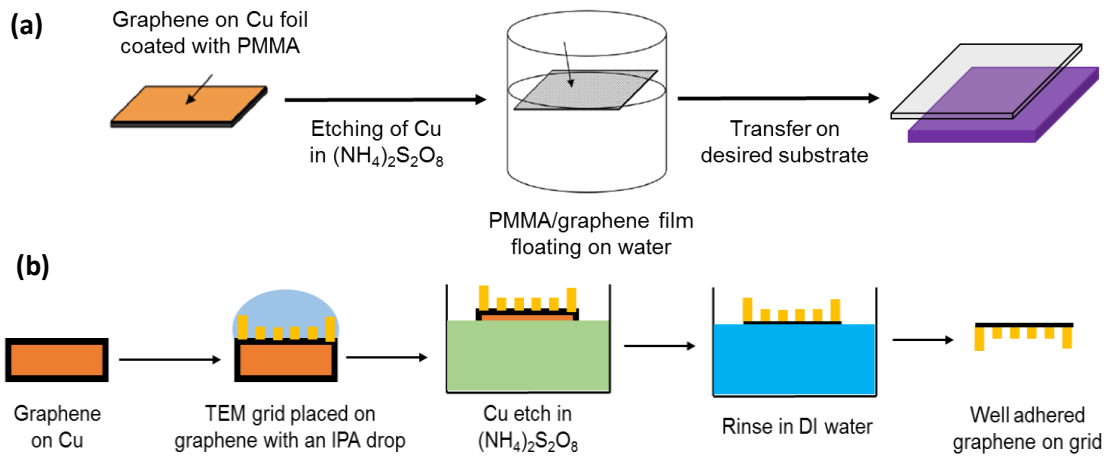

Figure 2.2. Schematic representation of the steps involved in transfer of graphene from copper foil to **(a)** Si/SiO_2 substrate using PMMA-based transfer, and **(b)** TEM grid using direct polymer-free transfer method.

For Raman spectroscopic measurements and TEM characterization, the graphene grains were transferred on to a gold TEM grid using a polymer-free, direct transfer method to avoid any contamination from the polymer support layer. Briefly, a TEM grid (G2000, 7.5 µm square holes, *TedPella*) was placed directly on the Cu foil with graphene stack along with a drop of isopropyl alcohol (IPA). On heating, as the IPA evaporates the surface tension draws the graphene and metallic grid together into intimate contact. The Cu foil is then etched in 0.2 M $(NH_4)_2S_2O_8$ solution, washed in DI water and the resulting graphene on TEM grid is dried in vacuum and used for subsequent Raman measurements and TEM analysis. A schematic representation of the above steps in shown in Fig. 2.2.

2.2.3. Raman spectroscopy

For characterizing the quality of the graphene such as presence of defects, crystalline nature, number of layers and twist angle-dependent vibrational properties, Raman spectroscopy was employed. The Raman spectra were recorded using a Horiba LabRam monochromator equipped with a 532 nm (2.33 eV) laser with 1800 lines/mm grating and a 100X objective (NA = 0.94) at room temperature. The laser spot size was about 1 µm, and the laser power was kept below 1 mW to avoid local heating of suspended graphene sample. The Raman spectra were collected from the regions on TEM grid where the entire 7.5 µm square hole was covered with graphene and regions with holes or partial folding of graphene film were avoided.

2.2.4. Transmission electron microscopy (TEM) characterization

The determination of crystalline nature and atomic scale characterization of graphene was performed using high-resolution TEM imaging. Further, the relative twist

angle between the graphene layers in tBLG was characterized using selected area electron diffraction (SAED) patterns. Bright-field TEM imaging and selected area diffraction patterns were obtained using a FEI Tecnai 12 TEM operated at 80 kV accelerating voltage. For precise mapping of different tBLG grains on the TEM grid between the Raman spectroscopy experiments and TEM analysis, the squares on TEM grid were assigned coordinates. Since the use of high energy electron irradiation is known to introduce defects in the suspended graphene, the TEM analysis for determining the twist angle was done after the Raman scattering experiments.

2.3. Results and Discussion

2.3.1. Electron microscopy characterization

The scanning electron microscopy (SEM) images of the single layer and twisted bilayer graphene on Cu foil grown using the three conditions are shown in Fig. 2.3. The shorter annealing time (30 minutes) and high partial pressure of CH_4 (20 Torr) used in Condition A resulted in a high nucleation density of graphene on Cu foil. Due to self-limiting growth mechanism, the resultant polycrystalline graphene film had a high percentage of grain boundaries with an average grain size of 1-2 μm (Fig. 2.3 (a,b)). These grain boundaries are highly undesirable since they act as scattering sites and thus affect the thermal and electrical transport in graphene. In comparison, the longer annealing time (2 hours) and low concentration of CH_4 (90 ppm) used in Condition B resulted in much lower nucleation density of graphene growth seeds. This low nucleation density, in turn, allows for growth of high quality single-crystalline grains of graphene with grain sizes in the range of 150-200 μm and minimizes grain boundaries by preventing overlapping of graphene

grains (Fig. 2.3 (c,d)). For synthesis of tBLG grains using Condition C, the annealing duration and methane concentration was kept same as Condition B but flow rate was lowered (300 sccm) to increase the residence time of precursor gas in the chamber and this led to nucleation of a second graphene layer. As shown in Fig. 2.3(e,f), for a growth time

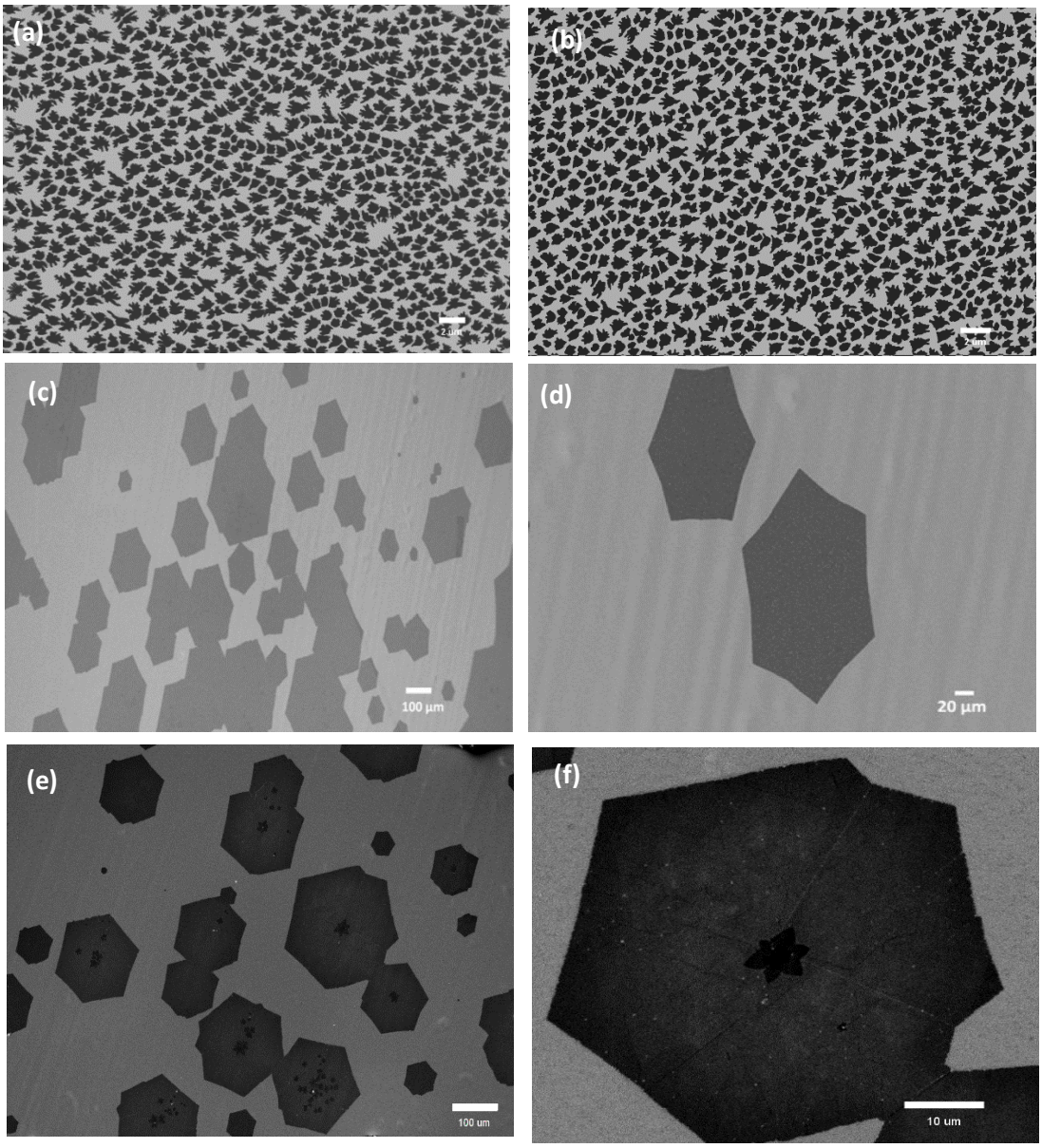

Figure 2.3. Scanning electron microscopy images of graphene grown on Cu foil using Condition A – **(a, b)**, Condition B – **(c, d)**, and Condition C – **(e, f)**.

of 12 minutes the average grain size for first graphene layer was 25-30 μm and the second layer of graphene that nucleated near the center of first grain had an average size of ~5 μm. This is indicative that the center of first (primary) layer acts as a preferential nucleation site for the growth of secondary layer.

Fig. 2.4 shows the high resolution-transmission electron microscopy (HR-TEM) and selected area electron diffraction (SAED) patterns obtained for the SLG (Condition B) and tBLG grains (Condition C). The honeycomb lattice arrangement shown in Fig. 2.4(a)

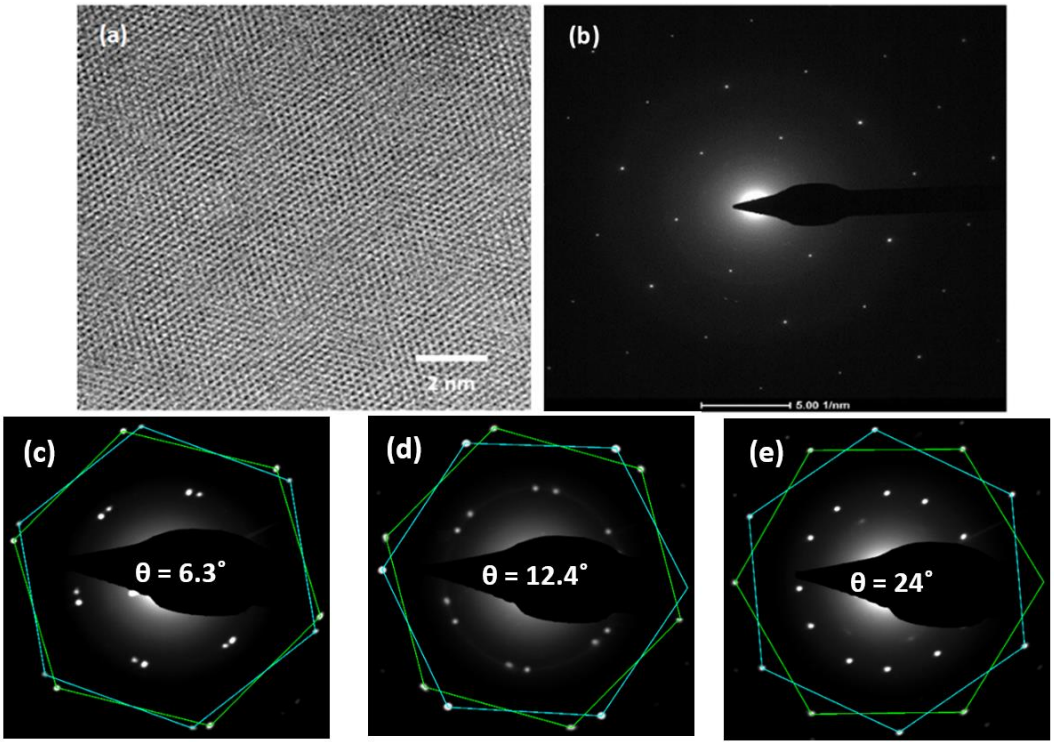

Figure 2.4. (a) High resolution transmission electron microscopy image of SLG, **(b)** Selected area electron diffraction (SAED) pattern for SLG, **(c-e)** SAED patterns showing relative twist angles of θ = 6.3˚, 12.4˚, and 24˚, respectively between the graphene layers in tBLG.

confirms the crystallinity and pristine nature of the SLG films synthesized using CVD (Condition B). Additionally, the number of graphene layers were verified by obtaining electron diffraction patterns. The diffraction pattern obtained from the SLG region showed

a hexagonal pattern (Fig. 2.4(b)), while that obtained from a tBLG region showed a diffraction pattern with two sets of hexagonal patterns rotated at a certain angle that is indicative of the relative twist angle θ between the stacked layers (Fig. 2.4(c-e)). This technique allows for determination of the twist angle with an accuracy of ±1˚.

2.3.2. Raman spectroscopic analysis of SLG and tBLG

Raman spectroscopy has been extensively used for characterization of number and orientation of graphene layers, doping, quantifying defects, and determining the types of edge functional groups.[27,28] Graphitic systems typically exhibit three signature peaks in the Raman spectra: G, D, and 2D. The G-peak typically centered around 1586 cm^{-1} originates from the doubly degenerate E_{2g} phonon mode at the Brillouin zone (BZ) center and corresponds to the C-C stretching mode. The D-peak centered around 1350 cm^{-1} originates from the LO phonon mode near K-points in the BZ and corresponds to breathing modes of sp^2 rings. For pristine defect-free graphene, the D-peak is hardly detectible since it is only activated by structural defects in a second order inter-valley double resonance process. The 2D-peak, which is the second order D peak centered around 2690 cm^{-1}, arises from two phonons with opposite momentum in the highest optical branch near the K-point. The Raman spectra for the SLG synthesized using

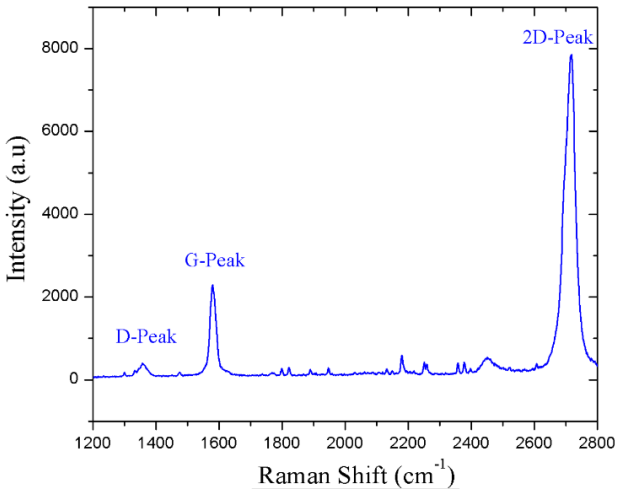

Figure 2.5. Raman spectra of SLG suspended on a TEM grid.

Condition B is shown in Fig. 2.5. The I_{2D}/I_G ratio was >3 and FWHM (full width at half maxima) for G and 2D-peaks were 8 cm^{-1} and 20 cm^{-1}, respectively. These observations are indicative of single-layer nature of graphene. Additionally, the D-peak which is indicative of defects, had negligible intensity and this further confirms the pristine nature of graphene.

The Raman spectra for tBLG is extremely sensitive to the relative twist angle between the graphene layers. Fig. 2.6 shows the Raman spectra of different tBLG grains (having rotation angles θ = 5.8°, 7.2°, 11.2°, 14.7°, 19°, 24.7°, 26º and 29.3°). The resonant

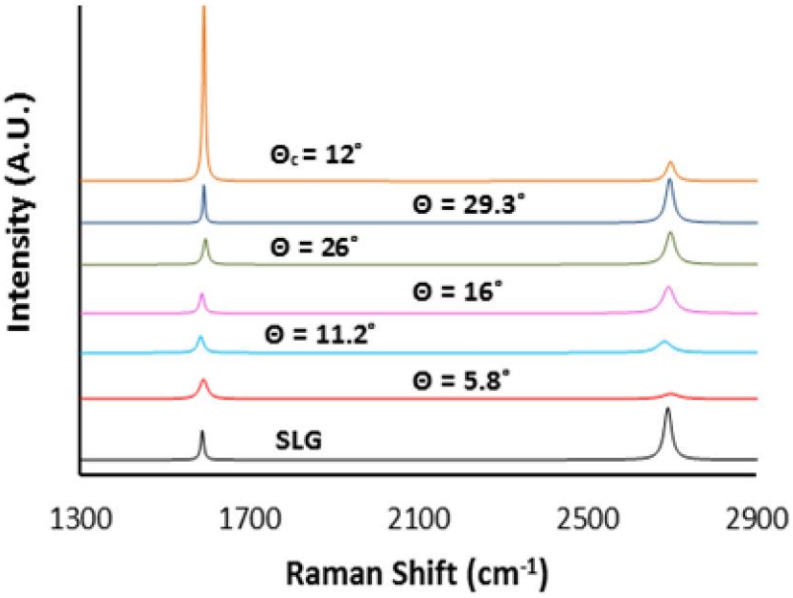

Figure. 2.6. Raman spectra of different tBLG samples labelled with the corresponding twist angle determined using TEM. The experimentally observed peaks were fitted with a Lorentzian function and shifted vertically for clarity.

enhancement of G-peak was also observed for tBLG with θ_c = 12°. This agrees with the estimate of $\theta_c = \Delta k/K = 3aE_{laser}/\hbar v_f 4\pi$ where a is the lattice parameter of graphene (2.46 Å), $\hbar$ is the reduced Planck's constant, and v_f is the Fermi velocity in monolayer graphene

(10^6 m/s), E_{laser} is the energy of the excitation source. Unlike AB-BLG, the I_{2D}/I_G ratio for tBLG varies significantly as a function of θ. For smaller twist angles (< ~10°), the Raman spectra looks similar to that of few-layer graphene with I_{2D}/I_G < 1. For larger twist angles (>20°), the Raman spectra looks similar to that of single-layer graphene with the I_{2D}/I_G ratio > 1, which signifies the layer decoupling mechanism. Fig. 2.7 shows the observed I_{2D}/I_G ratios as a function of θ.

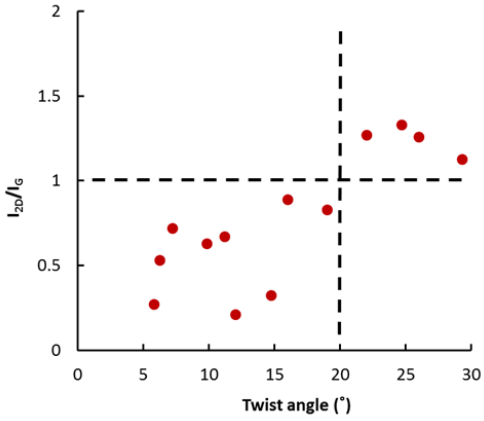

Figure. 2.7. Plot of 2D to G peak intensity as a function of twist angle θ.

In order to identify correlation between the Raman spectra and the corresponding twist angle, the angle-dependent Raman spectra for different tBLG systems were looked into detail by analyzing the FWHM and peak centers of the G and 2D-peaks. As shown in Fig. 2.8, for smaller twist angles, the G and 2D-peak widths were broader compared to those of SLG. There was an increase around the resonant twist angle, θ_c = 12°. As θ

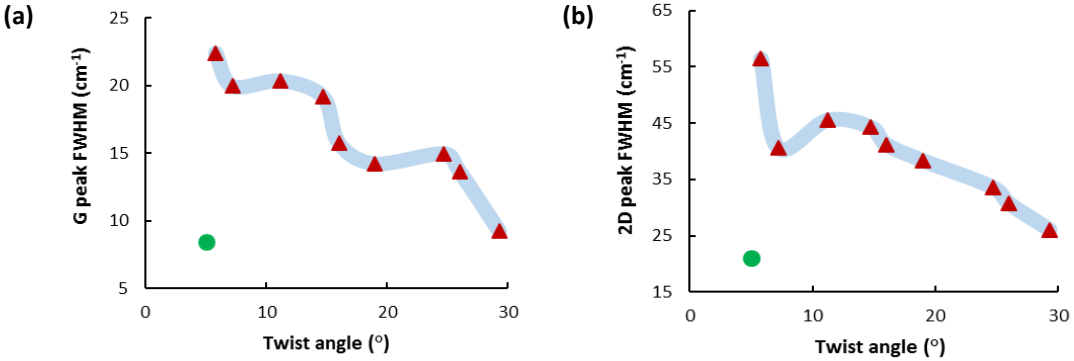

Figure. 2.8. FWHM of **(a)** G-peak and **(b)** 2D-peak for tBLG as a function of twist angle. The G and 2D peaks were fitted with a single Lorentzian peak. FWHM for SLG is indicated by the green dot for reference. The blue line is guide to the eye.

increased above θ_c, the FWHM of the 2D-peak monotonically decreased. The FWHM of the G-peak had a plateau between 19° and 24.7°, and then decreased with a minimum at 30° that was close to the FWHM of SLG. In case of peak positions, shown in Fig. 2.9, the center of G-peak for tBLG grains was upshifted by 5-15 cm^{-1} as compared to SLG. However, due to shift in peak positions arising from doping of graphene upon interaction with chemicals used in transfer process, no specific trend was observed as a function of θ. The trends observed for intensity ratios and peak widths as a function of twist angle are indicative of layer decoupling with increasing twist angle and are similar to those reported in literature.

In addition to the twist angle dependent evolution of G and 2D bands, we further analyzed low-energy phonon modes by performing molecular dynamics calculations of the phonon dispersion for commensurate rotation angles between 0° and 30°. Numerical details

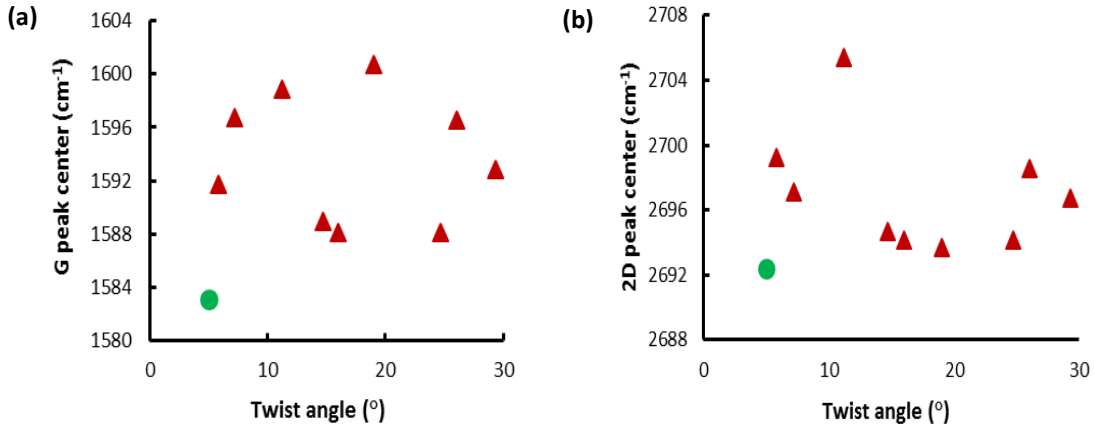

Figure. 2.9. Position of **(a)** G-peak and **(b)** 2D-peak center as a function of twist angle for tBLG. The G peak center position for SLG is shown by the green dot for comparison.

are provided in the Appendix A. In a graphitic system like tBLG, the ZO′ (or ZA) modes, at frequency of ~95cm^{-1}, correspond to inter-layer breathing modes and describe the

coupling between the layers.[26,29] We identified these low-frequency ZO' modes by analyzing both the direction and the magnitude of the out-of-plane displacements on each layer. Two exemplary low-frequency dispersions near Γ for twist angles 6.01° and 13.17° are shown in Fig. 2.10(a). The ZO′ mode at Γ, corresponding to the out-of-plane displacement of each layer, is indicated by the red solid circle, and the frequencies corresponding to the acoustic branches and the zone-folded acoustic branches are indicated by the blue solid circles. The low-frequency ZO′ modes for all of the simulated tBLG systems are tabulated in Table 2.1. A plot of the low-frequency experimental Raman spectrum for various measured twist angles is superimposed on the

Table 2.1 Evolution of the theoretically predicted frequency for the low-energy ZO′ mode as a function of twist angle ordered by supercell size.

Twist angle (θ)	No. of atoms in supercell	Theoretically predicted low frequency ZO' modes (cm^{-1})	Change in frequency Δf (cm^{-1})
AB	4	96.44	0.0
21.78°	28	94.56	-1.88
27.79°	54	95.66	-0.78
13.17°	76	93.76	-2.68
9.43°	148	97.97	1.53
7.34°	244	96.94	0.50
6°	364	90.13	-6.31

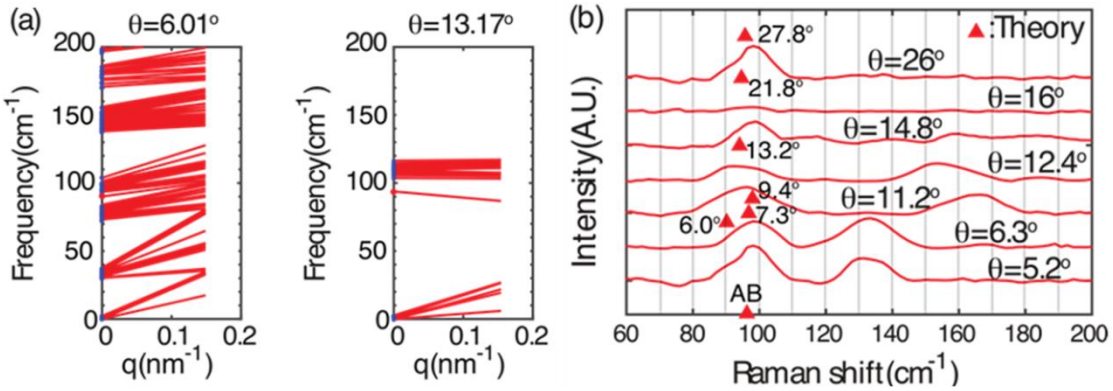

Figure. 2.10 (a) Calculated phonon dispersion near Γ with θ = 6.01°(left) and θ = 13.17°(right). The plots consist of only two q-points due to the large size of the supercells; **(b)** Calculated ZO' mode frequencies (red triangles) plotted on top of the low-energy Raman spectrum from various experimentally observed twist angles in tBLG systems.

theoretically calculated ZO′ frequencies in Fig. 2.10(b). It can be seen that the experimental peaks occur in the expected theoretical frequency range of the ZO′ mode, and that the shifts are not monotonic functions of either the angle or the supercell lattice constant.

2.4. Conclusions

In conclusion, we have demonstrated a controlled, reproducible way of synthesizing high quality single layer and twisted bilayer graphene with large grain size using ambient-pressure chemical vapor deposition. The quality of the graphene samples was characterized using Raman spectroscopy and electron microscopy. The twist angle-dependent vibrational properties in tBLG were analyzed by obtaining Raman spectra for the various tBLG grains with twist angles determined using selected area electron diffraction (SAED). The G and 2D-peaks were looked into detail to determine extent of coupling between the graphene layers as a function of twist angle. Large scale molecular dynamics simulations were employed to study the low-frequency phonon dispersion as a function of twist angle and compared to the measured Raman spectra. Shifts of a few cm^{-1} were observed, numerically and experimentally, in the ZO′ mode that were not monotonic functions of angle or supercell size. Raman peaks in range 120 cm^{-1} to 200 cm^{-1} were observed for the lower angle samples. Consistent with the previous observations, the peaks in this frequency range did show a monotonic dependence on rotation angles between 11˚ and 14˚. Using tBLG as a model system, we demonstrate that the vibrational properties and inter-layer coupling for van der Waals (vdW) heterostructures can be analyzed by this method.

2.5. References

1. Choi, Wonbong, Indranil Lahiri, Raghunandan Seelaboyina, and Yong Soo Kang. "Synthesis of graphene and its applications: a review." *Critical Reviews in Solid State and Materials Sciences* 35, no. 1 (2010): 52-71.
2. Avouris, Phaedon, and Christos Dimitrakopoulos. "Graphene: synthesis and applications." *Materials today* 15, no. 3 (2012): 86-97.
3. Cai, Jinming, Pascal Ruffieux, Rached Jaafar, Marco Bieri, Thomas Braun, Stephan Blankenburg, Matthias Muoth et al. "Atomically precise bottom-up fabrication of graphene nanoribbons." *Nature* 466, no. 7305 (2010): 470-473.
4. Bonaccorso, Francesco, Antonio Lombardo, Tawfique Hasan, Zhipei Sun, Luigi Colombo, and Andrea C. Ferrari. "Production and processing of graphene and 2d crystals." *Materials Today* 15, no. 12 (2012): 564-589.
5. Novoselov, Kostya S., Andre K. Geim, Sergei V. Morozov, D. Jiang, Y_ Zhang, Sergey V. Dubonos, Irina V. Grigorieva, and Alexandr A. Firsov. "Electric field effect in atomically thin carbon films." *science* 306, no. 5696 (2004): 666-669.
6. Hernandez, Yenny, Valeria Nicolosi, Mustafa Lotya, Fiona M. Blighe, Zhenyu Sun, Sukanta De, I. T. McGovern et al. "High-yield production of graphene by liquid-phase exfoliation of graphite." *Nature nanotechnology* 3, no. 9 (2008): 563-568.
7. Ohta, Taisuke, Aaron Bostwick, Thomas Seyller, Karsten Horn, and Eli Rotenberg. "Controlling the electronic structure of bilayer graphene." *Science*313, no. 5789 (2006): 951-954.

8. Zhang, Yi, Luyao Zhang, and Chongwu Zhou. "Review of chemical vapor deposition of graphene and related applications." *Accounts of chemical research* 46, no. 10 (2013): 2329-2339.
9. Mattevi, Cecilia, Hokwon Kim, and Manish Chhowalla. "A review of chemical vapour deposition of graphene on copper." *Journal of Materials Chemistry* 21, no. 10 (2011): 3324-3334.
10. Sutter, Peter W., Jan-Ingo Flege, and Eli A. Sutter. "Epitaxial graphene on ruthenium." *Nature materials* 7, no. 5 (2008): 406-411.
11. Coraux, Johann, Alpha T. N'Diaye, Carsten Busse, and Thomas Michely. "Structural coherency of graphene on Ir (111)." *Nano letters* 8, no. 2 (2008): 565-570.
12. Gao, Libo, Wencai Ren, Huilong Xu, Li Jin, Zhenxing Wang, Teng Ma, Lai-Peng Ma et al. "Repeated growth and bubbling transfer of graphene with millimetre-size single-crystal grains using platinum." *Nature communications*3 (2012): 699.
13. Kim, Keun Soo, Yue Zhao, Houk Jang, Sang Yoon Lee, Jong Min Kim, Kwang S. Kim, Jong-Hyun Ahn, Philip Kim, Jae-Young Choi, and Byung Hee Hong. "Large-scale pattern growth of graphene films for stretchable transparent electrodes." *Nature* 457, no. 7230 (2009): 706-710.
14. Li, Xuesong, Weiwei Cai, Jinho An, Seyoung Kim, Junghyo Nah, Dongxing Yang, Richard Piner et al. "Large-area synthesis of high-quality and uniform graphene films on copper foils." *Science* 324, no. 5932 (2009): 1312-1314.
15. Zhao, Liuyan, Kwang Taeg Rim, Hui Zhou, Rui He, Tony F. Heinz, Aron Pinczuk, George W. Flynn, and Abhay N. Pasupathy. "Influence of copper crystal surface on the

CVD growth of large area monolayer graphene." *Solid State Communications* 151, no. 7 (2011): 509-513.

16. Bistritzer, R., and A. H. MacDonald. "Moiré butterflies in twisted bilayer graphene." *Physical Review B* 84, no. 3 (2011): 035440.
17. Moon, Pilkyung, and Mikito Koshino. "Energy spectrum and quantum Hall effect in twisted bilayer graphene." *Physical Review B* 85, no. 19 (2012): 195458.
18. Shallcross, S., S. Sharma, E. Kandelaki, and O. A. Pankratov. "Electronic structure of turbostratic graphene." *Physical Review B* 81, no. 16 (2010): 165105.
19. Ohta, Taisuke, Aaron Bostwick, Thomas Seyller, Karsten Horn, and Eli Rotenberg. "Controlling the electronic structure of bilayer graphene." *Science*313, no. 5789 (2006): 951-954.
20. Novoselov, K. S., Edward McCann, S. V. Morozov, Vladimir I. Fal'ko, M. I. Katsnelson, U. Zeitler, D. Jiang, F. Schedin, and A. K. Geim. "Unconventional quantum Hall effect and Berry's phase of 2π in bilayer graphene." *Nature physics* 2, no. 3 (2006): 177-180.
21. Castro, Eduardo V., K. S. Novoselov, S. V. Morozov, N. M. R. Peres, JMB Lopes Dos Santos, Johan Nilsson, F. Guinea, A. K. Geim, and AH Castro Neto. "Biased bilayer graphene: semiconductor with a gap tunable by the electric field effect." *Physical Review Letters* 99, no. 21 (2007): 216802.
22. Bistritzer, Rafi, and Allan H. MacDonald. "Moiré bands in twisted double-layer graphene." *Proceedings of the National Academy of Sciences* 108, no. 30 (2011): 12233-12237.

23. Li, Hongyang, Hao Ying, Xiangping Chen, Denis L. Nika, Alexandr I. Cocemasov, Weiwei Cai, Alexander A. Balandin, and Shanshan Chen. "Thermal conductivity of twisted bilayer graphene." *Nanoscale* 6, no. 22 (2014): 13402-13408.
24. He, Rui, Ting-Fung Chung, Conor Delaney, Courtney Keiser, Luis A. Jauregui, Paul M. Shand, C. C. Chancey, Yanan Wang, Jiming Bao, and Yong P. Chen. "Observation of low energy Raman modes in twisted bilayer graphene." *Nano letters* 13, no. 8 (2013): 3594-3601.
25. Kim, Kwanpyo, Sinisa Coh, Liang Z. Tan, William Regan, Jong Min Yuk, Eric Chatterjee, M. F. Crommie, Marvin L. Cohen, Steven G. Louie, and A. Zettl. "Raman spectroscopy study of rotated double-layer graphene: misorientation-angle dependence of electronic structure." *Physical review letters* 108, no. 24 (2012): 246103.
26. Lui, Chun Hung, Leandro M. Malard, SukHyun Kim, Gabriel Lantz, François E. Laverge, Riichiro Saito, and Tony F. Heinz. "Observation of layer-breathing mode vibrations in few-layer graphene through combination Raman scattering." *Nano letters* 12, no. 11 (2012): 5539-5544.
27. Malard, L. M., M. A. Pimenta, G. Dresselhaus, and M. S. Dresselhaus. "Raman spectroscopy in graphene." *Physics Reports* 473, no. 5 (2009): 51-87.
28. Ferrari, Andrea C. "Raman spectroscopy of graphene and graphite: disorder, electron–phonon coupling, doping and nonadiabatic effects." *Solid state communications* 143, no. 1 (2007): 47-57.

29. Yan, Jia-An, W. Y. Ruan, and M. Y. Chou. "Phonon dispersions and vibrational properties of monolayer, bilayer, and trilayer graphene: Density-functional perturbation theory." *Physical review B* 77, no. 12 (2008): 125401.

CHAPTER 3

Thermal conductivity of graphene with defects induced by electron beam irradiation

3.1. Introduction

3.1.1. Physics of heat conduction in graphene-based systems

For a given material, the net heat transfer is determined by Fourier's law, $q = -K\Delta T$, where q is the heat flux, K is the thermal conductivity and ΔT is the temperature gradient. For solid materials heat is carried by the electrons and acoustic phonons (i.e. ion-core vibrations in the crystal lattice), such that net thermal conductivity $K = K_p + K_e$, where K_p and K_e are the phonon and electron contributions, respectively. Unlike metals, where heat transport is dominated by the electrons, heat conduction in graphene-based systems is primarily dominated by the acoustic phonons owing to the strong in-place covalent sp^2 bonding that results in efficient heat transfer by lattice vibrations.[1,2] The contribution of electrons to heat conduction has been verified based on Wiedemann–Franz law,[3] $K_e/\sigma = (\pi^2/3)\,(k_B/e)^2\,T$, where K_e is the electron contribution to K, $\sigma = 1/\rho$ is the electrical conductivity, ρ is the electrical resistivity, k_B is the Boltzmann constant, and e is the charge of an electron). According to the kinetic theory of gases, the phonon thermal conductivity for 2D graphitic systems is expressed as:

$$K_p = (1/2)\, C_p\, \nu_s\, \lambda\ ,$$

where C_p is the specific heat capacity, ν_s is the phonon group velocity, which can be approximated the speed of sound, and λ is the phonon mean free path. For sample size (L)

much larger than the phonon mean free path (λ), $L >> \lambda$, the thermal transport is considered diffusive, i.e., the phonons undergo multiple scattering events. Fourier's law assumes diffusive transport. But for nanoscale samples with $L < \lambda$, the thermal transport is termed ballistic.[2,4]

Pristine single layer graphene (SLG) isolated by mechanical exfoliation has minimal defects or impurities, hence the phonons are primarily scattered only by other phonons. Thus the intrinsic thermal conductivity, limited by the crystal-lattice anharmonicity, is much higher (>5000 W m^{-1} K^{-1}).[5] However, large area graphene films synthesized by CVD inherently contain grain boundaries, impurities and external surfaces such as nucleation of bilayers. Furthermore, defects can be introduced during the device fabrication steps which include exposure of graphene film to electron beam and UV irradiation. Due to these reasons, the thermal transport is limited by extrinsic factors including phonon-rough-boundary or phonon-defect scattering, rather than by the intrinsic lattice dynamics.[6-8] The scattering of phonons in-plane from point-defects and external surfaces decreases the phonon mean free path, thus leading to lower thermal conductivity for CVD graphene. In the following two sections, we experimentally determine the thermal conductivity of CVD graphene and explore the effects of above mentioned extrinsic factors on thermal transport in graphene.

3.1.2. Effect of point defects on thermal conductivity

The exceptionally high intrinsic thermal conductivity, *K* of large suspended graphene samples has been experimentally verified using the opto-thermal Raman technique[9,10] and confirmed independently using scanning thermal microscopy

measurements.[11] This can be attributed to an unusually long mean free path (λ) of the long-wavelength phonons in two-dimensional (2-D) lattices.[2,12] Recent calculations by different methods suggested that the graphene sample size should be in the 100 μm[13,14] or even 1 mm[15] range in order to fully recover the intrinsic thermal conductivity, ranging from 4000–6000 W m^{-1} K^{-1} near RT. However, the thermal conductivity of graphene synthesized by the CVD is always lower than that of the mechanically exfoliated graphene due to extrinsic effects including polymer residue from nanofabrication,[8] edge roughness,[6] polycrystalline grain boundaries,[7] and disorder from contact with a substrate or a capping layer.[16] However, to date, there have been no quantitative experimental studies of the thermal conductivity dependence on the concentration of defects, N_D, in graphene. The only reported experimental study of the phonon – point-defect scattering in graphene utilized isotopically modified graphene.[17] The phonon scattering on isotope impurities is limited to the mass-difference term only. It does not include the local strain effects owing to missing atoms, bond breaking or presence of chemical impurities. It was established in ref. 17 that the dependence of the thermal conductivity on the isotope impurity (^{13}C) concentration is in line with the prediction of the well-established virtual crystal model[18] used to calculate thermal conductivity in alloy semiconductors such as Si_xGe_{1-x}[18] or $Al_xGa_{1-x}As$.[19] This model predicts the highest K for the material with either $x = 0$ or $(1 - x) = 0$ and a fast decrease to a minimum as x deviates from 0. The situation is expected to be different in materials with defects induced by irradiation.

The knowledge of the K dependence on the concentration of defects induced by irradiation can shed light on the strength of the phonon – point defect scattering in 2-D materials. The

change in the dimensionality results in different dependencies of the scattering rates on the phonon wavelengths in the processes of phonon relaxation by defects and grain boundaries.[6,20,21] In bulk 3-D crystals, the phonon scattering rate on point defects, $1/\tau_P$, varies as $\sim 1/f^4$ (where f is the phonon frequency).[21] Owing to the changed phonon density of states (PDOS), the phonon scattering rate in 2-D graphene has a different frequency dependence, $1/\tau^P \sim 1/f^3$, which can, in principle, affect the phonon MFP and the thermal conductivity. In addition to the fundamental scientific interest, a quantitative study of the dependence of K on N_D is important for practical applications of graphene in thermal management. The graphene and few-layer graphene (FLG) heat spreaders[22] will likely be produced by CVD while FLG thermal fillers in thermal interface materials (TIMs)[23] will be synthesized via the liquid phase exfoliation (LPE) technique. Both methods typically provide graphene with a large density of defects than that exfoliated from HOPG.

3.2. Experimental details

3.2.1. Graphene synthesis and transfer

The single layer graphene samples were synthesized using ambient pressure chemical vapor deposition (AP-CVD) on a Cu foil. Briefly, a polycrystalline Cu foil was cleaned to remove any surface oxides, loaded in a tube furnace and annealed for 2 h under flowing Ar and H_2 at 1030˚C. For the growth of graphene, methane (90 ppm) along with Ar and H_2 was introduced into the chamber for 20 min. After the growth, the furnace was turned off and cooled to room temperature in Ar and H_2 atmosphere. The SLG grains were transferred on to a gold TEM grid using a direct transfer method discussed in detail in Section 2.2.2. Fig. 3.1 shows a false-colored SEM image of graphene on a gold TEM grid.

Only the holes fully covered with graphene were chosen for the study to simplify the data extraction in the opto-thermal Raman technique.

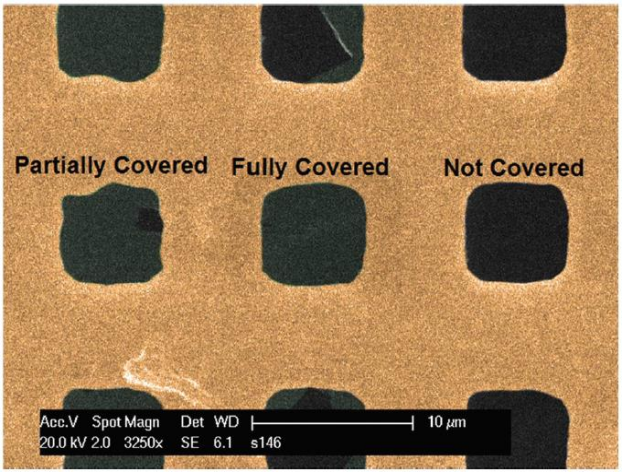

Figure. 3.1. False-colored SEM image of graphene transferred on gold TEM grid. Some holes are fully or partially covered with the graphene flake.

3.2.2. Opto-thermal Raman measurements

The opto-thermal Raman measurement is a non-contact steady state technique, which directly measures the thermal conductivity.[5] A schematic of measurement setup is

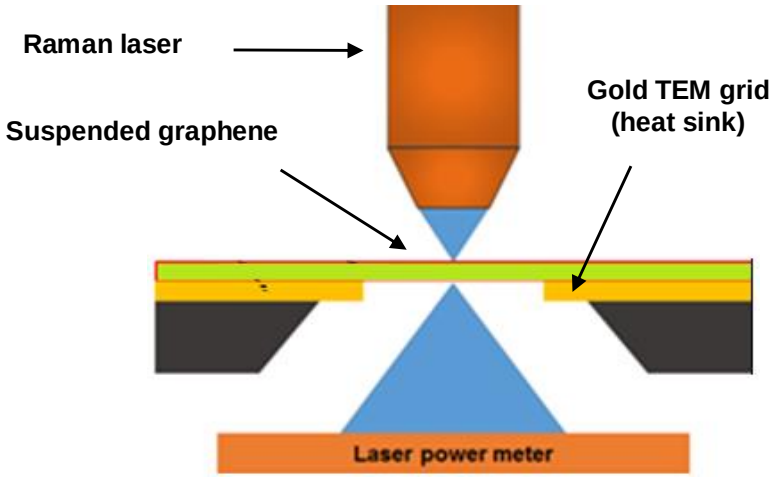

Figure. 3.2. Schematic representation of setup for opto-thermal Raman measurements of thermal conductivity for graphene suspended on a TEM grid.

shown in Fig. 3.2. Basically, the micro-Raman spectrometer has a dual function: first as a heater, causing local heating at the laser spot, and second as a thermometer, measuring the temperature rise from the Raman G-peak shift, caused by the laser heating. The measurement is done in two steps: the calibration procedure and the power-dependent Raman measurement. During the calibration, the Raman spectrum of graphene sample is recorded under low-power laser excitation (0.5 mW) to avoid local heating caused by the laser in a wide temperature range. In order to do this, the sample is placed inside a cold–hot cell (Linkam 600), where the temperature is controlled externally with steps of 10 °C and accuracy of ~0.1 °C. The samples are kept at least five minutes at each step to stabilize the temperature, and then the Raman G-peak positions are recorded. The procedure provides the position of the G-peak as a function of the sample temperature. In the second step of the opto-thermal measurements, the excitation laser power is intentionally increased to cause local heating in the suspended graphene, while the stage temperature is kept constant at room temperature. The spectral position of the Raman G-peak reveals the local temperature rise in response to the laser heating with the help of the calibration curve.

The temperature calibration and power measurement results are shown in Fig. 3.3(a) and 3.3(b), respectively. One can see from the temperature calibration plot that the dependence of the G peak spectral position on the sample temperature can be approximated as linear in the examined temperature interval. The extracted temperature coefficient χ_G = -0.013 $cm^{-1}/°C$ is in line with previous reports for graphene. The G-peak shift with increasing laser power (Fig. 3.3(b)) also shows an excellent linear dependence of the G-peak shift on the laser power. The portion of light absorbed by suspended graphene, which

causes the local heating, was measured directly by placing a power meter (*Ophir*) under the sample. To ensure accuracy, the absorbed power was measured for a graphene covered hole and on a reference empty hole. The difference in power readings corresponds to the power absorbed by graphene at a given laser wavelength λ. The measurement was repeated ten times at different laser power levels to determine the absorption coefficient of 5.68% ± 0.72% at the excitation laser wavelength of λ = 488 nm. The light absorption coefficient at λ < 500 nm, used in our experiments, is larger than the well-known long-wavelength limit, and it can increase further owing to surface contamination, defects, and bending.[24,25]

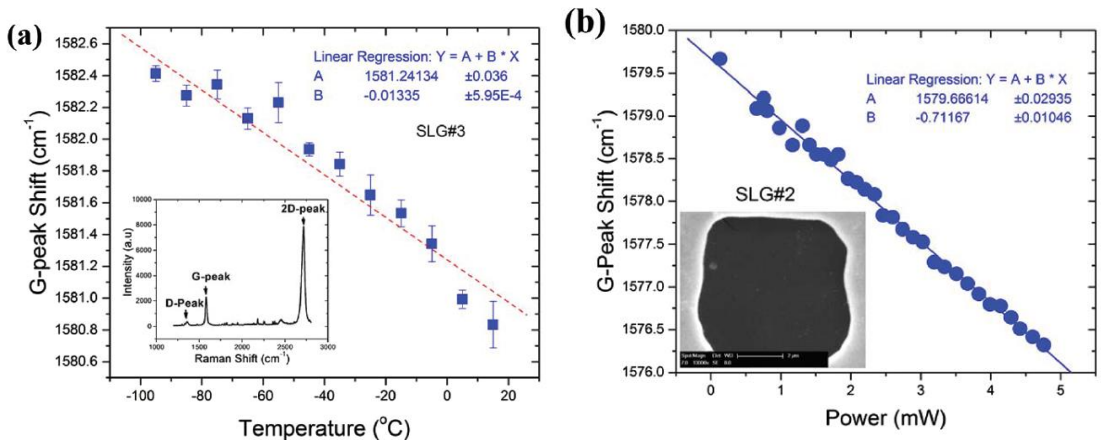

Figure 3.3. (a) Calibration dependence of the Raman G peak position of suspended SLG as a function of temperature before graphene exposure to electron beam. The inset shows a representative Raman spectrum of CVD graphene. **(b)** Raman G peak position dependence on power on excitation laser. The SEM image of this sample is depicted in the inset.

The slope of the $\omega_G(\Delta P)$ curve contains information about the value of thermal conductivity K, which can be extracted by solving the heat diffusion equation, knowing the sample geometry and temperature rise $\Delta T = \chi_G{}^{-1}\Delta\omega_G$ (where $\Delta\omega_G$ is the shift in the spectral position of G peak ω_G). The large sample size ensures that the phonon transport is

diffusive or partially diffusive. The "grey" phonon MFP in graphene is around ~800 nm near RT. The sample size of ~7.5 μm ensures that phonons scatter several times before reaching the edges. The thermal conductivity of suspended CVD graphene before introduction of defects was found to be ~1800 W m^{-1} K^{-1} near RT. This value is in agreement with the previous independent reports for suspended CVD graphene.[9,10] A possible presence of few grain boundaries and defects, introduced during synthesis or transfer, reduce the thermal conductivity of CVD graphene as compared to that of graphene obtained by mechanical exfoliation from HOPG.

3.2.3. Electron beam irradiation

The additional defects in the suspended graphene were introduced in a controllable way using low-energy electron beam irradiation.[26] The samples were irradiated under 20 keV electron beam using Philips XL-30 FEG field-emission system. The suspended graphene sample was exposed to continuous electron beam from electron gun with current varying from ~3 nA to ~10 nA controlled by the beam spot size. Before each irradiation step, a Faraday cup was used to read the beam current at the desired spot size. A constant magnification was maintained during all irradiation steps in order to keep the irradiated area constant (6.6×10^7 nm^2). As a result, the dose density was controlled by the irradiation time. The irradiation process was done inside a vacuum chamber with the pressure below 10^{-4} Torr.

The Raman spectra of the suspended graphene samples were recorded after each irradiation step. Fig. 3.4(a) shows the evolution of the D and D′ peaks in the Raman spectrum of single layer graphene after each irradiation step. It can be seen that the D to G

peak intensity ratio, I_D/I_G, increases from 0.13 for as-grown CVD graphene all the way to 1.00, after four steps of the electron beam irradiation. The presence of the D peak in the spectrum before irradiation indicates a background defect concentration characteristic for CVD graphene and explains *K* values somewhat below the bulk graphite limit. The

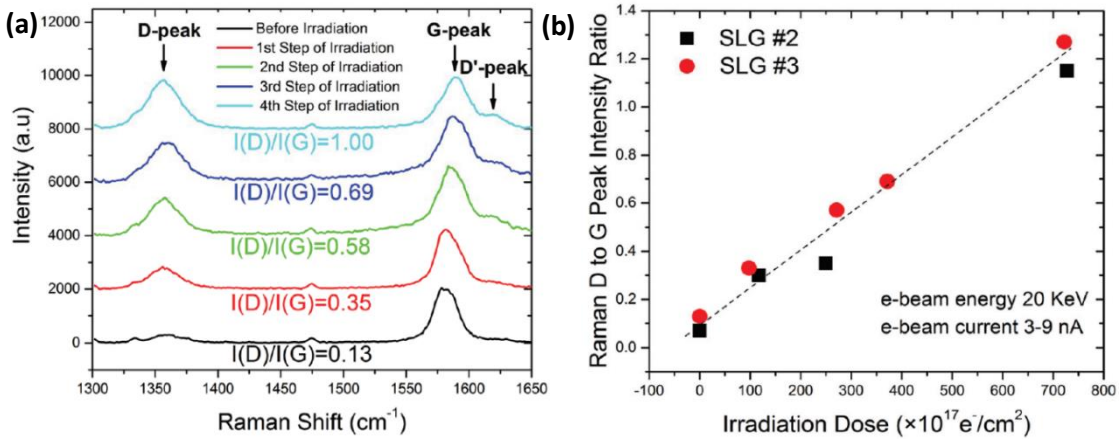

Figure 3.4. (a) Evolution of Raman spectrum under electron beam irradiation. As the sample is exposed to the electron beam, the Raman D peak intensity increases resulting in a D-to-G peak intensity ratio change from ~0.13 to ~1.00; **(b)** Correlation of the Raman D-to-G peak intensity ratio with the electron beam irradiation dose.

evolution of the Raman spectrum under irradiation was used for quantifying the density of defects, N_D, following an empirical correlation:[27,28]

$$N_D = \frac{(1.8 \pm 0.5) \times 10^{22}}{\lambda^4} \left(\frac{I_D}{I_G}\right)$$

It is known that the above correlation is valid for a relatively low defect density regime. This criterion was met in the reported experiments. The defect density increases linearly with the Raman D to G peak intensity ratio. To show the correlation between the density of defects and the electron beam irradiation dose, we have plotted the Raman D to G peak intensity ratio, I_D/I_G, as a function of the total irradiation dose (Fig. 3.4(b)). The

linear dependence is clearly seen as expected for the low defect density regime.[26] The opto-thermal Raman measurements were performed after each irradiation step. The dependence of the G-peak shift on the temperature and total power is presented in Fig. 3.5. The temperature coefficient of the Raman G-peak, χ_G, was not significantly affected by the

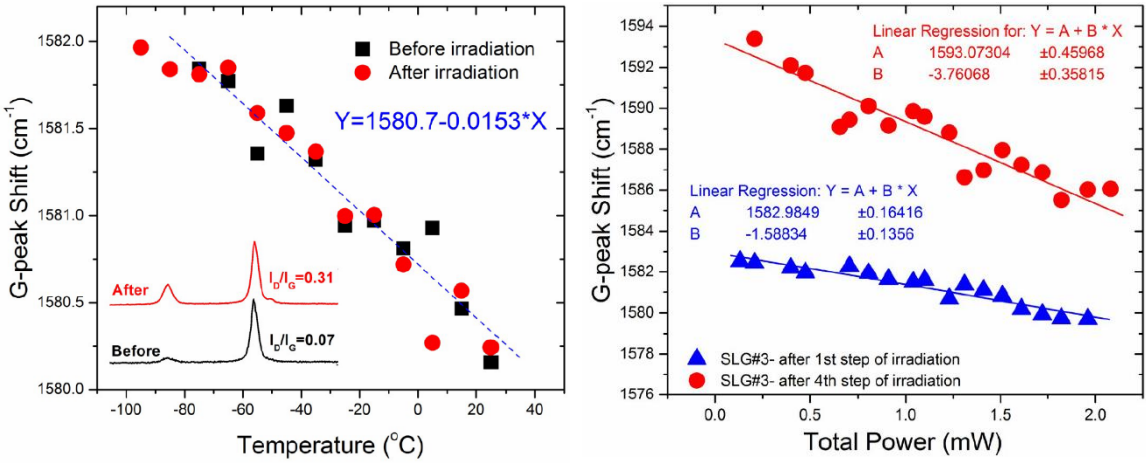

Figure 3.5. (a) Calibration measurement for SLG before (black squares) and after (red circles) the irradiation procedure. **(b)** Power dependent Raman measurement results after the 1st (blue triangles) and 4th (red circles) steps of irradiation were applied. One should notice the increase of the slope factor, which is directly related to the suppression of thermal conductivity.

defect density. But the slope of the $\omega_G(\Delta P)$ curve increased significantly after each step of irradiation, indicating a decrease in thermal conductivity. In measuring the $\omega_G(\Delta P)$ dependence, we had to keep the power level small enough in order to avoid local healing of defects via heating.

In Fig. 3.6 we present the extracted thermal conductivity, K, as a function of the defect density, N_D, by squares, circles and triangles corresponding to three suspended flakes of graphene. The details of the thermal data extraction using COMSOL simulation have been reported in ref. 12. For the small defect densities, $N_D < 1.2 \times 10^{11}$ cm^{-2}, the

thermal conductivity decreased with increasing N_D. It can be approximated with the linear dependence $K = 1990 - 116 \times N_D$ [W m^{-1} K^{-1}]. In the N_D = 0 limit, the thermal conductivity K = 1990 W m^{-1} K^{-1} was still smaller than that of the ideal basal plane of HOPG due to the background defects and possible grain boundaries present in CVD graphene before irradiation. The presence of defects before irradiation was evidenced from D peak in the Raman spectrum. At the defect density of $N_D \sim 1.5 \times 10^{11}$ cm^{-2}, one can see an intriguing change in the $K(N_D)$ slope. It can be interpreted as a strong reduction in the rate of the decrease of K with increasing concentration N_D or the onset of saturation. The thermal conductivity in this region is still rather high $K \sim 400$ W m^{-1} K^{-1}. This is clearly above the amorphous carbon limit.[2]

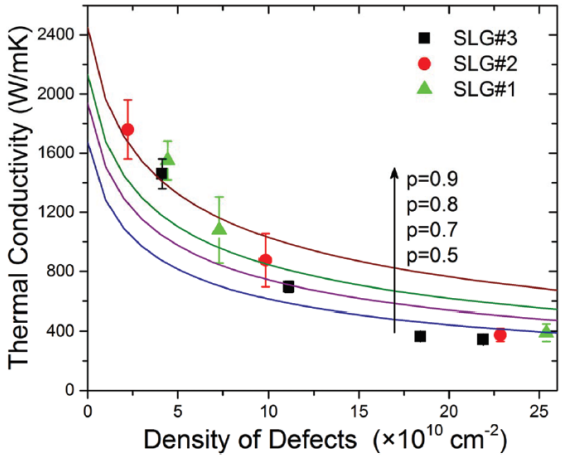

Figure 3.6. Dependence of the thermal conductivity on the density of defects. The experimental data are shown by squares, circles and triangles. The solid curves are calculated using the BTE with different values of the specularity parameter p.

3.3. Discussion

For theoretical interpretation of the measured behavior of the thermal conductivity we employed both a BTE analysis and MD simulations. The details of our BTE and MD approach are provided in Appendix B. Briefly, for analysis of our experimental data, we take into account three main mechanisms of phonon scattering: phonon–phonon Umklapp

(U) scattering, phonon – rough edge scattering (also referred to as boundary (B) scattering), and phonon – point-defect (P_D) scattering. The strength of the phonon scattering on defects is determined by the mass-difference parameter $\zeta = (\Delta M/M)^2$, where M is the mass of carbon atom and $\Delta M = M - M_D$ is the difference between masses of a carbon atom and a defect. The value of ζ strongly depends on the nature of defects. In our BTE analysis, we used ζ as a fitting parameter to the experimental data. Within our model assumptions, the agreement with the experimental results is reached for $\zeta = 590$. The important conclusion from the BTE modeling is that the observed weakening $K(N_D)$ dependence can be reproduced via interplay of the three main phonon scattering mechanisms – Umklapp scattering due to lattice anharmonicity, mass-difference scattering, and rough edge scattering.

Let us now consider a possible nature of defects in our samples and their effect on the thermal conductivity as revealed from MD simulations. The electron energies of 20 keV used in the electron beam irradiation process are less than the knockout threshold energy of 80 keV.[26,29,30] Such irradiation is only sufficient to overcome the energy barrier required for breaking of the carbon–carbon bond and initiating reaction with any residual impurities such as H_2O and O_2 on the surface of graphene. This reaction results in functionalization of graphene with –OH and –C=O groups. Prior studies have shown that the –C=O configuration is energetically more favorable than –OH, and the transition of –OH and other functional groups into the energetically stable –C=O configuration can occur especially when they are annealed.[31] The energy barrier for the diffusion of –OH and epoxy groups is around 0.5–0.7 eV,[32] which corresponds to a diffusion rate $\sim 10^2\ s^{-1}$ as calculated

from transition-state theory, assuming a typical phonon frequency range in graphene. For this reason, the functional groups can be mobile at the temperature of the thermal experiments (~350 K). Upon continuous electron beam irradiation, two epoxy or hydroxyl group can come together and release an O_2 molecule.[33] When the coverage of functional groups is high, detectable amounts of CO/CO_2 can be released creating vacancies in the graphene lattice.[34] The presence of –OH and –C=O functional groups can be the reason for stronger phonon – defect scattering than that predicted by BTE models with vacancies only (and the resulting large ζ required for fitting to the experimental data). Our MD simulations show that a combination of single and double vacancy defects can also account for the experimentally observed thermal conductivity dependence on the defect concentration. The absolute value at the zero-defect limit is lower than the experimental due to the domain-size limitation in the simulation.

As one can see from Fig. 3.7, the thermal conductivity decreases drastically for N_D increasing from 2 × 10^{10} cm^{-2} to 10 × 10^{10} cm^{-2} and subsequently reaches a near-constant value at the higher concentrations of defects. This value is substantially above the amorphous carbon limit – in

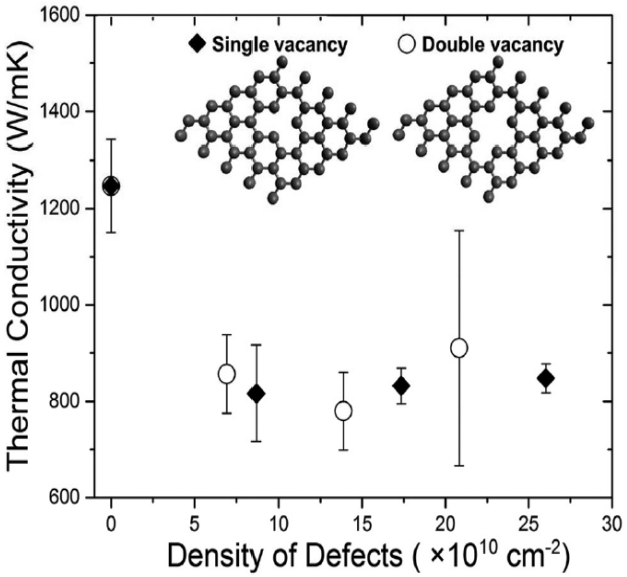

Figure. 3.7. MD simulation results for thermal conductivity of graphene with single and double vacancy defects. The simulated defect structures are depicted in the inset.

line with the experiment. According to this model scenario, upon irradiation, –C=O and other functionalized defects are formed that strongly reduce the thermal conductivity. Continuous irradiation results in the creation of single and double vacancies. The increase in their concentration does not lead to pronounced *K* reduction, which approaches an approximately constant value for the N_D range that was investigated. It can be explained in the following way. As more defects are introduced in graphene through irradiation the additional defect sites serve as scattering centers for phonons with wavelengths shorter than the distance between two vacancies. The delocalized long-wavelength phonons, that carry a significant fraction of heat, are less affected by extra defects that are closely spaced compared to those introduced at the previous irradiation step. At some irradiation dose, the increase in the phonon scattering rate of the delocalized modes due to extra defects is substantially smaller than that of the short-ranged localized modes. Hence, after a certain critical N_D the thermal conductivity effectively saturates. The weakening of the $K(N_D)$ dependence observed experimentally and revealed in the present MD simulation is in line with reported computational results performed for graphene and graphene ribbons under various assumptions about the nature of defects.[34-37]

We further analyzed experimental Raman data to confirm the presence of vacancies in the irradiated graphene following the methodology developed in ref. 38. In this approach, the type of defects is determined from the ratio of intensities of D and D′ peaks, $I_D/I_{D'}$. It has been shown that $I_D/I_{D'}$ in graphene attains its maximum ($\simeq$13) for the defects associated with sp^3 hybridization, decreases for the vacancy-like defects ($\simeq$7), and reaches a minimum for the boundary-like defects ($\simeq$3.5). Following this method,[38] the results

shown in Fig. 3.8 confirm the presence of vacancy type defects in our irradiated graphene sample ($I_D/I_{D'} \simeq 7$). It is known that the intensity of the D band depends not only on the concentration of defects, but also on the type of defects,[39] and only defects that are capable of scattering electrons between the two valleys K and K′ of the Brillouin zone can contribute to the D band.[40-42] For this reason, not all types of defects in graphene can be detected by Raman spectroscopy. However, our Raman data confirm the presence of vacancies supporting the theoretical assumptions.

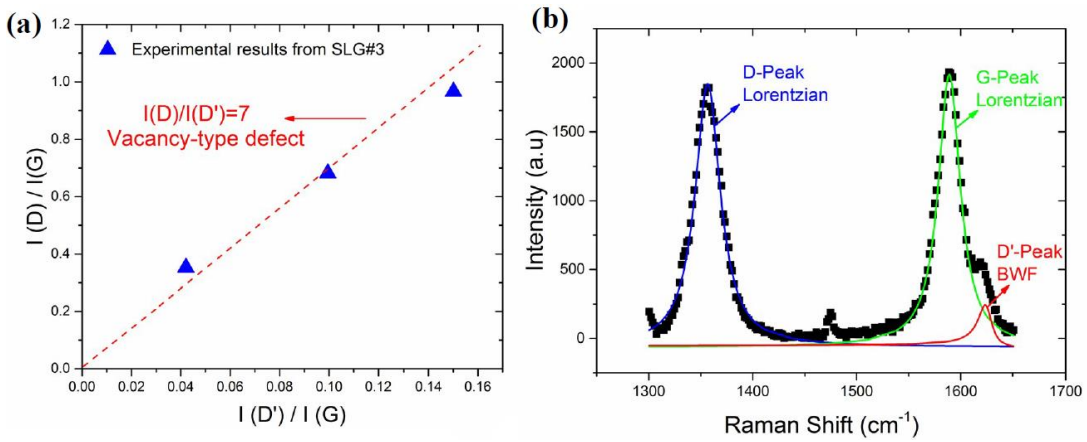

Figure 3.8. **(a)** Nature of defects was found to be mostly vacancies based on Raman D to D' peak intensity ratio of ~7, which has been attributed to vacancy type defect. (b) Raman D and G peak was fitted with Lorentzian function while D' peak was fitted using Fano line shape.

3.4. Conclusions

We investigated the thermal conductivity of suspended CVD graphene as a function of the defect density. The defects were introduced by the low-energy electron beams and quantified by the Raman D-to-G peak intensity ratios. It was found that as the defect density changes from 2.0×10^{10} cm^{-2} to 1.8×10^{11} cm^{-2} the thermal conductivity reduces from $\sim(1.8 \pm 0.2) \times 10^3$ W m^{-1} K^{-1} to $\sim(4.0 \pm 0.2) \times 10^2$ W m^{-1} K^{-1} near RT. At higher defect density the thermal conductivity revealed an intriguing weakening of the $K(N_D)$

dependence. This behavior was explained theoretically within the Boltzmann transport equation and molecular dynamics approaches. The obtained results contribute to understanding the acoustic phonon point defect scattering in 2-D materials. Our data indicating rather large values of thermal conductivity for graphene with defects adds validity to the proposed practical applications of graphene in thermal management.

3.5. References

1. Klemens, P. G. "Theory of the a-plane thermal conductivity of graphite." *Journal of Wide Bandgap Materials* 7, no. 4 (2000): 332-339.
2. Balandin, Alexander A. "Thermal properties of graphene and nanostructured carbon materials." *Nature materials* 10, no. 8 (2011): 569-581.
3. Yigen, S., and A. R. Champagne. "Wiedemann–Franz Relation and Thermal-Transistor Effect in Suspended Graphene." *Nano letters* 14, no. 1 (2013): 289-293.
4. Pumarol, Manuel E., Mark C. Rosamond, Peter Tovee, Michael C. Petty, Dagou A. Zeze, Vladimir Falko, and Oleg V. Kolosov. "Direct nanoscale imaging of ballistic and diffusive thermal transport in graphene nanostructures." *Nano letters* 12, no. 6 (2012): 2906-2911.
5. Balandin, Alexander A., Suchismita Ghosh, Wenzhong Bao, Irene Calizo, Desalegne Teweldebrhan, Feng Miao, and Chun Ning Lau. "Superior thermal conductivity of single-layer graphene." *Nano letters* 8, no. 3 (2008): 902-907.
6. Nika, D. L., E. P. Pokatilov, A. S. Askerov, and A. A. Balandin. "Phonon thermal conduction in graphene: Role of Umklapp and edge roughness scattering." *Physical Review B* 79, no. 15 (2009): 155413.

7. Serov, Andrey Y., Zhun-Yong Ong, and Eric Pop. "Effect of grain boundaries on thermal transport in graphene." *Applied Physics Letters* 102, no. 3 (2013): 033104.
8. Pettes, Michael Thompson, Insun Jo, Zhen Yao, and Li Shi. "Influence of polymeric residue on the thermal conductivity of suspended bilayer graphene." *Nano letters* 11, no. 3 (2011): 1195-1200.
9. Cai, Weiwei, Arden L. Moore, Yanwu Zhu, Xuesong Li, Shanshan Chen, Li Shi, and Rodney S. Ruoff. "Thermal transport in suspended and supported monolayer graphene grown by chemical vapor deposition." *Nano letters* 10, no. 5 (2010): 1645-1651.
10. Chen, Shanshan, Arden L. Moore, Weiwei Cai, Ji Won Suk, Jinho An, Columbia Mishra, Charles Amos et al. "Raman measurements of thermal transport in suspended monolayer graphene of variable sizes in vacuum and gaseous environments." *ACS nano* 5, no. 1 (2010): 321-328.
11. Hwang, Gwangseok, and Ohmyoung Kwon. "Measuring the size dependence of thermal conductivity of suspended graphene disks using null-point scanning thermal microscopy." *Nanoscale* 8, no. 9 (2016): 5280-5290.
12. Ghosh, Suchismita, Wenzhong Bao, Denis L. Nika, Samia Subrina, Evghenii P. Pokatilov, Chun Ning Lau, and Alexander A. Balandin. "Dimensional crossover of thermal transport in few-layer graphene." *Nature materials* 9, no. 7 (2010): 555-558.
13. Nika, Denis L., Artur S. Askerov, and Alexander A. Balandin. "Anomalous size dependence of the thermal conductivity of graphene ribbons." Nano letters 12, no. 6 (2012): 3238-3244.

14. Mei, S., L. N. Maurer, Z. Aksamija, and I. Knezevic. "Full-dispersion Monte Carlo simulation of phonon transport in micron-sized graphene nanoribbons." Journal of Applied Physics 116, no. 16 (2014): 164307.
15. Fugallo, Giorgia, Andrea Cepellotti, Lorenzo Paulatto, Michele Lazzeri, Nicola Marzari, and Francesco Mauri. "Thermal conductivity of graphene and graphite: collective excitations and mean free paths." Nano letters 14, no. 11 (2014): 6109-6114.
16. Seol, Jae Hun, Insun Jo, Arden L. Moore, Lucas Lindsay, Zachary H. Aitken, Michael T. Pettes, Xuesong Li et al. "Two-dimensional phonon transport in supported graphene." *Science* 328, no. 5975 (2010): 213-216.
17. Chen, Shanshan, Qingzhi Wu, Columbia Mishra, Junyong Kang, Hengji Zhang, Kyeongjae Cho, Weiwei Cai, Alexander A. Balandin, and Rodney S. Ruoff. "Thermal conductivity of isotopically modified graphene." *Nature materials* 11, no. 3 (2012): 203-207.
18. Abeles, B. "Lattice thermal conductivity of disordered semiconductor alloys at high temperatures." *Physical Review* 131, no. 5 (1963): 1906.
19. Liu, Weili, and Alexander A. Balandin. "Thermal conduction in AlxGa1-xN alloys and thin films." *Journal of Applied Physics* 97, no. 7 (2005): 73710-73710.
20. Klemens, P. G. "Theory of the a-plane thermal conductivity of graphite." *Journal of Wide Bandgap Materials* 7, no. 4 (2000): 332-339.
21. Klemens, P. G., and D. F. Pedraza. "Thermal conductivity of graphite in the basal plane." *Carbon* 32, no. 4 (1994): 735-741.

22. Subrina, Samia, Dmitri Kotchetkov, and Alexander A. Balandin. "Heat removal in silicon-on-insulator integrated circuits with graphene lateral heat spreaders." *IEEE Electron Device Letters* 30, no. 12 (2009): 1281-1283.
23. Shahil, Khan MF, and Alexander A. Balandin. "Graphene–multilayer graphene nanocomposites as highly efficient thermal interface materials." *Nano letters* 12, no. 2 (2012): 861-867.
24. Mak, Kin Fai, Matthew Y. Sfeir, Yang Wu, Chun Hung Lui, James A. Misewich, and Tony F. Heinz. "Measurement of the optical conductivity of graphene." *Physical review letters* 101, no. 19 (2008): 196405.
25. Santoso, Iman, Ram Sevak Singh, Pranjal Kumar Gogoi, Teguh Citra Asmara, Dacheng Wei, Wei Chen, Andrew TS Wee, Vitor M. Pereira, and Andrivo Rusydi. "Tunable optical absorption and interactions in graphene via oxygen plasma." *Physical Review B* 89, no. 7 (2014): 075134.
26. Teweldebrhan, Desalegne, and Alexander A. Balandin. "Modification of graphene properties due to electron-beam irradiation." *Applied Physics Letters* 94, no. 1 (2009): 013101.
27. Cançado, L. Gustavo, A. Jorio, EH Martins Ferreira, F. Stavale, C. A. Achete, R. B. Capaz, M. V. O. Moutinho, A. Lombardo, T. S. Kulmala, and A. C. Ferrari. "Quantifying defects in graphene via Raman spectroscopy at different excitation energies." *Nano letters* 11, no. 8 (2011): 3190-3196.
28. Lucchese, Márcia Maria, F. Stavale, EH Martins Ferreira, C. Vilani, M. V. O. Moutinho, Rodrigo B. Capaz, C. A. Achete, and A. Jorio. "Quantifying ion-induced

defects and Raman relaxation length in graphene." *Carbon* 48, no. 5 (2010): 1592-1597.

29. Kotakoski, J., A. V. Krasheninnikov, U. Kaiser, and J. C. Meyer. "From point defects in graphene to two-dimensional amorphous carbon." *Physical Review Letters* 106, no. 10 (2011): 105505.
30. Banhart, Florian, Jani Kotakoski, and Arkady V. Krasheninnikov. "Structural defects in graphene." *ACS nano* 5, no. 1 (2010): 26-41.
31. Bagri, Akbar, Rassin Grantab, N. V. Medhekar, and V. B. Shenoy. "Stability and formation mechanisms of carbonyl-and hydroxyl-decorated holes in graphene oxide." *The Journal of Physical Chemistry C* 114, no. 28 (2010): 12053-12061.
32. Zhou, Si, and Angelo Bongiorno. "Origin of the chemical and kinetic stability of graphene oxide." *Scientific reports* 3 (2013).
33. Larciprete, Rosanna, Stefano Fabris, Tao Sun, Paolo Lacovig, Alessandro Baraldi, and Silvano Lizzit. "Dual path mechanism in the thermal reduction of graphene oxide." *Journal of the American Chemical Society* 133, no. 43 (2011): 17315-17321.
34. Zhang, Hengji, Geunsik Lee, and Kyeongjae Cho. "Thermal transport in graphene and effects of vacancy defects." *Physical Review B* 84, no. 11 (2011): 115460.
35. Hao, Feng, Daining Fang, and Zhiping Xu. "Mechanical and thermal transport properties of graphene with defects." *Applied physics letters* 99, no. 4 (2011): 041901.
36. Mortazavi, Bohayra, and Saïd Ahzi. "Thermal conductivity and tensile response of defective graphene: a molecular dynamics study." *Carbon* 63 (2013): 460-470.

37. Haskins, Justin, Alper Kınacı, Cem Sevik, Hâldun Sevinçli, Gianaurelio Cuniberti, and Tahir Çağın. "Control of thermal and electronic transport in defect-engineered graphene nanoribbons." *ACS nano* 5, no. 5 (2011): 3779-3787.

38. Eckmann, Axel, Alexandre Felten, Artem Mishchenko, Liam Britnell, Ralph Krupke, Kostya S. Novoselov, and Cinzia Casiraghi. "Probing the nature of defects in graphene by Raman spectroscopy." *Nano letters* 12, no. 8 (2012): 3925-3930.

39. Venezuela, Pedro, Michele Lazzeri, and Francesco Mauri. "Theory of double-resonant Raman spectra in graphene: intensity and line shape of defect-induced and two-phonon bands." *Physical Review B* 84, no. 3 (2011): 035433.

40. Cancado, L. G., M. A. Pimenta, B. R. A. Neves, M. S. S. Dantas, and A. Jorio. "Influence of the atomic structure on the Raman spectra of graphite edges." *Physical review letters* 93, no. 24 (2004): 247401.

41. Casiraghi, Cinzia, Achim Hartschuh, Huihong Qian, S. Piscanec, Carsten Georgi, A. Fasoli, K. S. Novoselov, D. M. Basko, and A. C. Ferrari. "Raman spectroscopy of graphene edges." *Nano letters* 9, no. 4 (2009): 1433-1441.

42. Krauss, Benjamin, Péter Nemes-Incze, Viera Skakalova, László P. Biro, Klaus von Klitzing, and Jurgen H. Smet. "Raman scattering at pure graphene zigzag edges." *Nano letters* 10, no. 11 (2010): 4544-4548.

CHAPTER 4

Band-gap Engineering of Graphene

4.1. Introduction

It is a general consensus that the MOSFET scaling is approaching its limit as FETs with shorter gates suffer from degraded electrostatics and short channel effects.[1] The scaling theory predicts that FETs with a thinner gate-controlled region will be more robust against short-channel effects.[2,3] Hence, significant research is directed towards exploring newer materials and device concepts ensure improvement in device performance. This opens up possibilities for FETs with two-dimensional materials such as graphene and transition metal dichalcogenides (TMDs), which are one atomic layer thick, as the channel material.[3,4] Owing to exceptional electrical properties such as high charge mobility, ambipolar nature and quantum hall effect, graphene is one the materials that is considered to be a strong candidate for post-Si electronics by the International Technology Roadmap for Semiconductors (ITRS).[5]

The electronic band-structure of conventional semiconductors consists of valence and conduction bands that are parabolic and separated by a gap of size E_g, the band-gap of the semiconductor (Fig. 4.1(a)). The band-gap values for typical semiconductors are 1.1 eV for Si, 0.7 eV for Ge and 1.4 eV for GaAs. However, pristine graphene does not have a band-gap and the band-structure consists of cone-shaped valence and conduction bands that touch each other at the K points in the Brillouin zone (Fig. 4.1(b)).[6] The transfer characteristics for a typical graphene-FET and a Si MOSFET are shown in Fig. 4.1(c). For

a conventional semiconductor like Si, decreasing the gate voltage shifts the Fermi level into the band-gap region where the carrier density, and hence the drain current, is negligible and the transistor is said to be switched off. The ability of Si FETs to completely switch off results in extremely low power dissipation in static mode and thus facilitates its operation as a switch with on–off ratios I_{ON}/I_{OFF} in the range of 10^4 - 10^7. The typical static drain current in graphene inverters[7] is ~270 μA μm^{-1} at a supply voltage V_{DD} = 2.5 V, in contrast to the much smaller leakage drain current ~100nA μm^{-1} at V_{DD} = 0.75 V in 22 nm node high-performance Si logic transistors.[8] This large non-zero off-state drain current in graphene is due to its zero band-gap and is responsible for the low I_{ON}/I_{OFF} for graphene FETs. This is a major obstacle for graphene FETs and limits its use for applications.[9]

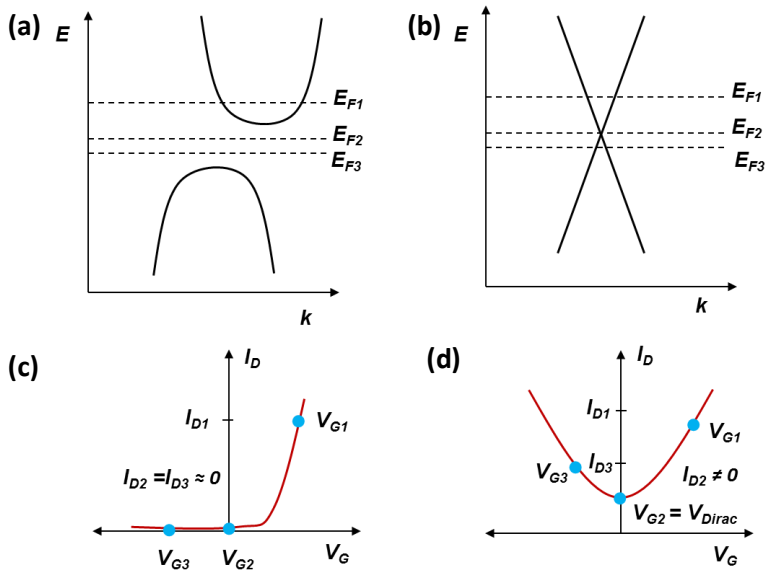

Figure 4.1 Electronic bandstructure diagram of **(a)** conventional semiconductor, **(b)** Single-layer graphene; Transfer characteristics for **(c)** conventional semiconductor, **(d)** Single-layer graphene.

The issue of zero band-gap of pristine graphene has sparked a lot of research for ways to engineer a band-gap using different methods including confinement of charge

carriers in one dimensional structures like graphene nanoribbons[10,11] applying a vertical bias to bilayer graphene,[12] and chemical modification of graphene.[13] In particular, fabrication of one-dimensional structures like graphene nanoribbons (GNRs) is considered particularly elegant since it offers control over extent of bandgap introduced by simply varying the dimensions. Analogous to carbon nanotubes,[14] the band-gap for a GNR device is inversely proportional to the ribbon width (Fig. 4.2(a)). Bandgaps in the range of 300-400 meV have been demonstrated experimentally for GNRs with less than 15 nm width.[10,11] However, fabrication of GNRs with widths down to sub-10 nm is challenging and the resulting GNRs suffer from edge roughness and edge site defects.[15,16] These defects significantly affect the band gap, induce doping and degrade the mobility of charge carriers along the length of the ribbon. The highest quality GNRs with smooth, well-defined edges have been synthesized by longitudinal unzipping of carbon nanotubes.[11] However, this technique results in isolated ribbons with undefined shape and is therefore not practical for FET device fabrication. Most practical fabrication techniques for GNRs are based on a top down approach that involves deposition of large area graphene on a substrate followed by

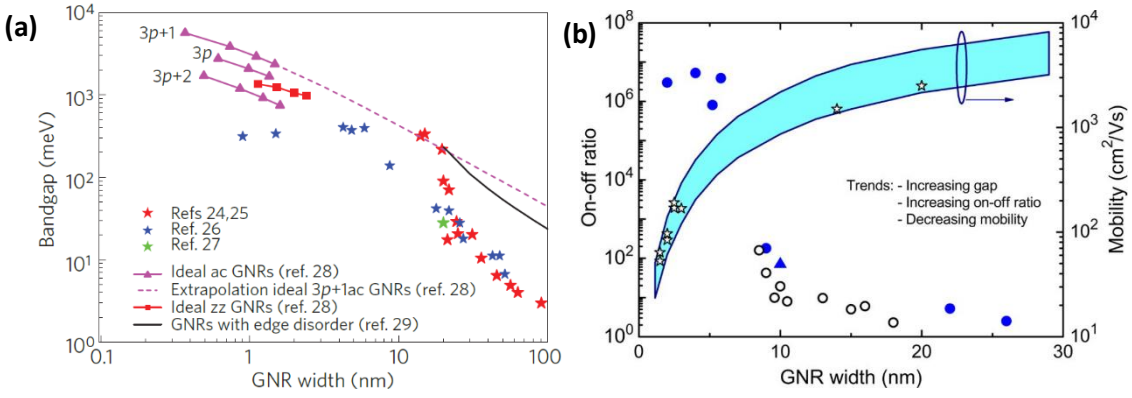

Figure 4.2 (a) Bandgap versus GNR width based on experiments and calculations,[3] **(b)** Effect of GNR width on I_{ON}/I_{OFF} ratio and mobility of experimental GNR-FETs.[9]

anisotropic etching using a mask, resulting in an array of GNRs.[15,16] The edge roughness and defects are primarily introduced during this etching step that involves removal of graphene using dry plasma-based etching.

In this chapter, we discuss two different top down approaches for synthesis of GNR array with varying widths. The first approach is using convention electron-beam lithography (EBL). Briefly, large area graphene synthesized using CVD is transferred on Si/SiO_2 and coated with a thin-layer of poly(methyl methacrylate) (PMMA), a positive e-beam resist, which acts like an etch mask.[17,18] The resist layer is patterned using electron-beam lithography and the exposed graphene is removed using oxygen-based reactive-ion etching (RIE). Finally, the PMMA layer is dissolved and this results in an array of GNRs with widths between 50-200 nm. As discussed above, these widths are not narrow enough to open up a sufficient band gap in graphene. So, we propose a second top-down approach that utilizes an array of metal nanowires (NWs) to act like an etch mask. Briefly, the metal nanowire array is fabricated using a superlattice nanowire pattern (SNAP) transfer process,[19,20] which results in Pt NWs with widths down to 8 nm. These narrow NWs act like an etch mask and the graphene is etched using RIE. We investigate the nature of the edge defect sites in detail using material characterization techniques including Raman spectroscopy and x-ray photoelectron spectroscopy (XPS). Further, the effect of thermal annealing treatments to reduce the concentration of edge defects was explored. In the final section, we explore the applications of these GNR-FETs devices as a gas sensor and compare the sensitivity to its graphene counterpart.

4.2. Experimental Details

4.2.1. Synthesis and transfer of large area graphene

Large area single-layer graphene (SLG) was synthesized using ambient pressure chemical vapor deposition (AP-CVD) on a Cu foil. A polycrystalline Cu foil (99.8% purity, 0.025 mm thickness) was cleaned and loaded into the CVD chamber and the furnace temperature was ramped to 1030˚C while flowing Ar (300 sccm) and H_2 (15 sccm) and the foil was annealed for 2 h. For the growth of graphene, low concentration of methane (90 ppm in Ar) and H_2 were introduced into the chamber for 20 min at 375 sccm and 15 sccm, respectively. After the growth, the furnace was turned off and cooled to room temperature in Ar and H_2 atmosphere. Next, the graphene was transferred on Si/SiO_2 substrate using a conventional polymer-based method. Briefly, the Cu foil with graphene was spin-coated with a layer of poly(methyl methacrylate) (4% in anisole) at 2000 rpm and baked at 180˚C for 10 min. The copper foil was then etched in 0.2 M $(NH_4)_2S_2O_8$ and washed repeatedly with DI water. The resulting PMMA/graphene film floating on the surface of DI water was transferred to a Si/SiO_2 chip and dried in air. The PMMA layer was dissolved in acetone and graphene chip was annealed at 250°C in air to remove the polymer residues and improve the contact between the graphene film and substrate.

4.2.2. FET device fabrication

Field-effect transistors (FETs) with SLG as the channel material were fabricated on Si/SiO_2 (highly doped p-type Si substrate with 300 nm of SiO_2 deposited using thermal oxidation) using conventional photolithography. Channel regions with dimensions of L_c = W_c = 10 µm were defined in graphene using photolithography, followed by oxygen-based

reactive ion etching (RIE). Briefly, a positive photoresist S1813 was spin-coated at 4000 rpm for 45 seconds, exposed to a UV light source (~370 nm wavelength, 12 mW cm^{-2} intensity) for 3 seconds using a hard mask and developed in 1:4 solution of water:AZ400K developer. The exposed graphene was removed using RIE conditions: power – O_2 flow rate – 25 sccm, chamber pressure – 60 mTorr, power – 60 W, duration – 30 seconds. The unexposed regions of photoresist were dissolved in acetone resulting in 10 x 10 µm stripes of graphene. Next, source (S) and drain (D) electrodes were patterned using a second photolithography step, followed by deposition of 10/80nm layer of Cr/Au using e-beam evaporation and lift-off. The p-doped Si substrate was used as the back-gate electrode. The native oxide layer on the back of Si was removed by etching in buffered oxide etchant (BOE) and metal contacts were deposited using e-beam evaporation. The device fabrication scheme is shown in Fig. 4.3.

Figure 4.3 Process flow diagram for fabrication of graphene-FETs using photolithography.

4.2.3. GNR fabrication using electron-beam lithography (EBL)

The 10 x 10 µm graphene stripes patterned using photolithography were spin-coated with an electron-beam resist, 2% PMMA in anisole, at 4000 rpm for 45 seconds and baked at 180˚C for 5 minutes. An array of lines with varying line-spacing was written using EBL (Zeiss Leo 1550) using following conditions: voltage = 20 keV, beam current = 70

pA, line dose = 0.2 – 1.0 nC cm^{-1}. Since PMMA is a positive resist, the width of GNR was controlled by varying the spacing between the lines written. The exposed features were developed in a 1:3 solution of MIBK:IPA at 4˚C for 70 seconds (MIBK – methyl isobutyl ketone, IPA – isopropyl alcohol) and the exposed graphene was removed using RIE. The unexposed PMMA was dissolved in acetone at 60˚C and this resulted in GNR arrays with varying widths. A detailed device fabrication scheme is shown in Fig. 4.4.

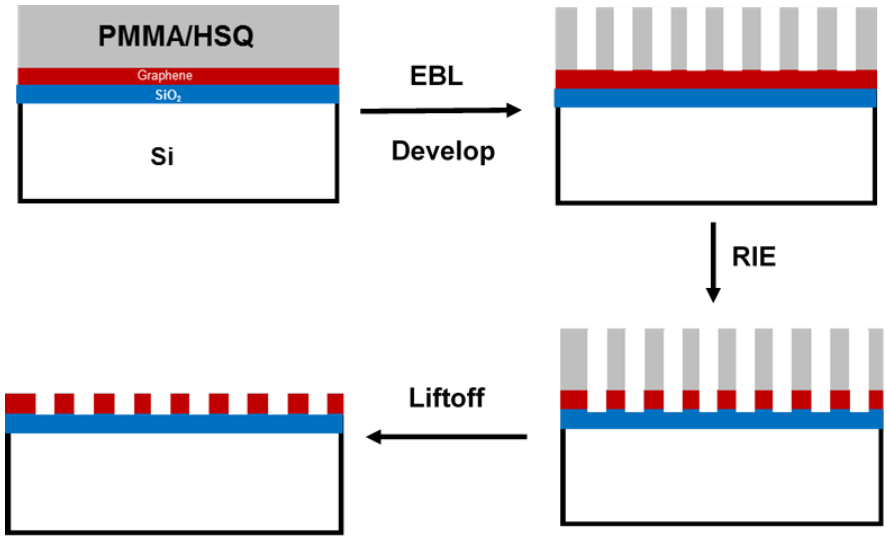

Figure 4.4 Process flow diagram for fabrication of GNR-FETs using electron-beam lithography.

4.2.4. Superlattice nanowire pattern (SNAP) transfer process

SNAP process was originally developed by James Heath group for the fabrication on ultrahigh density Si nanowires.[19,20] We adapted a similar scheme for fabrication of an ultrahigh density array of GNRs. Briefly, a superlattice consisting of alternating layers of GaAs/$Al_{0.8}Ga_{0.2}As$ (varying thickness from 8 − 50 nm) was grown using molecular beam epitaxy (MBE) and cut into small rectangular pieces called 'master' (size − 1x1 mm). The $Al_{0.8}Ga_{0.2}As$ layers were selectively etched in NH_4OH (8 sec) followed by H_2O_2 (5 sec) to

form a comb-like structure with GaAs pillars. A 10 nm layer of Pt was deposited on top of the ridges of the master using e-beam evaporation with samples titled at an angle of 36˚C. The substrate − graphene film on Si/SiO_2 − was spin-coated with a thin layer of heat-curable epoxy at 5000 rpm for 60 seconds. The epoxy formulation consisted of Epoxy bond 110 (*Allied Tech Products*) − 10 drops of part A and 1 drop of part B, added to 20 ml solution of 2% PMMA in anisole. The master with evaporated Pt was dropped vertically on the substrate and baked at 150˚C for 20 minutes to transfer the Pt NWs array from the

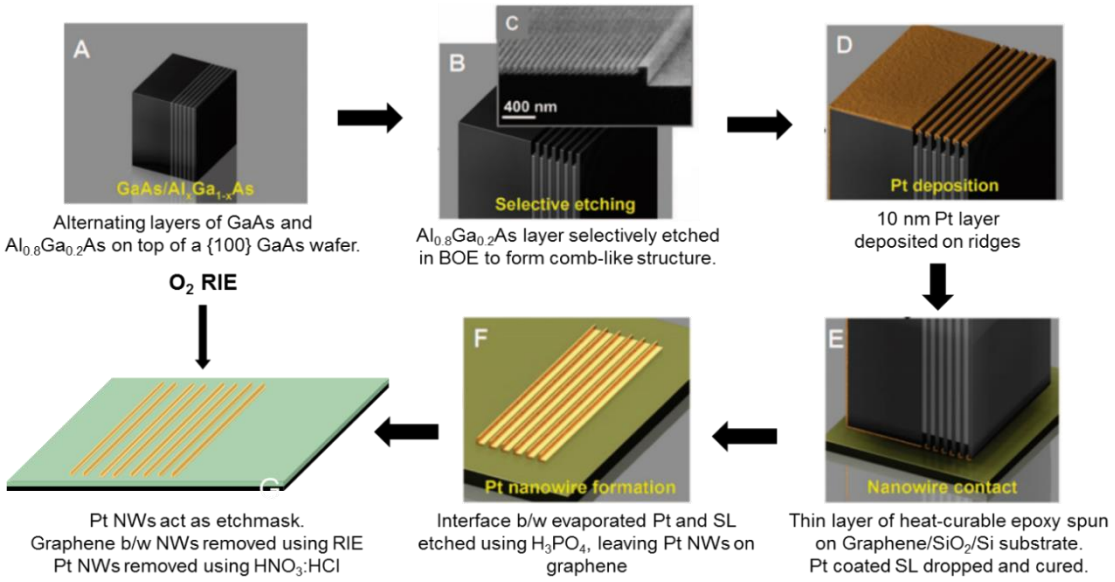

Figure 4.5 Process flow diagram for fabrication of GNR-FETs using superlattice nanowire pattern (SNAP) transfer.

master to the graphene/PMMA layer. The master substrate was removed by etching the interface in a solution of 5:1:50 H_3PO_4:H_2O_2:H_2O for 6 hours. This results in an ultrahigh density Pt NW array on graphene/PMMA which serves as an etch mask. The unprotected graphene/PMMA between the Pt NWs is removed using RIE at 100 W for 2 minutes. In

the final step, the Pt NWs are lifted off by dissolving the PMMA layer in acetone. A detailed device fabrication scheme is shown in Fig. 4.5.

4.3. Results and Discussion

4.3.1. Electrical characteristics: Large area graphene-FET

The electrical properties of CVD grown large-area SLG were investigated by fabricating FET devices. The channel resistance of graphene-FETs with a channel length of 10 µm was measured by obtaining characteristic curves ($I_d - V_{ds}$) with V_{ds} between +0.1V and −0.1V (Fig. 4.6(a)) using a Keithley source-meter. No back-gate voltage (V_g) was applied during these measurements. The transfer characteristics ($I_d - V_g$) were measured using the highly p-doped Si substrate as the global back gate, and 300 nm thermally grown SiO_2 layer as the gate dielectric. Fig. 4.6(b) shows the $I_d - V_g$ curve for V_g varying between −10V and +50V and V_{ds} = 0.1V. The transfer curve shows the characteristic ambipolar nature of graphene with V_{cnp} (charge neutrality point) around +15V. This shift of V_{cnp} to positive V_g (V_{cnp} = 0 V in pristine undoped graphene) is indicative of p-type nature typically seen in CVD graphene due to hole-doping induced during the O_2 plasma step used for patterning for the graphene channel. Hole-doping can also be attributed to adsorption of atmospheric oxygen and vapors as the channel is exposed to ambient air.[21] The electron and hole mobilities were calculated using the equation:[3]

$$\mu = \frac{L_c g_m}{W_c C_g V_{ds}}$$

where, L_c is the channel length (10 µm), g_m is the transconductance (slope of the $I_d - V_g$ curve, $\frac{dI_d}{dV_g}$), W_c is the channel width (10 µm), C_g is the gate capacitance per unit area (11.6

nF cm^{-2} for 300 nm SiO_2) and V_{ds} is the source-drain bias (0.1 V). The mobility values were found to be in-line with literature reported values for back-gated graphene FETs with

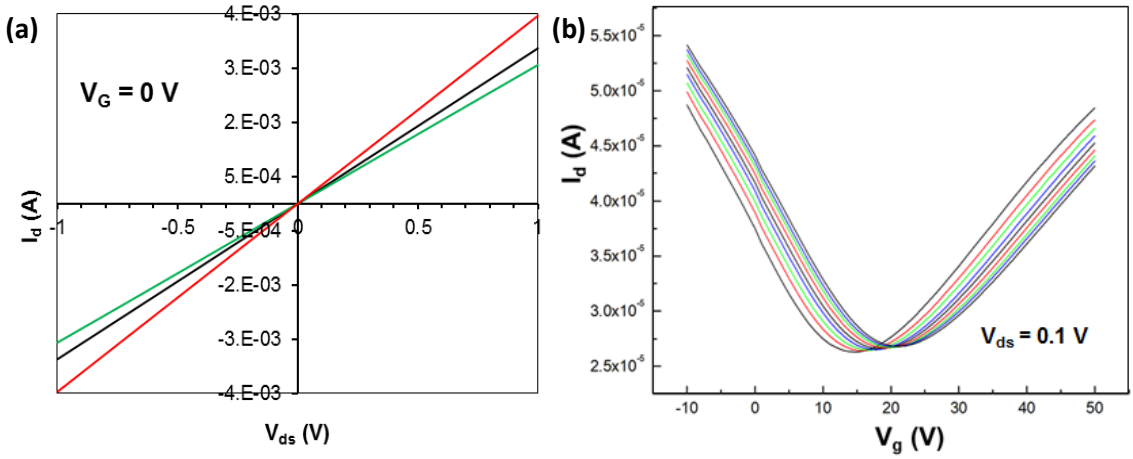

Figure 4.6 (a) $I_d - V_{ds}$ curve for three independent large area graphene devices (L_c = 10 µm); **(b)** Transfer characteristics ($I_d - V_g$) for multiple large area graphene FETs.

mobility of ~2000 cm^2/Vs. However, due to absence of bandgap in large area graphene, the I_{ON}/I_{OFF} is negligible (~2) and the off-current is as high as ~2.5 x 10^{-5} A.

4.3.2. Electrical characteristics: GNR-FETs fabricated using e-beam lithography

Graphene nanoribbons (GNR) arrays were fabricated by patterning the large area graphene used in the FET devices discussed above using electron-beam lithography. The graphene was first spin-coated with a thin layer (~80-100 nm) of positive e-beam resist, PMMA. Next, the PMMA coated graphene was exposed to an electron beam with accelerating voltage = 20 keV and an array of line features was patterned. The electron dose was varied between 0.2 − 2.0 nC cm^{-1} to obtain GNR of different widths. Since PMMA is a positive resist, the regions exposed to electron beam were dissolved during developing stage. Correspondingly, the width of GNRs was inversely proportional to the electron line-dose and directly proportional to the spacing between the line features. After

exposure, the devices were developed in MIBK:IPA solution held at 4˚C to ensure slow dissolution rate of the exposed PMMA regions. The development at low temperature is critical for obtaining the required high resolution and reproducible sub-micron features. In the final step, the exposed graphene regions were removed using O_2-based RIE and the PMMA layer was dissolved in acetone to obtain GNR arrays. Fig. 4.7 shows the SEM images of GNR arrays with widths between 60 nm (line dose = 0.6 nC cm^{-1}) and 100 nm (line dose = 0.2 nC cm^{-1}).

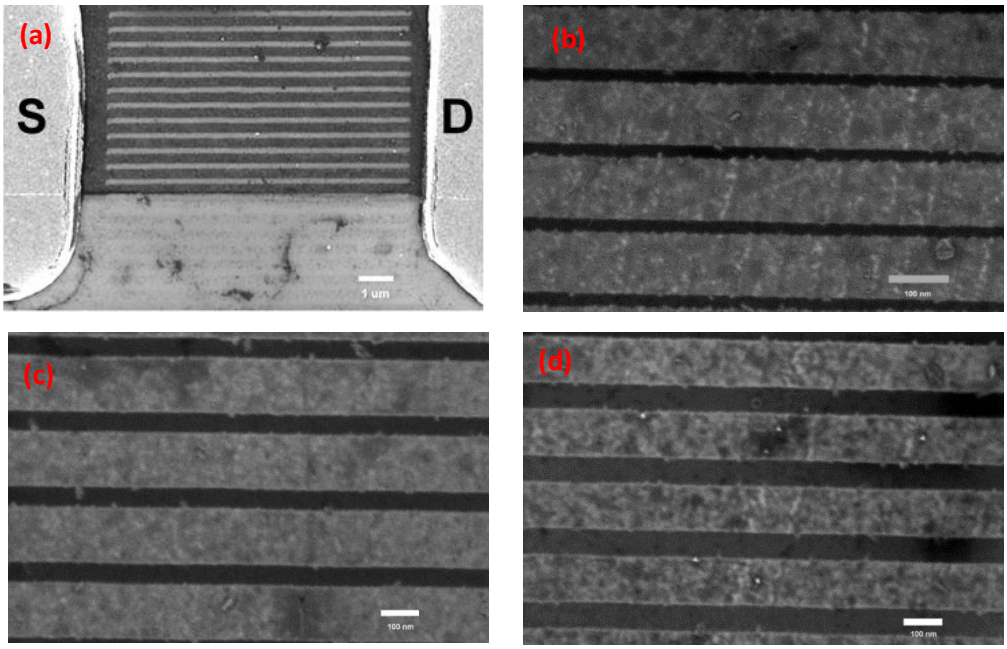

Figure 4.7 (a) SEM image of a GNR-FET device fabrication using e-beam lithography. SEM images of GNR arrays fabricated by changing the electron line dose: **(b)** Line dose=0.2 nC cm^{-1}, width – 100 nm, **(c)** Line dose=0.4 nC cm^{-1}, width – 80 nm, **(d)** Line dose=0.6 nC cm^{-1}, width – 60 nm. The scale bar (b), (c), (d) is 100 nm.

The electrical characteristics of the GNR-FET devices were measured by obtaining transfer curves as in case in large area graphene FETs. As shown in Fig. 4.8, the transfer curve for GNR array of 60 nm width showed a shift in V_{cnp} to +85V as compared to +15V

for large area graphene. This shift in V_{cnp} to higher positive voltages is attributed to p-doping induced during the RIE step of GNR fabrication process. The RIE introduces

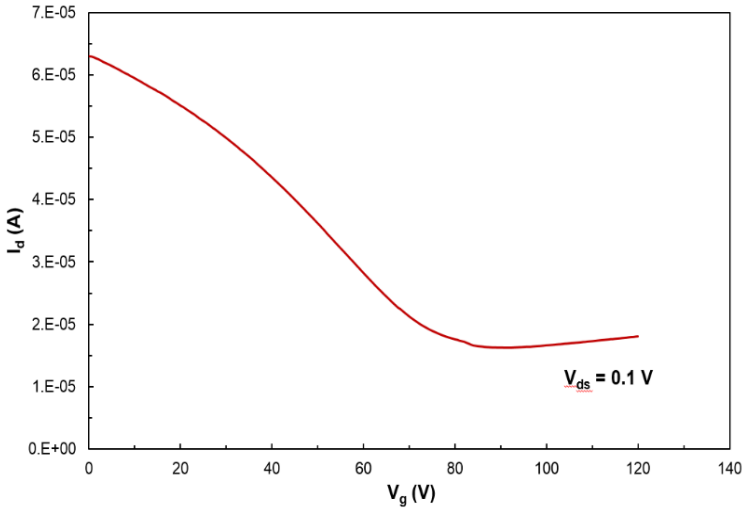

Figure 4.8 Transfer characteristics ($I_d - V_g$) for GNR-FET with ribbon width of 60 nm.

defects in the form of oxygen-functional groups at the edge carbon atoms of GNRs, which results in p-doping due to the electro-negative nature of these groups.[21,22] These edge defects further lead to decrease in the mobility of GNR device to ~500 cm^2/Vs as compared to large area graphene. This decrease in mobility is characteristic nature of GNR fabricated using a top-down approach. Additionally, there was a small increase in I_{ON}/I_{OFF} ratio (~4) and the current in the off-state decreased slightly to ~1 x 10^{-5} A. This I_{ON}/I_{OFF} ratio is directly related to the extent of bandgap induced due to the quantum confinement of carriers in on-dimensional ribbons. Engineering a sizable bandgap (≥300 meV) requires patterning of GNRs widths 20 nm and lesser. Thus, the low I_{ON}/I_{OFF} ratios observed can be attributed to the resolution limit of the EBL tool. Since the width of EBL fabricated GNR (60−200 nm) is not narrow enough to engineer a sizable bandgap, a second top-down fabrication

technique using a superlattice nanowire pattern (SNAP) transfer process was employed to pattern GNRs with widths down to sub-10 nm.

4.3.3. GNR fabrication using SNAP process

The superlattice wafer with alternating layers of GaAs/$Al_{0.8}Ga_{0.2}As$ was cut into small pieces and the $Al_{0.8}Ga_{0.2}As$ layers were selectively etched in NH_4OH. Fig. 4.9(a) shows the SEM image of comb-like structures with GaAs pillars. For an etch time of 8 seconds, the ridge height was found to be ~30 nm. Longer etch times lead to deeper trenches and this increases the possibility of collapsing. Angled deposition was employed to deposit Pt on top of the ridge and this results in an 'L' shaped cross-section of the Pt layer. SEM image shown in Fig. 4.9(b) confirms the successful deposition of Pt on top of the GaAs ridges.

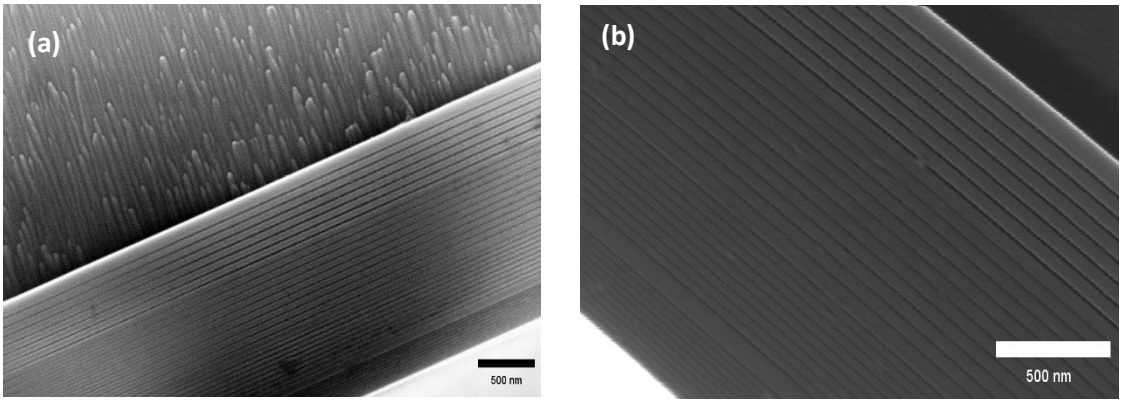

Figure 4.9 (a) SEM image (top view) of master with comb-like features formed due to selective etching of $Al_{0.8}Ga_{0.2}As$ layers; **(b)** SEM image (top view) of master after angled deposition of 10 nm Pt layer on top of GaAs ridges.

Next, a thin layer of heat-curable epoxy was spin-coated on the graphene film of Si/SiO_2. The thickness of epoxy is critical for successful bonding of the superlattice piece and it was optimized by diluting the PMMA solution using anisole solvent. The superlattice

piece with deposited Pt layer was bonding to the substrate by dropping it vertically with the atomically flat plane facing down. It is critical to drop the superlattice vertically to ensure transfer of the Pt NWs to the substrate. The reproducibility and yield was found to be very low when dropping the superlattice manually using a tweezer. To overcome this issue, a customized micro-manipulator (Fig. 4.10) was used to ensure precise vertical dropping of the superlattice. The master was bonded firmly to the graphene/PMMA

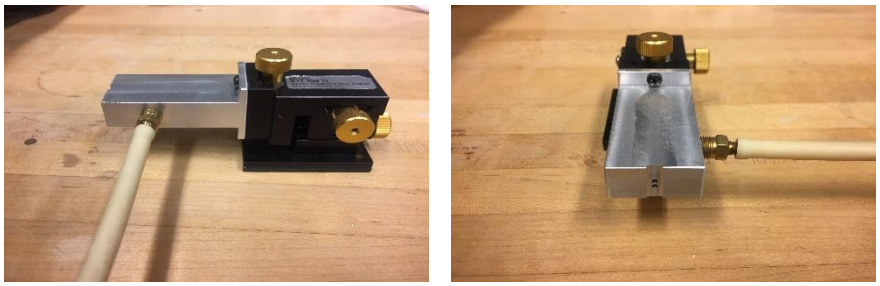

Figure 4.10 (a) Side-view and **(b)** Front-view of the customized micromanipulator used for vertical dropping of master.

substrate after curing of the epoxy layer. Next, the master was etched in phosphoric acid solution that etches both, GaAs and $Al_{0.8}Ga_{0.2}As$, layers and thus releases the superlattice template from the Pt NWs. In an ideal case scenario, this would lead to transfer of Pt NW array on graphene/PMMA and act like an etch mask for anisotropic etching of graphene between the Pt NWs. However, presently there were issues with the transfer process and the Pt NWs were not successfully transferred. To our understanding, this issue could be due to improper cleaning/surface roughness of the substrate and/or higher thickness of the epoxy layer that causes the PMMA to fill the ridges of the master and thereby prevent it from bonding successfully. Optimization of this step in future work would require

modifying the epoxy layer formulation to get a consist and uniformly thin layer (~10 nm) of epoxy.

4.3.4. Characterization of edge defects

Most top-down GNR fabrication processes involve an anisotropic etching step using O_2–based RIE to remove the graphene layer by using an etch mask (PMMA in case of EBL, Pt NWs in case of SNAP). As discussed in Section 4.3.2, this etching step inevitably introduces defects such as oxygen-functional groups and terminal sp^3-hybridized carbon atoms. A schematic representation of these edge-site defects is shown in Fig. 4.11. Additionally, unlike the GNRs formed by unzipping of carbon nanotubes, the edge carbon atoms do not have a prefer crystal orientation (armchair/zigzag) and consist of a combination of both crystal orientations. Such defects are responsible for the significant reduction in carrier mobility and p-doping of GNRs as compared to pristine graphene. We characterized the nature of these defects using Raman spectroscopy and x-ray photoelectron spectroscopy (XPS) analysis. In these spectroscopic characterization techniques, the lateral resolution (~1 µm in case of Raman spectroscopy and ~25 µm in case of XPS) is limited by the spot-size of the probe beam. To ensure the response is obtained purely from edge-atoms and not the basal plane, large area

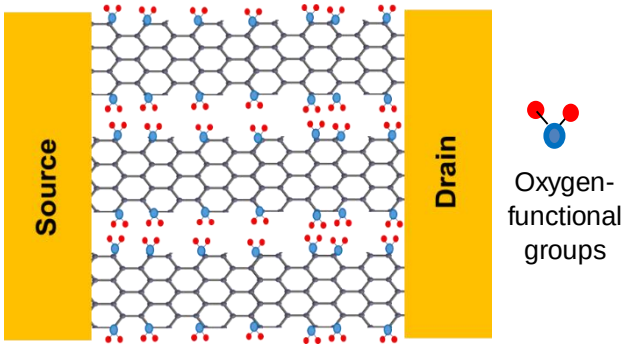

Figure 4.11 Schematic representation of edge defects in graphene nanoribbons introduced during RIE.

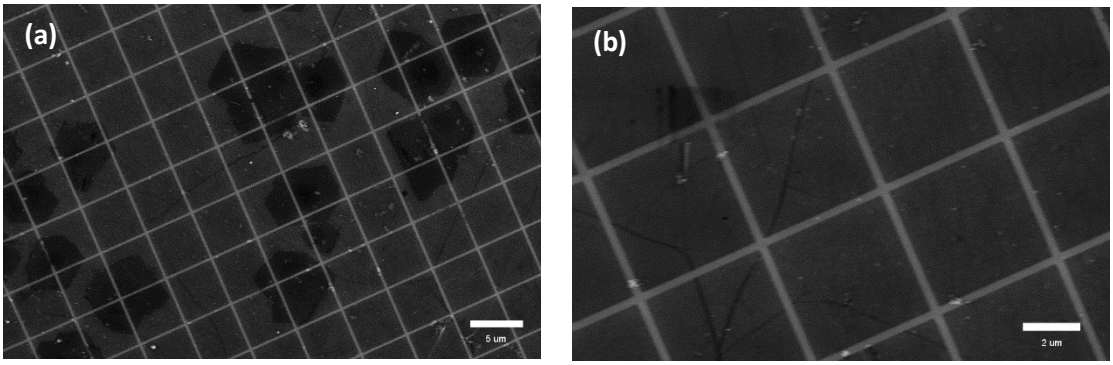

Figure 4.12 SEM images at **(a)** low magnification, **(b)** high magnification of micro-patterned graphene fabricated using EBL for spectroscopic characterization of defects. The scale bar in (a) is 5µm and (b) is 2 µm.

graphene was patterned into 4 x 4 µm squares using EBL. Fig. 4.12 shows the SEM images of the micro-patterned graphene sample used for spectroscopic characterization.

The Raman spectra obtained from the central part of the ribbon (Fig. 4.13(a)) showed a negligible D-peak intensity, similar to large area graphene and this is indicative of the pristine nature of basal-plane graphene. However, the Raman spectra obtained at the edge planes showed a significant increase in the intensity of D peak (Fig. 4.13(b)), with I_D/I_G increasing from 0.08 to 0.94.

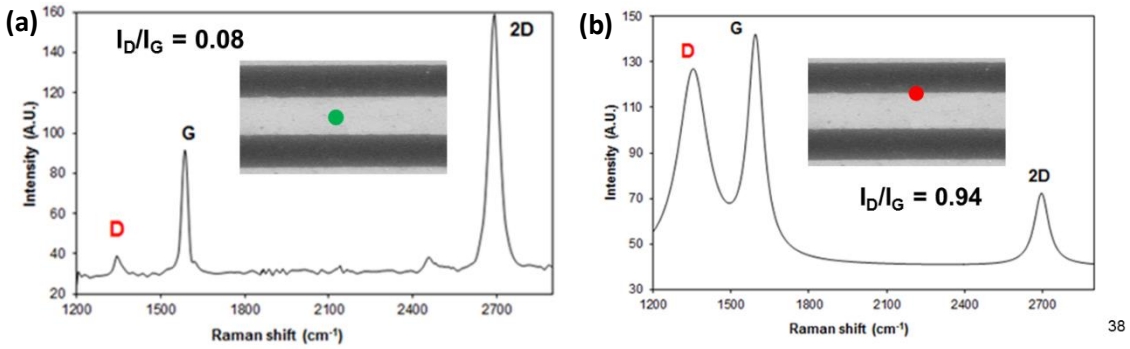

Figure 4.13 Raman spectra obtained near **(a)** Central region of micro-patterned graphene showing I_D/I_G = 0.08, (b) Edge region of micro-patterned graphene showing I_D/I_G = 0.94. The inset SEM images indicate the location where spectra were recorded.

To further confirm the nature and type of these defects, elemental analysis using XPS was employed. The XPS spectrum of large area pristine graphene (Fig. 4.14(a)) showed a pronounced asymmetry on the higher binding energy side typical of poly-aromatic carbons. The asymmetric C1s core peak is indicative of graphitic structure as opposed to aliphatic or sp^3 based carbon materials which exhibit symmetric spectra.[23,24] The spectrum was fitted with a main peak (284.2 eV) corresponding to C=C and a secondary peak (285.3 eV), which corresponds to sp^3 hybridized carbon bonds due to amorphous carbon contaminants and defects. The relatively small intensity of this peak indicates marginal traces of other carbon functionalities, which is characteristic of CVD synthesized graphene.[24] However, the XPS spectra of micro-patterned graphene (Fig. 4.14(b)) showed a much larger concentration of sp^3 defects, carbonyl (C=O) and ether

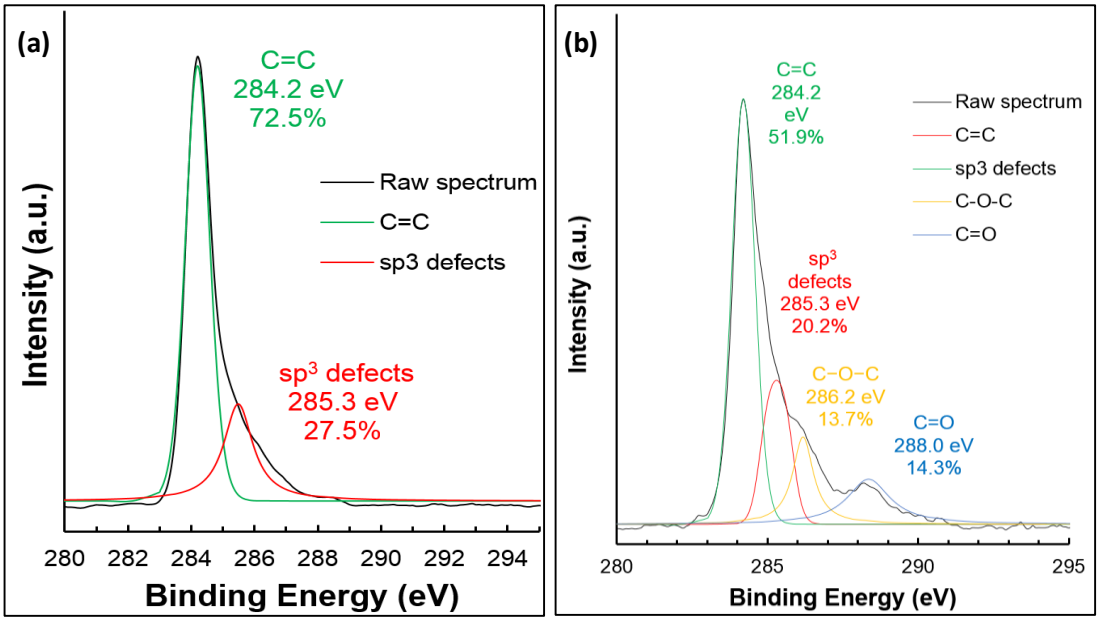

Figure 4.14 XPS analysis of **(a)** large area graphene with sp^3 defects due to grain boundaries but absence of oxygen-functional groups **(b)** micro-patterned graphene showing a significant increase in concentration of oxygen-functional groups due to edge defects.

(C−O−C) groups. The C1s core peak was deconvoluted and the relative concentration of these defects and carbon functionalities was measured.

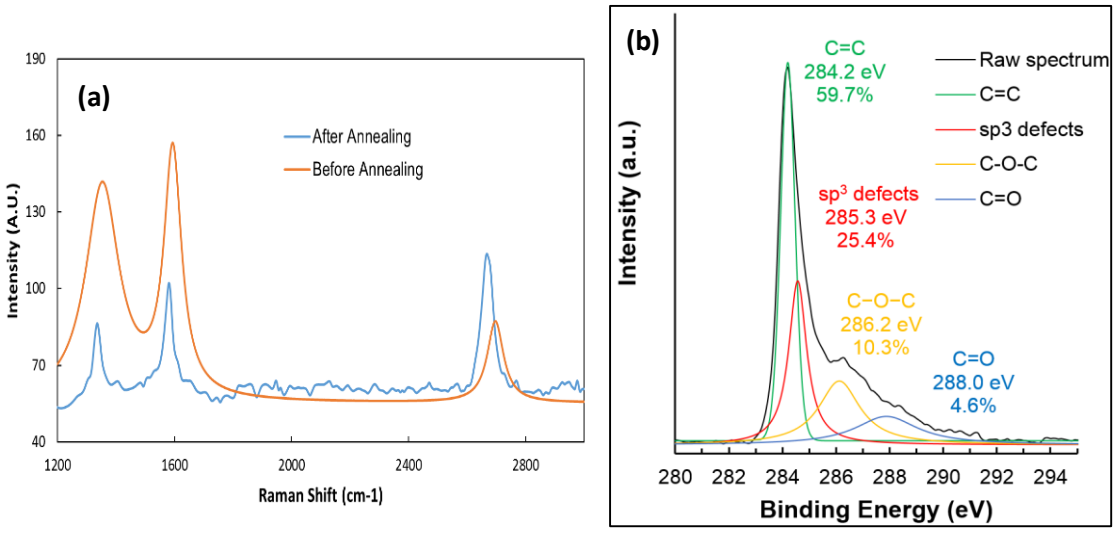

Figure 4.15 (a) Raman spectra micro-patterned graphene showing reduction in I_D/I_G from 0.94 to 0.78 after thermal annealing; **(b)** XPS analysis showing reducing in concentration of oxygen-functional groups.

The spectroscopic characterization experiments give us some knowledge about the concentration and nature of defects introduced during the device fabrication process. Analogous to graphene oxide, most of these defects are due to oxidation of carbon atoms in graphene lattice. We explored different treatments including chemical reduction using hydrazine,[25] electrochemical reduction[26] and thermal annealing in reducing environment at high temperatures[27] to reduce the concentration of defects and restore the graphitic structure to increase the mobility of GNR-FET devices. The results shown in Fig. 4.15 demonstrated that thermal annealing at 300˚C under low pressure (1.3 Torr) with 5% H_2 in Ar led to a decrease in the intensity of D peak in Raman spectra. The I_D/I_G ratio decreased from 0.94 in case of as-prepared micro-patterned graphene, to 0.78 after thermal annealing.

Additionally, XPS showed a lowered concentration of carbon functionalities including carbonyl and ether groups due to reduction of oxygen. The relative percentage of sp^2 hybridized C=C increased from 52% to almost 60% after thermal annealing.

4.3.5. GNR-FET based gas sensors

One of the commonly discussed applications of graphene-FET devices is electrical sensors for detection of chemicals and biological species. We evaluated the performance of the GNR-FET devices for sensing of NO_2 by measuring the change in channel resistance upon exposure of to varying concentration of NO_2. As shown in Fig. 4.16, chronoamperometric measurements were performed keeping V_{ds} = 0.1 V and V_g = 0 V, and monitoring I_d as a function of time. Due to p-type nature of GNRs and electron withdrawing nature of NO_2, exposure to 2.5 ppm of NO_2 in N_2 led to ~2% decrease in channel resistance. In comparison, the graphene-FET device (shown in inset) did not show any measurable change in resistance. This result demonstrates that, unlike most applications of FETs, graphene chemical sensors benefit from the presence of edge-defect sites. The negligible

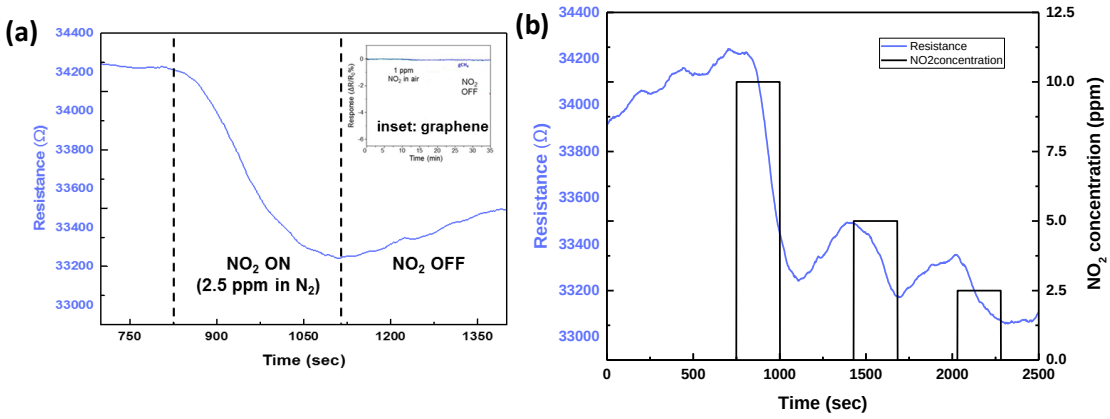

Figure 4.16 (a) Dynamic response of GNR-FET device upon exposure to 2.5 ppm NO_2 in N_2; **(b)** Dynamic response of GNR-FET device for NO_2 concentrations between 2.5 and 10 ppm.

response in case of graphene-FET is due to the inertness of pristine graphene, which limits the sensitivity due to lack of binding sites for analyte molecules. This result demonstrates the application of GNRs as an attractive option for fabrication of FET-based chemical sensors with significantly higher sensitivity compared to their graphene counterparts.

4.4. Conclusions

In conclusion, this work discusses bandgap engineering of graphene by quantum confinement of charge carriers into a pseudo one-dimensional nanostructures called graphene nanoribbons (GNR). The GNR-FET devices were fabricated using two different top-down techniques: (a) Conventional electron-beam lithography for patterning GNR with widths from 50-200 nm, and (b) Superlattice nanowire pattern (SNAP) transfer process for patterning GNR with widths from 8-20 nm. Since FET-based applications require nanopatterning of graphene down to sub-10 nm, the I_{ON}/I_{OFF} ratio of the GNR-FET with ribbon width of 50 nm fabricated using e-beam lithography was found to be low (~4). A new method based on fabrication of ultrahigh density Pt NW array with widths down to 8 nm was developed. The fabricated Pt NW array acts like an etch mask and facilitates fabrication of GNRs with narrow widths. The preliminary attempts, though promising, were not successful and require optimization of device fabrication steps. The edge defects in GNRs, which are responsible for degradation of carrier mobility and increase in off-state current were characterized using Raman spectroscopy and x-ray photoelectron spectroscopy. Thermal annealing treatment was used to reduce the concentration of these defects. Finally, the fabricated GNR-FET device was used as a gas sensor for dynamic sensing of NO_2 gas. Compared to the pristine graphene-FET, the GNR-FET showed a

significant increase in sensitivity and were able to detect low concentrations (2.5 ppm) of NO_2.

4.5. References

1. Veeraraghavan, S. U. R. Y. A., and Jerry G. Fossum. "Short-channel effects in SOI MOSFETs." *IEEE Transactions on Electron Devices* 36, no. 3 (1989): 522-528.
2. Suzuki, Eiichi, Kenichi Ishii, Seigo Kanemaru, Tatsuro Maeda, Toshiyuki Tsutsumi, Toshihiro Sekigawa, Kiyoko Nagai, and Hiroshi Hiroshima. "Highly suppressed short-channel effects in ultrathin SOI n-MOSFETs." *IEEE Transactions on Electron Devices* 47, no. 2 (2000): 354-359.
3. Schwierz, Frank. "Graphene transistors." *Nature nanotechnology* 5, no. 7 (2010): 487-496.
4. Radisavljevic, Branimir, Aleksandra Radenovic, Jacopo Brivio, I. V. Giacometti, and A. Kis. "Single-layer MoS_2 transistors." *Nature nanotechnology* 6, no. 3 (2011): 147-150.
5. ITRS, International Technology Working Groups International Technology Roadmap for Semiconductors (ITRS, 2010)
6. Novoselov, Kostya S., Andre K. Geim, Sergei V. Morozov, D. Jiang, Y_ Zhang, Sergey V. Dubonos, Irina V. Grigorieva, and Alexandr A. Firsov. "Electric field effect in atomically thin carbon films." *science* 306, no. 5696 (2004): 666-669.
7. E. Guerriero, L. Polloni, M. Bianchi, A. Behnam, E. Carrion, L. G. Rizzi, E. Pop, and R. Sordan, "Gigahertz integrated graphene ring oscillators," ACS Nano, vol. 7, no. 6, pp. 5588-5594, 2013.

8. C.-H. Jan, U. Bhattacharya, R. Brain, S.-J. Choi, G. Curello, G. Gupta, W. Hafez, M. Jang, M. Kang, K. Komeyli, T. Leo, N. Nidhi, L. Pan, J. Park, K. Phoa, A. Rahman, C. Staus, H. Tashiro, C. Tsai, P. Vandervoorn, L. Yang, J.-Y. Yeh, and P. Bai, "A 22nm SoC platform technology featuring 3-D tri-gate and high-k/metal gate, optimized for ultra-low power, high performance and high density soc applications," in Proceedings of the IEEE International Electron Devices Meeting (IEDM), San Francisco, USA, 2012, pp. 3.1.1-3.1.4.
9. Schwierz, Frank. "Graphene transistors: status, prospects, and problems." *Proceedings of the IEEE* 101, no. 7 (2013): 1567-1584.
10. Han, Melinda Y., Barbaros Özyilmaz, Yuanbo Zhang, and Philip Kim. "Energy band-gap engineering of graphene nanoribbons." Physical review letters 98, no. 20 (2007): 206805.
11. Li, Xiaolin, Xinran Wang, Li Zhang, Sangwon Lee, and Hongjie Dai. "Chemically derived, ultrasmooth graphene nanoribbon semiconductors." Science 319, no. 5867 (2008): 1229-1232.
12. Zhang, Yuanbo, Tsung-Ta Tang, Caglar Girit, Zhao Hao, Michael C. Martin, Alex Zettl, Michael F. Crommie, Y. Ron Shen, and Feng Wang. "Direct observation of a widely tunable bandgap in bilayer graphene." Nature 459, no. 7248 (2009): 820-823.
13. Liu, Hongtao, Yunqi Liu, and Daoben Zhu. "Chemical doping of graphene." Journal of materials chemistry 21, no. 10 (2011): 3335-3345.

14. Wilder, Jeroen WG, Liesbeth C. Venema, Andrew G. Rinzler, Richard E. Smalley, and Cees Dekker. "Electronic structure of atomically resolved carbon nanotubes." *Nature* 391, no. 6662 (1998): 59-62.
15. Marmolejo-Tejada, Juan M., and Jaime Velasco-Medina. "Review on graphene nanoribbon devices for logic applications." *Microelectronics Journal*48 (2016): 18-38.
16. Celis, A., M. N. Nair, A. Taleb-Ibrahimi, E. H. Conrad, C. Berger, W. A. de Heer, and A. Tejeda. "Graphene nanoribbons: fabrication, properties and devices." *Journal of Physics D: Applied Physics* 49, no. 14 (2016): 143001.
17. Hwang, Wan Sik, Kristof Tahy, Xuesong Li, Huili Grace Xing, Alan C. Seabaugh, Chun Yung Sung, and Debdeep Jena. "Transport properties of graphene nanoribbon transistors on chemical-vapor-deposition grown wafer-scale graphene." *Applied Physics Letters* 100, no. 20 (2012): 203107.
18. Huang, Chi-Hsien, Ching-Yuan Su, Takeru Okada, Lain-Jong Li, Kuan-I. Ho, Pei-Wen Li, Inn-Hao Chen, Chien Chou, Chao-Sung Lai, and Seiji Samukawa. "Ultra-low-edge-defect graphene nanoribbons patterned by neutral beam." *Carbon* 61 (2013): 229-235.
19. Melosh, Nicholas A., Akram Boukai, Frederic Diana, Brian Gerardot, Antonio Badolato, Pierre M. Petroff, and James R. Heath. "Ultrahigh-density nanowire lattices and circuits." *Science* 300, no. 5616 (2003): 112-115.
20. Heath, James R. "Superlattice nanowire pattern transfer (SNAP)." *Accounts of chemical research* 41, no. 12 (2008): 1609-1617.
21. Liu, Hongtao, Yunqi Liu, and Daoben Zhu. "Chemical doping of graphene." *Journal of materials chemistry* 21, no. 10 (2011): 3335-3345.

22. Paul, Rajat Kanti, Sushmee Badhulika, Nuvia M. Saucedo, and Ashok Mulchandani. "Graphene nanomesh as highly sensitive chemiresistor gas sensor." *Analytical chemistry* 84, no. 19 (2012): 8171-8178.

23. Darmstadt, Hans, and Christian Roy. "Surface spectroscopic study of basic sites on carbon blacks." Carbon 41, no. 13 (2003): 2662-2665.

24. Peltekis, Nikolaos, Shishir Kumar, Niall McEvoy, Kangho Lee, Anne Weidlich, and Georg S. Duesberg. "The effect of downstream plasma treatments on graphene surfaces." Carbon 50, no. 2 (2012): 395-403.

25. Park, Sungjin, Jinho An, Jeffrey R. Potts, Aruna Velamakanni, Shanthi Murali, and Rodney S. Ruoff. "Hydrazine-reduction of graphite-and graphene oxide." Carbon 49, no. 9 (2011): 3019-3023.

26. Shao, Yuyan, Jun Wang, Mark Engelhard, Chongmin Wang, and Yuehe Lin. "Facile and controllable electrochemical reduction of graphene oxide and its applications." Journal of Materials Chemistry 20, no. 4 (2010): 743-748.

27. Gao, Xingfa, Joonkyung Jang, and Shigeru Nagase. "Hydrazine and thermal reduction of graphene oxide: reaction mechanisms, product structures, and reaction design." The Journal of Physical Chemistry C 114, no. 2 (2009): 832-842.

CHAPTER 5

Applications of Carbon Nanotubes as FET/chemiresistive based electrical biosensors

5.1. Introduction

Due to the absence of a sizable bandgap in graphene and the limitations of the different synthesis methods of graphene nanoribbons, it is unlikely that high-performance integrated logic circuits with graphene as a channel material will be practical within the next decade. However, more recently other electronic applications of graphene, which do not necessarily require the highest quality material, are being explored.[1] Some of these applications include flexible electronics such as touch screen displays,[2] organic light-emitting diodes (OLEDs),[3] photovoltaics where graphene can be used a transparent electrode,[4] energy storage and conversion devices such as supercapacitors[5] and dye-sensitized solar cells,[6] and electrical sensors.[7-10] In particular, the use of carbon based nanomaterials such as graphene and carbon nanotubes for developing chemical sensors has been extensively explored in the recent years. Sensors are used for a wide range of applications including environmental monitoring of toxins and pollutants,[9] surveillance and security,[11] lab-on-a-chip devices,[12] healthcare including point-of-care diagnostics[13,14] and so on. This has led to increasing research interest in exploring new materials that can be used for fabrication of cheaper and compact sensor devices with low power consumption.

The geometry of carbon nanomaterials, 2-D (planar) in case of graphene and 1-D (tubular) for CNTs, and their intriguing physiochemical and electrical properties makes them ideal transduction materials for development of next generation miniaturized biosensors. The planar and tubular geometry ensures exposure of almost all the surface atoms which enables binding a significant fraction of analyte molecules to the transduction material. The Debye length, k_D, a measure of the field penetration into the bulk, is comparable to the dimensions of these nanostructures, which causes significant modulation of their electronic properties upon exposure to chemicals.[9,15] These properties enable label-free detection of analytes with higher sensitivities and lower limits of detection. Furthermore, they can easily be configured as field-effect transistors using lithography techniques and integrated with the modern microelectronics for fabrication of multiplexed devices that can detect a number of analytes simultaneously. Additionally, their electrochemical properties such as faster electron transfer kinetics, low residual current, wide potential window and ease of surface functionalization makes ideal for biosensing applications. Unlike most graphene applications that require a reduction of surface defects, graphene chemical sensors benefit from the presence of defect sites. The inertness of pristine graphene limits the sensitivity by inhibiting the chemical binding of analytes. It has been experimentally demonstrated that the electrochemistry of graphene is driven by the edge-plane sites that can exhibit an electron transfer rate (k_e) as high as 0.01 cm/s.[16] So, the high density of edge-plane defect sites per unit mass of the material in carbon nanotubes and chemically modified graphene enhances their electrochemical activity,[17] making them highly sensitive and selective transduction materials in comparison to other nanomaterials

such as metal oxide nanowires and conducting polymer films. For the detection of analytes from complex matrices, the transducer element of the biosensor, i.e. graphene or CNT is coupled with a biorecognition molecule, i.e. enzymes, antibodies, aptamers, etc., for enhancing the biosensor selectivity and achieving high sensitivities without using labeling or amplification techniques (Fig. 5.1).[9]

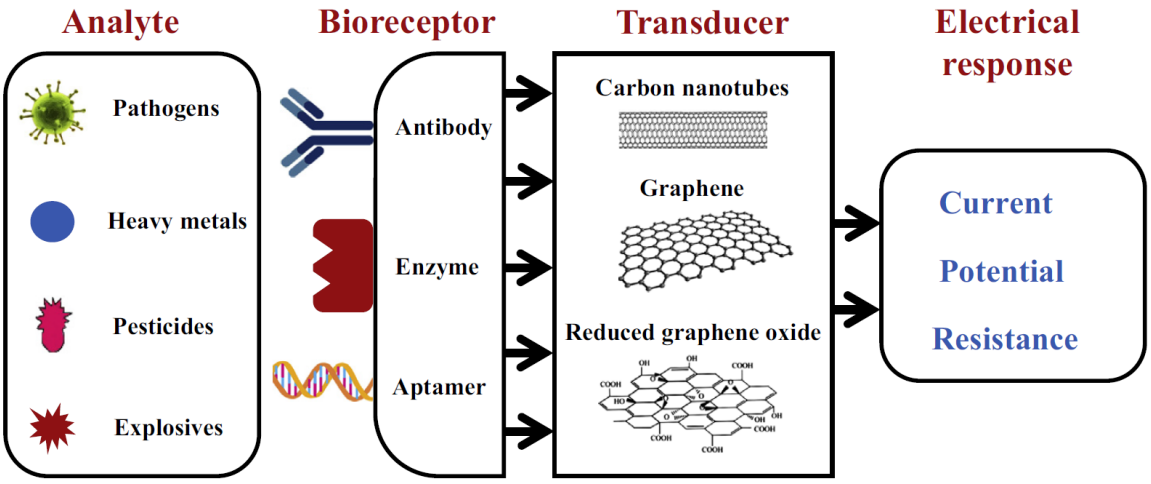

Figure 5.1 Carbon nanomaterial based electrical biosensors

In this chapter, I discuss the fabrication of chemiresistive/field-effect transistor (FET)-type biosensors using carbon nanotubes. Unlike the conventional metal-oxide semiconductor field-effect transistors (MOSFETs), where the conducting channel is buried in the bulk material, the nanotubes or graphene are located on the surface of the supporting substrate in direct contact with the environment. Upon incubation and specific binding of chemical/biological analytes, the conductance changes and the change is used to quantify the analyte concentration. The first work discusses fabrication of a carbon nanotube biosensor for electronic detection of microRNAs, which are potential biomarkers for early-stage diagnosis of cancer.[18] The second work explores the use of carbon nanotube biosensor for detection of mercury, a toxic metal pollutant, in saliva samples.[19]

5.2. Electronic Detection of MicroRNA at Attomolar Level with High Specificity

5.2.1. Introduction

Since their discovery two decades ago, microRNAs (miRNAs) have emerged as a new modality in medical diagnostics. These small endogenous biomolecules of ~22 nucleotides in length have been linked to virtually all known physiological and pathological processes, such as cell differentiation and proliferation, developmental timing, neuronal asymmetry, apoptosis, insulin secretion, and various metabolic reactions.[20,21] In addition, the change of miRNA levels in many human diseases suggests that miRNA expression profiling could be used for defining clinical phenotypes, as well as potentially useful molecular diagnostic markers. However, accurately measuring miRNA levels has also posed numerous new challenges to the analytical technologies. Given the short length of the miRNAs with inherently different melting temperatures, their trace levels in the cell (typically <1% relative to the other cellular RNAs), and the highly similar sequences between miRNA family members,[21] the detection methods need to be extremely sensitive. In addition, they need to be specific to accurately measure the levels of specific analytes in small amounts of complex RNA sample. At the present time, the majority of the microRNA detection relies on techniques like Northern blot[22-24] and reverse transcriptase-polymerase chain reaction (RT-PCR).[25] These methods are time-consuming, have low throughput, require a relatively large amount of RNA material. In additions, these techniques require the use of an equipped laboratory with specialized and well-trained biologists and are not feasible for routine serum-based miRNA determination.

To enable detection of the extremely low concentration over a wide dynamic range in which miRNA is present in cells (<1% of total cell RNAs) and human serum (0 to 1 pM), we have integrated a highly selective biorecognition element, the RNA binding protein p19 from Carnation Italian ringspot virus (CIRV), with an extremely sensitive carbon nanotubes field effect transistor (CNTs-FET) transducer for a label-free, fast, facile, and low cost nanobiosensor. This is the first report of a biosensor using p19 and CNTs-FET combination for electronic detection of miRNA. The p19 is a 19 kDa protein expressed by plant viruses to function as a suppressor of the RNA silencing pathway and binds with high affinity only to double stranded/duplex RNA (dsRNA) in a size-specific and sequence-independent manner; i.e., it does not bind ssRNA, tRNA, rRNA, ssDNA, or dsDNA.[26,27] The p19 binding affinity is determined by the miRNA duplex region length. For example, it has the highest affinity for 21−23 nt dsRNA which progressively becomes weaker for 24−26 nt dsRNA and very low for 19 nt and smaller. Hybridization of a miRNA-specific probe to a single-stranded target miRNA creates dsRNA that tightly binds the p19 fusion protein. Binding of the dsRNA to the protein results in a change in conductance of the CNTs, and the amount of target miRNA in the sample is quantified by measuring the change in resistance from the I−V curve (Figure 1). miRNA-122a, a specific liver marker expressed in 70% of liver cells,[28] which has been linked with lipid metabolism, liver homeostasis,[29,30] and hepatitis C virus replication,[31] was studied as a model target. This nanobiosensor detected the target miRNA-122a from 1 aM to 10 fM in the presence of a million-fold excess of total RNA and other miRNA sequences. The 1 aM limit of detection is the best reported to date.

5.2.2. Experimental Details

(a) Fabrication of CNT networks FET device: Sensors were microfabricated on a highly doped p-type silicon substrate capped with 300 nm of SiO_2 (*Ultrasil Corp.*, 4″ Prime Silicon Wafer, P/Boron doped, <100> orientated, 525±25 µm thick, 0.01-0.02 Ohm-cm). Electrodes were written on the substrate by standard lithographic patterning, followed by the deposition of a 20 nm Ti layer and a 180 nm Au layer by e-beam evaporation. The width of the interdigitated finger (20 fingers, 10 pairs) was 5 µm and was separated by a gap of 3 µm (Fig. 5.2(a)). Finally, electrodes were defined by using a standard lift-off technique. 3-aminopropyltriethoxy silane (APTES) was introduced to assist CNTs immobilization. Chip with patterned electrodes were cleaned sequentially with piranha solution, oxygen plasma, and UV ozone, followed by incubation with APTES (as received)

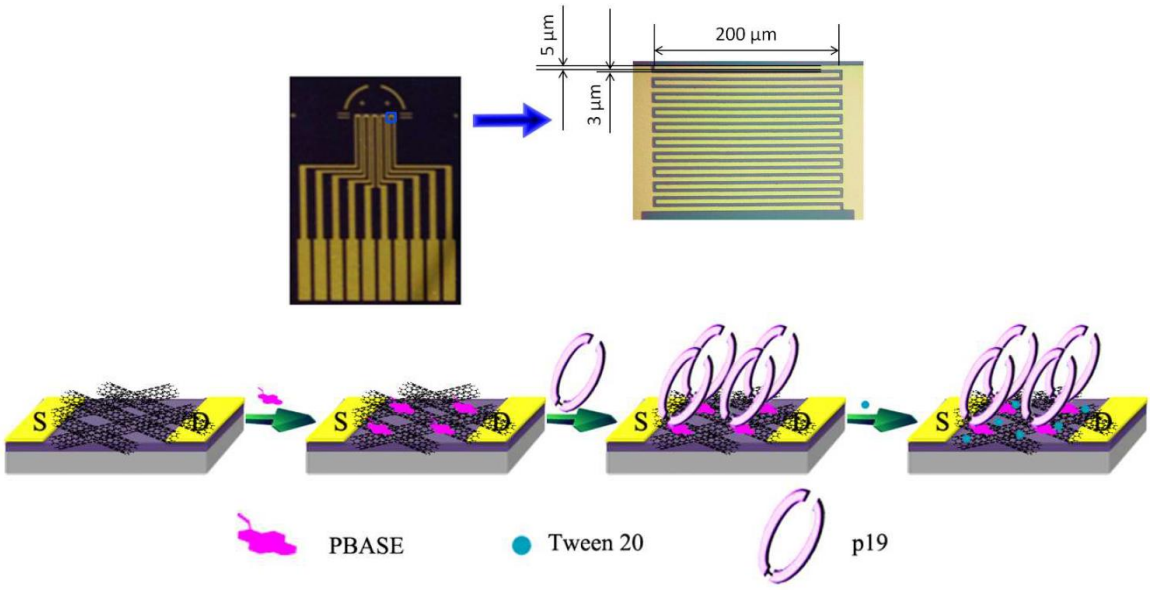

Figure 5.2 (a) Optical microscope image of microfabricated chip with 5 set of interdigitated electrodes. Each electrode has 20 fingers (10 pairs) 200 µm long, 5 µm wide separated by 3 µm gap. **(b)** Schematic of the p-19 functionalized CNTs-FET nanobiosensor fabrication.

(*Acros Organics*, 99%) for 30 min. Subsequently, CNT networks was formed by flooding the chip with 95% semiconducting pre-separated CNTs solution (*NanoIntegirs Inc.*, IsoNanotubes-S ™, 0.01 mg/ml) for 30 min, washed and finally annealed at 250°C for an hour in open air.

(b) Functionalization of CNT networks FET with p19: Chip with assembled CNT networks bridging the interdigitated electrodes was first modified with 1-Pyrenebutanoic acid succinimidyl ester (PBASE) by incubating with 10 µL of 6 mM PBASE (*Invitrogen*) in dry dimethylformamide (DMF) solutions for 30 min, washed thoroughly rinsing with PB (10 mM, pH 7.4), incubated with 10 µL of p19 (*New England BioLabs*, 2,000 units/mL) in PB (10 mM, pH 7.4) for 30 min at room temperature and thoroughly rinsing with PB (10 mM, pH 7.4). After that, devices were incubated with 0.1% Tween 20 (*BIO-RAD*) in PB (10 mM, pH 7.4) for 30 min to block any naked/bare sites on CNTs to prevent any non-specific adsorption, followed by thoroughly rinsing with PB (10 mM, pH 7.4). A schematic representation of surface functionalization steps in shown in Fig. 5.2 (b).

(c) Sensing Protocol: Samples containing RNA targets (miRNA-122a, miRNA-21, miRNA-32 or yeast total RNA) were incubated with 1 µM of miRNA-122a specific probe, 5′-pAAC ACC AUU GUC ACA CUC CAU A-3′ (complementary to miRNA-122a target) at 37˚C for 1 h in 1 10 mM pH 7.4 phosphate buffer (PB) in a total volume of 100 µL. The reaction mixture was then incubated with p19-functionalized CNTs-FET biosensor, whose initial resistance (R0) was initially measured (determined from the inverse of the slope of I-V curve between +0.2 V and -0.2 V), at room temperature for 1 h followed by removal

of unbound RNA by washing 5 times in 500 µL of PB and measuring the resistance again. A schematic representation of the miRNA sensing mechanism in shown in Fig. 5.3.

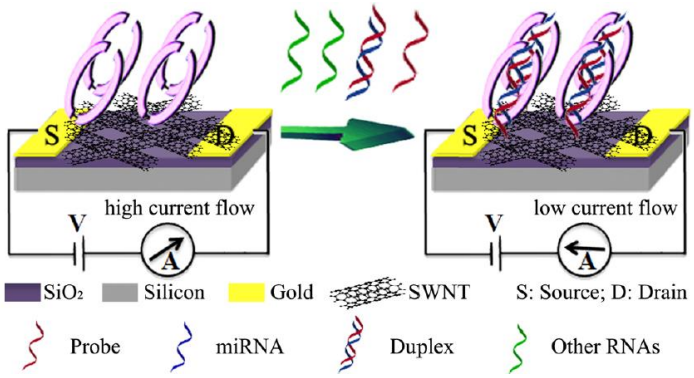

Figure 5.3 Schematic of miRNA detection principle by p-19 functionalized CNTs-FET nanobiosensor.

5.2.3. Results and Discussion

Fig. 5.4 shows an SEM image of device with the SWNTs network fabricated using the APTES-assisted assembly. The simple drop casting method resulted in a reproducible, uniform and highly dense carbon nanotube network as the sensing channel in the gap with starting resistance in the range of 3.2 ± 1.1 kΩ and ON−OFF ratios of 2.58 ± 1.02. The CNTs-FET devices were next functionalized with p19 through via PBASE as the linker molecule, and finally, the naked/bare CNTs sites were treated with Tween 20 to block nonspecific adsorption. The above fabrication steps were monitored by

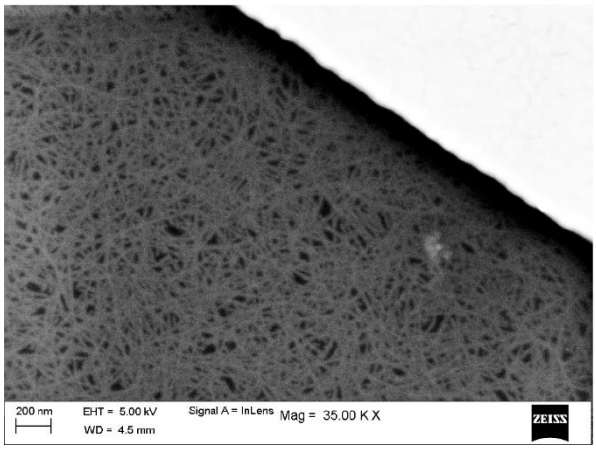

Figure 5.4 SEM image of CNT network produced by APTES-assisted assembly technique.

recording the current−voltage ($I_d - V_{ds}$) characteristics of the device between +1 and −1 V after each step by a semiconductor parameter analyzer. As shown in Fig. 5.5, the drive current in the CNTs FET device at a given voltage decreased after modification by PBASE, p19, and Tween 20. The observed current decreases or resistance increases are in accordance with the literature and are attributed to π−π stacking interaction between CNTs and pyrene in the case of PBASE and scattering potential generated and/or electron donation from the molecules to the nanotubes in the case of p19 and Tween 20.[32]

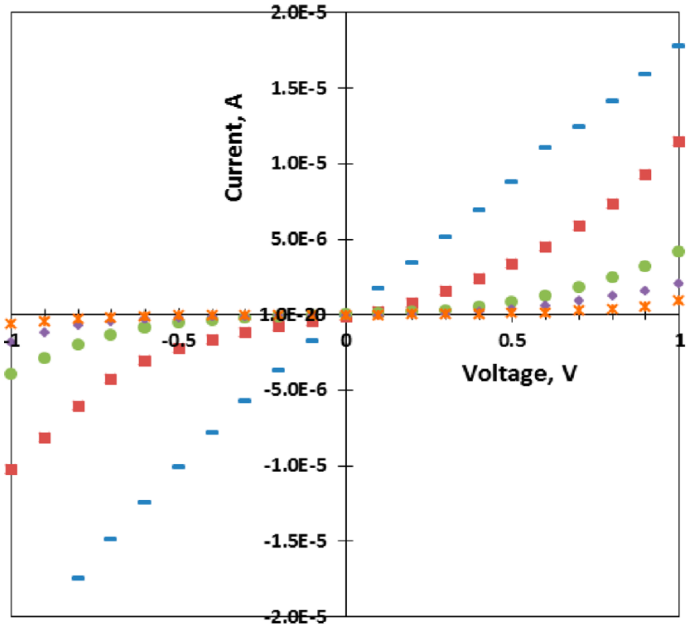

Figure 5.5 I_d−V_{ds} characteristics of the biosensor at various stages of miRNA detection. (blue −) Bare CNTs; (pink ■) CNTs functionalized with PBASE; (green circle) after p19 immobilization; (purple ◆) after blocking unoccupied sites with Tween 20; (orange ∗) 10 µL of 10 fM miRNA-122a target + 1 µM miRNA-122a probe after 1 h incubation at 37°C.

Next, we evaluated the potential of p19-functionalized CNTs-FET as miRNA nanobiosensor. Ten fM of synthetic miRNA-122a (5′-pUGG AGU GUG ACA AUG GUG UUU G-3′) was incubated with 1 µM of miRNA-122a− specific RNA probe and 5′-pAAC

ACC AUU GUC ACA CUC CAU A-3′ (complementary to miRNA-122a with two nucleotide 3′ extension) at 22˚C and 37˚C for 1 h in pH 7.4, 10 mM phosphate buffer (PB) in a total volume of 100 μL followed by incubation of 10 μL of the reaction mixture with nanobiosensor for 1 h at room temperature, washing 5 times with 500 μL of PB buffer and measuring the I−V characteristics. As illustrated in Fig. 5.5, the device current decreased (i.e., resistance increased) further, attributed to the accumulation of probe-target duplex of miRNA-122a bound to the p19 protein. The normalized resistance change calculated from the inverse of the slope of the linear range (+0.2 to −0.2 V) of the $I_d - V_{ds}$ curve was 2.22. In comparison, incubation with 1 μM of miRNA-122a target alone (positive control) produced a normalized resistance increase of only 0.015. Similarly, transistors in which CNTs were not modified with p19 but were treated with only Tween 20 to make the nanotubes hydrophilic when incubated with the probe and target mixture incubated at 37˚C for 1 h (negative controls) increased the normalized device resistance by 0.011. These results confirmed that the nanobiosensor response when incubated with the mixture of target miRNA with the probe was the result of p19 binding selectively to the hybridized duplex and thus the potential of the nanobiosensor as a specific, rapid, facile, and cost-effective analytical device for miRNA.

The effect of temperature on nucleic acid hybridization is well-established. Higher temperature leads to uncoiling of nucleic acid strands making the probe and target strands more accessible to one another, leading to improved hybridization efficiency and better specificity due to difference in the thermal stability of perfectly matched and mismatched duplexes.[33] A comparison of the sensor performance at two temperatures showed that

hybridization at 37˚C generated an enhanced signal over hybridization at 22˚C (Table 5.1), and 37˚C was selected for further studies.

After establishing the feasibility of detecting miRNA by the developed biosensor,

Table 5.1 Effect of hybridization temperature on sensor response

Log (Concentration) M	$\Delta R/R_o$	
	25˚C	37˚C
-18	0.22	0.51
-17	0.59	0.87
-16	0.96	1.22
-15	1.35	1.70
-14	2.14	2.22

we investigated its potential for quantitative detection, sensitivity, dynamic range, and limit of detection. Increasing concentrations (1 aM to 10 fM) of synthetic miRNA-122a were incubated with 1 μM of miRNA- 122a−specific RNA probe in a 100 μL total volume of PB at 37˚C for 1 h followed by incubation of 10 μL of the reaction mixture with nanobiosensor for 1 h at room temperature, washing 5 times with 500 μL of PB buffer and measuring the I−V characteristics. Fig. 5.6 shows the normalized response of the nanobiosensor [$(R - R_o)/R_o$, where R is the resistance after incubation with dsRNA and R_o is the resistance after blocking of unoccupied sites with Tween 20, determined from the inverse of the slope of the I−V curve from +0.2 to −0.2 V] as a function of log of miRNA-122a concentration. As shown in the figure, the response was linear over the range of 1 aM to 10 fM and a regression equation of $y = 0.41x + 7.85$ ($R^2 = 0.9939$) was obtained, where

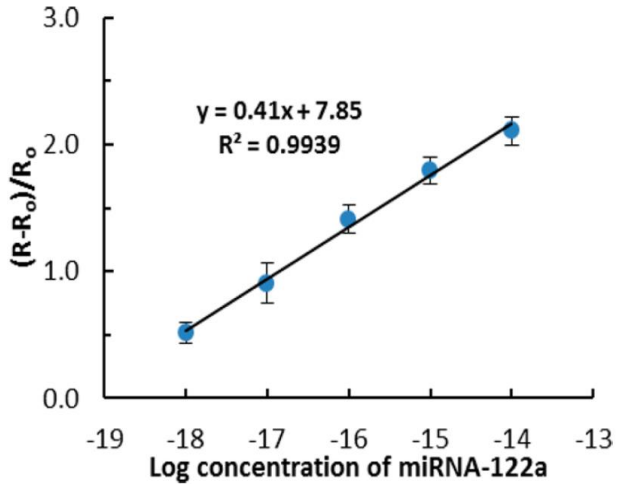

Figure 5.6 Nanobiosensor calibration for miRNA-122a in buffer. The data points are averages of measurements from 7 independent biosensors, and error bars represent ±1 standard deviation.

y is the relative change in resistance ($(R - R_o)/R_o$) and *x* is the logarithmic concentration of miRNA-122a. This detection limit is 10- to 100-fold better than other recently reported p19-based assays and sensors, some of which used labels including radioactive ^{32}P[7],[34-36] and 1000-fold better than the peptide nucleic acid probe functionalized silicon nanowire FET.[37]

For a real-world application, the nanobiosensor should be able to differentiate the target from other miRNAs and detect the target in a complex mixture. To evaluate the specificity, nanobiosensor response to the reaction mixture of 1 μM of miRNA-122a probe and 10 fM miRNA-21 (5′-pUAG CUU AUC AGA CUG AUG UUG A-3′) or miRNA-32 (5′-pUAU UGC ACA UUA CUA AGU UGC A-3′) after incubation at 37˚C for 1 h was measured. As shown in Fig. 5.7(a), both miRNAs generated an insignificant resistance change when compared to the perfect match target (miRNA-122a). Additionally, to investigate the potential of detecting the extremely low concentration of target miRNA in the presence of other nucleic acids, a calibration plot of the biosensor response as a function

of miRNA-122a concentration in the presence of 10 µg of total yeast RNA was generated following the protocol described previously. As shown in Fig. 5.7(b), the calibration plot was linear over the range of 1 aM to 10 fM and had a regression equation of $y = 0.42x + 8.08$ ($R^2 = 0.9917$). These are very similar to the analytical characteristics for the miRNA-122a analysis in buffer, showing the ability of the developed sensor to detect the target even in a large excess of other nucleic acids.

5.2.4. Conclusions

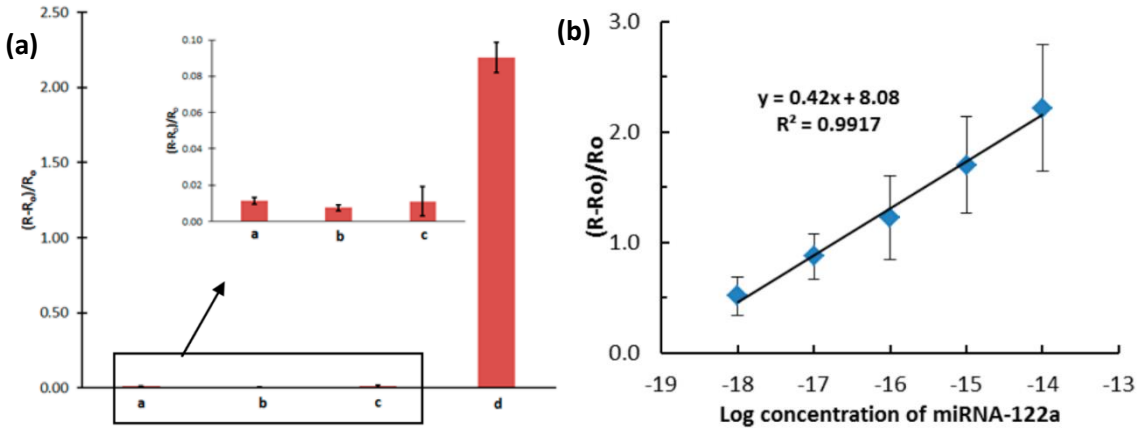

Figure 5.7 (a) Nanobiosensor selectivity. Responses of nanobiosensors to reaction mixtures of 1 µM miRNA-122a probe with (a) 10 fM miRNA-21, (b) 10 fM miRNA-32, (c) 10 µg of total yeast RNA (without miRNA- 122a target), and (d)10 fM miRNA-122a. Inset shows a magnified view. **(b)** Nanobiosensor calibration for miRNA-122a in the presence of 10 µg of total yeast RNA. The data points are averages of measurements from 10 independent biosensors, and error bars represent ±1 standard deviation.

We have developed a label-free nanobiosensor for fast, facile, inexpensive, highly specific, and ultrasensitive quantitative determination of miRNA in nucleic acid samples. The biosensor takes advantage of the high affinity and specificity of CIRV p19 protein for 21−23 nucleotide duplex RNA and the high sensitivity of CNTs-FET to quantitatively

measure as low as 1 aM to up to 10 fM of probe-specific target miRNA selectively and in a million-fold excess of other nucleic acids. Importantly, the 1 aM detection limit was achieved without employing any amplification techniques and is well below the levels of interest in biological and medical diagnostics even after diluting the sample which can further reduce any potential matrix interference. Moreover, the base mismatch discrimination can be achieved through selection of hybridization conditions, as is done in commonly employed nucleic acid detection methods. For example, by performing hybridization in a 50% formamide solution, Qavi and Bailey successfully achieved discrimination between microRNAs let- 7b and let-7c, which differ by a single-base change at position 17.[38] A similar strategy can be employed in our platform. The methodology developed in this work can be applied for fabricating an array of sensors on a single silicon substrate for multiplex sensing for miRNA expression profiling. Furthermore, the developed sensors are based on silicon microelectronics that are cheap and readily scalable to mass scale manufacturing.

5.3. An Oligonucleotide-functionalized Carbon Nanotube Chemiresistor for Sensitive Detection of Mercury in Saliva

5.3.1. Introduction

Mercury (Hg) is a toxic metal-pollutant in the environment that can exist in elemental, inorganic and/or organic forms and each form is known to have a distinct toxicity profile.[39] While the inorganic form of mercury ($HgCl_2$) is toxic to kidneys,[40] organic forms such as methylmercury are primarily neurotoxins that affect the central nervous system.[41] Methylmercury is also known to have genotoxic effects and fetal

exposure can cause intrauterine poisoning at lower exposure levels.[42] Methylmercury has a strong affinity to amino acids and eventually binds to proteins and polypeptide chains.[43] Humans are exposed to different forms of mercury due to natural causes such as off-gassing from the earth's crust and anthropogenic sources such as environmental pollution caused by industrial utilization and the use of pesticides in agricultural practices.[44] Mercury is methylated by the microorganisms present in water and bioconcentrated via the aquatic food chain.[45] This eventually results in human exposure due to the consumption of fish and contaminated water. Silver/gold-mercury amalgam dental fillings are another potential source of mercury exposure receiving scrutiny.[46] It is hypothesized that Hg^0 vapors emitted from amalgams are first converted to Hg^{2+} and then transformed to CH_3Hg^+ by oral bacteria.[47] Hence, the detection of mercury in several matrices including human saliva is an indispensable task.[48]

The commonly used techniques used for mercury detection include cold-vapor atomic absorption spectroscopy,[49] atomic fluorescence spectrometry,[50] and inductively coupled plasma spectrometry.[51] These techniques though highly sensitive and reliable have certain limitations such as complex sample preparation, use of expensive instruments, need for well-trained technicians and longer assay times. Hence, it is very important to develop a highly selective, sensitive, rapid and cost effective sensor for the detection of mercury.

To address these issues, electrochemical biosensors that incorporate a variety of bioreceptors and transducers for the detection of heavy metals have been discussed in the literature.[52,53] In particular, electrochemical biosensors based on carbon nanotubes as the transducer element have been widely used for effective, rapid and robust analysis of

environmental samples.[54,55] Owing to their high surface area to volume ratio, the electrical properties of carbon nanotubes are highly sensitive to any surface perturbations or binding events and enable label-free detection of analytes. Gong et al.[56] reported a DNA-based SWNT biosensor for label-free, selective and highly sensitive detection of Hg^{2+} using a polyT:polyA duplex functionalized SWNT. In this paper we use a similar detection scheme for the detection of both Hg^{2+} and CH_3Hg^+ in phosphate buffer and simulated saliva. A detailed detection scheme is shown in Fig. 5.8. Briefly, the SWNTs are functionalized with the capture oligonucleotide polyT, which hybridizes with polyA to form a DNA duplex. Upon exposure to mercury (Hg^{2+} and CH_3Hg^+), a structure switch occurs as the polyT:polyA duplex dehybridizes to form a T–Hg^{2+}–T complex[57,58] and polyA is released from the SWNT surface. These events lead to a change in the resistance of the

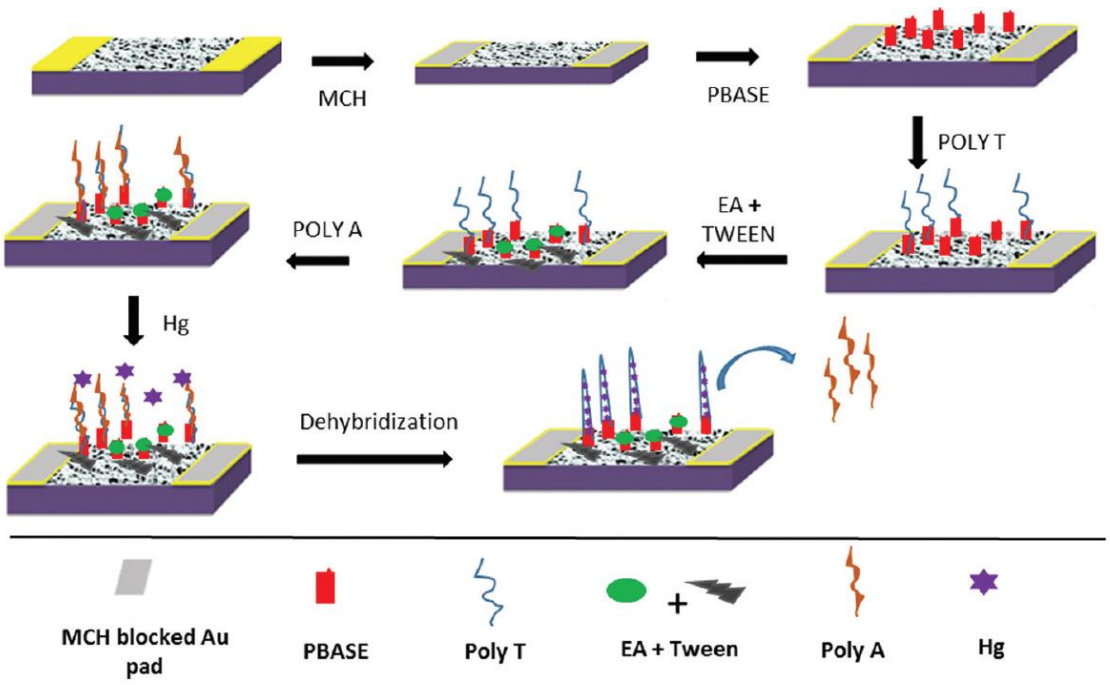

Figure 5.8 Schematic illustration of SWNT chemiresistive label-free biosensor surface functionalization and detection.

chemiresistive biosensor which is used to quantify the concentration of mercury. We demonstrate the real world application of the proposed biosensor by evaluating the performance against mercury ions spiked in simulated human saliva samples.

5.3.2. Experimental Details

(a) Device fabrication and surface functionalization: The SWNT devices were fabricated using the protocol reported by Ramnani et al.[18] Briefly, the interdigitated electrodes fabricated using standard lithography were incubated with APTES to assist uniform and dense immobilization of SWNTs on the substrate. Subsequently, the APTES functionalized chips were incubated with 50 µL of SWNT solution (0.01 mg/ml) for 30 min, followed by annealing in air at 250˚C. To prevent any non-specific binding of proteins and mercury ions to the gold pads, the SWNT functionalized chips were incubated with 2 mM MCH solution prepared in dimethylformamide (DMF) for 30 min. Next, the SWNT network was non-covalently modified with the linker molecule, PBASE (6 mM solution prepared in DMF) through π–π bond formation between pyrene and SWNTs. The PBASE-modified SWNTs were incubated overnight with 100 nM of amine-labeled polyT (5′-/5AmMC6/TTT TTT TTT TTT TTT-3′) in phosphate buffer (PB, 10 mM, pH 7.4) at 4 °C. The oligonucleotide was immobilized covalently via an amide bond between the amine at the 5′ end and the ester groups of PBASE. The device was further treated with 0.1 mM EA to block excess ester groups and 0.1% Tween 20 to prevent non-specific binding to SWNTs. Finally, the polyT captured on the SWNT surface was hybridized with polyA (5′-AAA AAA AAA AAA AAA-3′) by incubating with 100 nM polyA in PB for 2 hours at room temperature to form a DNA duplex. The above fabrication and functionalization steps

were monitored by recording the current–voltage ($I_d - V_{ds}$) characteristics of the device between −0.1 and +0.1 V after each incubation step using a CHI660 electrochemical workstation.

(b) Sensing protocol: SWNTs functionalized with the polyT:polyA duplex were incubated with increasing concentrations of Hg^{2+} and CH_3Hg^+ ion samples in PB for 30 min at room temperature. Following incubation, the chips were rinsed with PB three times to remove the unbound mercury ions and the resistance was measured by taking the inverse of the slope of the $I_d - V_{ds}$ curve from −0.1 V to +0.1 V under wet conditions, i.e. the sensing area covered with PB. A schematic of the device fabrication and sensing protocol is shown in Fig. 1. For the detection of mercury in biological samples, simulated human saliva was spiked with different concentrations of Hg^{2+}/CH_3Hg^+ and incubated on DNA-duplex-functionalized SWNTs.

(c) Simulated human saliva preparation: Simulated human saliva was prepared based on the composition reported previously.[59] The simulated saliva consisted of 0.6 g/L of sodium phosphate dibasic, 0.6 g/L of anhydrous calcium chloride, 0.4 g/L of potassium chloride, 0.4 g/L of sodium chloride, 4 g/L of mucin and 4 g/L of urea dissolved in DI water. The pH was adjusted to 7.2 and the solution was stored in the refrigerator until use.

5.3.3. Results and Discussion

The current–voltage ($I_d - V_{ds}$) characteristics were recorded after each step of surface modification during fabrication and subsequently when exposed to CH_3Hg^+ in PB for sensing. As shown in Fig. 5.9(a), the resistance of the device increased following each treatment step, i.e. MCH, PBASE, polyT, EA, Tween 20 and polyA. The increase in

resistance for the above steps is attributed to the change in the work function of gold due to the formation of Au–S bonds, π–π interaction between SWNTs and pyrene moieties in PBASE, electron donation from amine labeled polyT, EA, Tween 20 and polyA resulting in a decrease of the charge carrier concentration of the p-type SWNTs and/or electron scattering from these molecules. In the final step, the DNA duplex functionalized devices were incubated with different concentrations of CH_3Hg^+ in PB solution (10 mM, pH 7.4). Upon incubation of the DNA duplex functionalized biosensor with increasing concentrations of CH_3Hg^+ a decrease in device resistance was observed. Fig. 5.9(b) shows

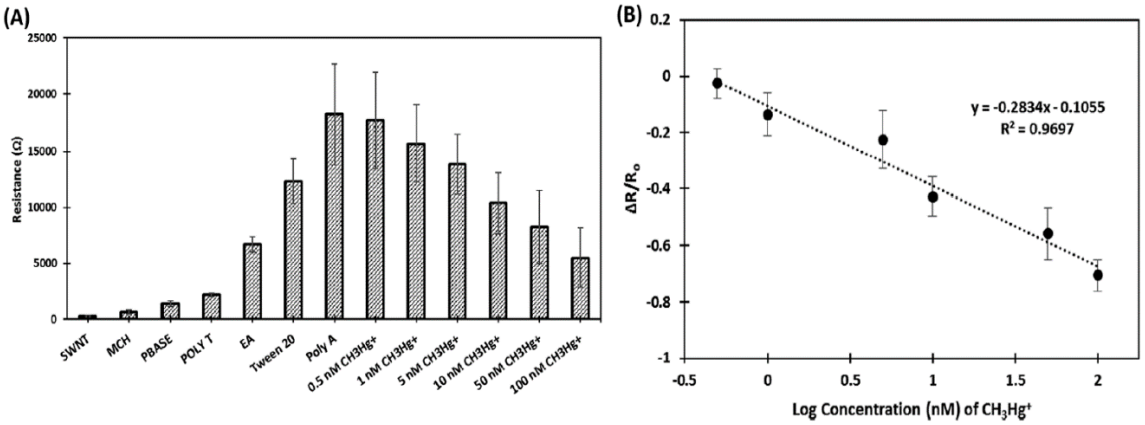

Figure 5.9 (A) Change in resistance observed after each device functionalization step and upon exposure to CH_3Hg^+; **(B)** calibration curve for detection of CH_3Hg^+ in PB. Each data point is an average of measurements from 8 independent sensors and error bars represent ±1 standard deviation.

the calibration curve, normalized change in resistance [$(R - R_o)/R_o$, where R is the resistance after incubation with CH_3Hg^+ and R_o is the resistance after hybridization between polyT and polyA] as a function of log concentration of CH_3Hg^+ (in nM). The sensor showed a linear response over the range of CH_3Hg^+ concentrations varying from 0.5 nM to 100 nM and a linear regression equation of $y = -0.2834x - 0.1055$ ($R^2 = 0.9697$)

was obtained. The biosensor sensitivity for CH_3Hg^+ was slightly higher than that for Hg^{2+} (Fig. 5.10). As shown in Fig. 5.10, a linear response was observed for Hg^{2+} concentrations varying from 1 nM to 1000 nM and a linear regression equation of $y = -0.2164x - 0.2549$ $(R^2 = 0.9145)$. Thus, the DNA-switching based biosensor responds to both mercury ions and would be suitable for measuring total mercury concentration but not for speciation of the mercury ion species. Further, the sensitivity achieved for Hg^{2+} was higher than that reported by Gong et al. due to the improved device performance resulting from the use of high purity SWNTs (95% vs. 66%) and a denser network of SWNTs obtained through APTES assisted assembly compared to the dielectrophoresis alignment method.

To verify that the change in resistance upon exposure to CH_3Hg^+ was specifically

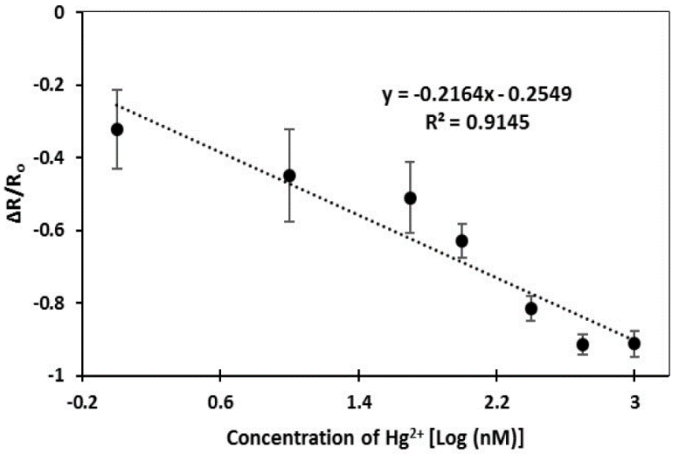

Figure 5.10 Calibration curve for detection of Hg^{2+} in PB. Each data point is an average of measurements from 8 independent sensors and error bars represent ±1 standard deviation.

due to the displacement of polyA from the polyT:polyA duplex, a control experiment was performed where the response of the polyT-functionalized SWNTs was measured for increasing concentrations of CH_3Hg^+ in the absence of polyA. As shown in Fig. 5.11,

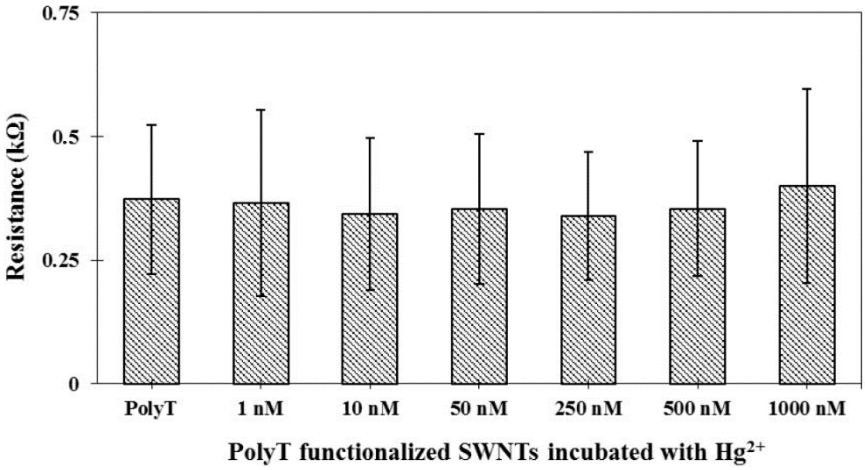

Figure 5.11 Control experiment showing response of polyT functionalized SWNTs incubated with increasing concentrations of CH_3Hg^+ in absence of polyA. Each data point is an average of measurements from 5 independent sensors and error bars represent ±1 standard deviation.

SWNTs functionalized with only the capture oligonucleotide (polyT) showed no significant changes in resistance upon incubation with CH_3Hg^+. Another control experiment was performed where the response of SWNTs to CH_3Hg^+ in the absence of polyT and polyA was measured. A negligible change in resistance with increasing CH_3Hg^+ concentrations (data not shown) confirmed the absence of any non-specific binding between SWNTs and CH_3Hg^+. These control experiments confirmed that the DNA duplex was primarily responsible for the nanobiosensor response to CH_3Hg^+. In a separate control experiment, the effectiveness of blocking of gold pads using 6-mercapto-1-hexanol (MCH) was evaluated. Without MCH treatment, the devices showed an increase in the device resistance upon exposure to CH_3Hg^+, which was attributed to CH_3Hg^+ binding to gold electrodes, changing the work function of gold. However, this non-specific binding was almost eliminated when the gold pads were blocked with MCH (Table 5.2).[60] Similar to the mechanism in the case of Hg^{2+}, the decrease in the device resistance upon incubation

with CH_3Hg^+ is hypothesized to be a result of dehybridization of the polyT:polyA duplex and subsequent release of polyA from the SWNT surface due to its binding to polyT and possibly the formation of a thymine–CH_3Hg^+–thymine duplex.

Table 5.2 Effect of mercapto-1-hexanol blocking on non-specific binding of CH_3Hg^+

	$\Delta R/R_0$ (average of 4 devices)
Response to 500 nm CH_3Hg^+ **in absence of MCH** blocking	**0.81 ± 0.24**
Response to 500 nm CH_3Hg^+ **with MCH** blocking	**0.08 ± 0.10**

Detection of mercury in simulated saliva: As discussed earlier, the most common sources of mercury poisoning among humans is via consumption of fish that contain mercury and amalgam dental fillings. Detection of mercury in body fluids such as urine, saliva and/or blood can serve as a diagnostic tool for the early detection of health issues. Although analysis of urine samples is a universally accepted diagnostic tool to assess exposures to a broad range of toxic metals particular mercury, over the recent years there has been a growing interest in the detection of disease biomarkers/ toxins in saliva due to the ease of sample collection in a noninvasive manner.[61] The use of SWNT chemiresistor based biosensors for the detection of stress biomarkers in saliva (salivary α-amylase) has been reported by our group. In this work, we evaluated the performance of our biosensor against simulated saliva samples spiked with mercury (both, Hg^{2+} and CH_3Hg^+) to demonstrate its practical application. The DNA-functionalized SWNT biosensor was tested for the detection of mercury in simulated saliva samples spiked with varying concentrations of both Hg^{2+} and CH_3Hg^+. It is critical to note that mucins, a large group of glycoprotein

molecules present in saliva, are known to non-specifically interact with nonpolar/hydrophobic surfaces. Since this non-specific adsorption is low on uncharged polar groups such as hydroxyl (–OH),[62] the blocking of gold pads using 6-mercapto-1-hexanol (MCH) makes the surface hydrophilic and alleviates the non- specific binding of mucin on gold. A negative control experiment was performed to test the response of DNA-functionalized biosensor to simulated human saliva in the absence of Hg^{2+} ions. As shown in Fig. 5.12, in the absence of Hg^{2+} ions, the response to simulated saliva was <1%, which confirms the absence of any non-specific binding of proteins. As shown in Fig. 5.13, for simulated saliva spiked with Hg^{2+} ion concentrations varying from 1 nM to 500 nM, a linear response with a regression equation of $y = -0.1342x - 0.2583$ ($R^2 = 0.9531$) and good reproducibility (evidenced by low standard deviation) was obtained. The sensitivity of 13.42% per log (nM) of Hg^{2+} was 40% lower than the sensitivity of 21.64% per log (nM)

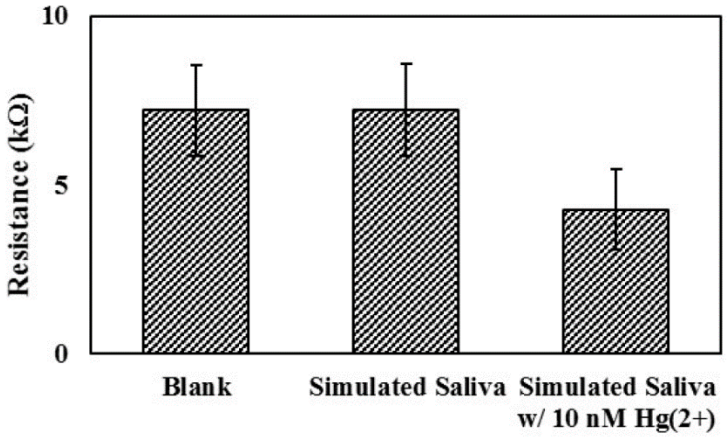

Figure 5.12 Bar graphs showing the response of biosensor to a blank sample (phosphate buffer, 10 mM, pH 7.4), simulated human saliva sample in the absence of Hg^{2+} ions and saliva sample spiked with 10 nm of Hg^{2+} ions. Each data point is an average of measurements from 5 independent sensors and error bars represent ±1 standard deviation.

of Hg^{2+} in buffer solution. Similarly, for saliva samples spiked with CH_3Hg^+ ion concentrations varying from 1 nM to 500 nM a linear regression equation of $y = -0.2481x - 0.0671$ ($R^2 = 0.9704$) was obtained. Further, the biosensors had good reproducibility. The sensitivity of 24.81% per log (nM) of CH_3Hg^+ was comparable to the sensitivity of 28.34% per log (nM) of CH_3Hg^+ in buffer solution but higher than for Hg^{2+} in saliva. These results demonstrate the high selectivity, specificity and reproducibility of the proposed biosensor which allows for detection of Hg^{2+} and CH_3Hg^+ in a complex matrix without any sample pretreatment.

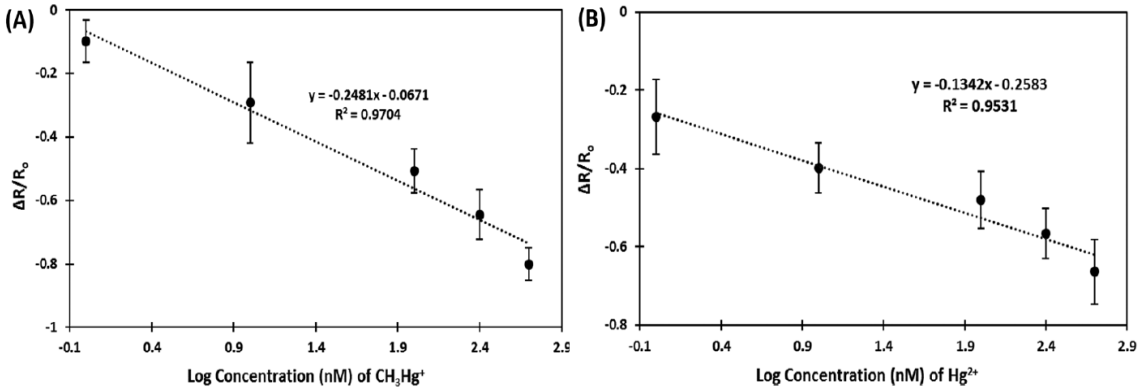

Figure 5.13 Calibration curve for detection of **(A)** CH_3Hg^+ and **(B)** Hg^{2+} in simulated human saliva. Each data point is an average of measurements from 7 (in the case of CH_3Hg^+) and 6 (in the case of Hg^{2+}) independent sensors and error bars represent ±1 standard deviation.

5.3.4. Conclusions

We have demonstrated a sensitive, selective and label-free SWNT-based chemiresistive biosensor for the facile detection of divalent mercuric (Hg^{2+}) and monomethyl mercury (CH_3Hg^+) ions in simulated saliva. The device utilizes the novel structure-switching mechanism of polyT oligonucleotides upon specific interactions with mercury ions to induce dehybridization of polyA oligonucleotides from the preformed

polyT:polyA duplexes at the SWNT surface. This structure switch causes a measureable change in device resistance which is used to quantify the mercury concentration. Overall, the biosensor exhibited good selectivity and sensitivity for CH_3Hg^+ and Hg^{2+} ions in simulated saliva with a linear detection range of 1 nM to 500 nM and a sensitivity of 24.81% and 15.68% per log (nM) of CH_3Hg^+ and Hg^{2+}, respectively. This detection strategy is the first report for the quantification of Hg ions in saliva without the use of labels while eliminating complex assay procedures. Therefore, the biosensor reported here provides a viable tool for mercury detection in biological samples.

5.4. References

1. Ferrari, Andrea C., Francesco Bonaccorso, Vladimir Fal'Ko, Konstantin S. Novoselov, Stephan Roche, Peter Bøggild, Stefano Borini et al. "Science and technology roadmap for graphene, related two-dimensional crystals, and hybrid systems." *Nanoscale* 7, no. 11 (2015): 4598-4810.
2. Bae, Sukang, Hyeongkeun Kim, Youngbin Lee, Xiangfan Xu, Jae-Sung Park, Yi Zheng, Jayakumar Balakrishnan et al. "Roll-to-roll production of 30-inch graphene films for transparent electrodes." Nature nanotechnology 5, no. 8 (2010): 574-578.
3. Withers, F., O. Del Pozo-Zamudio, A. Mishchenko, A. P. Rooney, A. Gholinia, K. Watanabe, T. Taniguchi et al. "Light-emitting diodes by band-structure engineering in van der Waals heterostructures." Nature materials 14, no. 3 (2015): 301-306.
4. Zhu, Hongwei, Jinquan Wei, Kunlin Wang, and Dehai Wu. "Applications of carbon materials in photovoltaic solar cells." *Solar Energy Materials and Solar Cells* 93, no. 9 (2009): 1461-1470.

5. Liu, Chenguang, Zhenning Yu, David Neff, Aruna Zhamu, and Bor Z. Jang. "Graphene-based supercapacitor with an ultrahigh energy density." *Nano letters* 10, no. 12 (2010): 4863-4868.
6. Wang, Xuan, Linjie Zhi, and Klaus Müllen. "Transparent, conductive graphene electrodes for dye-sensitized solar cells." *Nano letters* 8, no. 1 (2008): 323-327.
7. Shao, Yuyan, Jun Wang, Hong Wu, Jun Liu, Ilhan A. Aksay, and Yuehe Lin. "Graphene based electrochemical sensors and biosensors: a review." Electroanalysis 22, no. 10 (2010): 1027-1036.
8. Hill, Ernie W., Aravind Vijayaragahvan, and Kostya Novoselov. "Graphene sensors." IEEE sensors journal 11, no. 12 (2011): 3161-3170.
9. Ramnani, Pankaj, Nuvia M. Saucedo, and Ashok Mulchandani. "Carbon nanomaterial-based electrochemical biosensors for label-free sensing of environmental pollutants." Chemosphere 143 (2016): 85-98.
10. Tran, Thien-Toan, and Ashok Mulchandani. "Carbon nanotubes and graphene nano field-effect transistor-based biosensors." *TrAC Trends in Analytical Chemistry* 79 (2016): 222-232.
11. Sharma, Piyush Sindhu, Francis D'Souza, and Wlodzimierz Kutner. "Graphene and graphene oxide materials for chemo-and biosensing of chemical and biochemical hazards." In *Making and Exploiting Fullerenes, Graphene, and Carbon Nanotubes*, pp. 237-265. Springer Berlin Heidelberg, 2013.

12. Chua, Chun Kiang, Adriano Ambrosi, and Martin Pumera. "Graphene based nanomaterials as electrochemical detectors in Lab-on-a-chip devices." *Electrochemistry Communications* 13, no. 5 (2011): 517-519.
13. Pumera, Martin. "Graphene in biosensing." *Materials Today* 14, no. 7 (2011): 308-315.
14. Feng, Lingyan, Li Wu, and Xiaogang Qu. "New horizons for diagnostics and therapeutic applications of graphene and graphene oxide." *Advanced Materials* 25, no. 2 (2013): 168-186.
15. Ohno, Yasuhide, Kenzo Maehashi, and Kazuhiko Matsumoto. "Label-free biosensors based on aptamer-modified graphene field-effect transistors." *Journal of the American Chemical Society* 132, no. 51 (2010): 18012-18013.
16. Pumera, M., Ambrosi, A., Bonanni, A., Chng, E.L.K., Poh, H.L., 2010. Graphene for electrochemical sensing and biosensing. TrAC, Trends Anal. Chem. 29 (9), 954–965.
17. Wang, Jingfang, Shunlong Yang, Deyin Guo, Ping Yu, Dan Li, Jianshan Ye, and Lanqun Mao. "Comparative studies on electrochemical activity of graphene nanosheets and carbon nanotubes." *Electrochemistry Communications* 11, no. 10 (2009): 1892-1895.
18. Ramnani, Pankaj, Yingning Gao, Mehmet Ozsoz, and Ashok Mulchandani. "Electronic detection of microRNA at attomolar level with high specificity." *Analytical chemistry* 85, no. 17 (2013): 8061-8064.
19. Wordofa, Dawit N., Pankaj Ramnani, Thien-Toan Tran, and Ashok Mulchandani. "An oligonucleotide-functionalized carbon nanotube chemiresistor for sensitive detection of mercury in saliva." *Analyst* 141, no. 9 (2016): 2756-2760.

20. Carthew, Richard W. "Gene regulation by microRNAs." Current opinion in genetics & development 16, no. 2 (2006): 203-208.
21. Zamore, Phillip D., and Benjamin Haley. "Ribo-gnome: the big world of small RNAs." Science 309, no. 5740 (2005): 1519-1524.
22. Válóczi, Anna, Csaba Hornyik, Nóra Varga, József Burgyán, Sakari Kauppinen, and Zoltán Havelda. "Sensitive and specific detection of microRNAs by northern blot analysis using LNA-modified oligonucleotide probes." Nucleic acids research 32, no. 22 (2004): e175-e175.
23. Kloosterman, Wigard P., Erno Wienholds, Ewart de Bruijn, Sakari Kauppinen, and Ronald HA Plasterk. "In situ detection of miRNAs in animal embryos using LNA-modified oligonucleotide probes." Nature methods 3, no. 1 (2006): 27-29.
24. Várallyay, Éva, József Burgyán, and Zoltán Havelda. "MicroRNA detection by northern blotting using locked nucleic acid probes." Nature protocols 3, no. 2 (2008): 190-196.
25. Shi, Bizhi, Huamao Wang, Shengrong Guo, Yuhong Xu, Zonghai Li, and Jianren Gu. "Protein III-based single-chain antibody phage display using bacterial cells bearing an additional genome of a gene-III-lacking helper phage." BioTechniques 42, no. 6 (2007): 760.
26. Jin, Jingmin, Melissa Cid, Catherine B. Poole, and Larry A. McReynolds. "Protein mediated miRNA detection and siRNA enrichment using p19." Biotechniques 48, no. 6 (2010).

27. Vargason, Jeffrey M., György Szittya, József Burgyán, and Traci M. Tanaka Hall. "Size selective recognition of siRNA by an RNA silencing suppressor." Cell 115, no. 7 (2003): 799-811.
28. Girard, Muriel, Emmanuel Jacquemin, Arnold Munnich, Stanislas Lyonnet, and Alexandra Henrion-Caude. "miR-122, a paradigm for the role of microRNAs in the liver." Journal of hepatology 48, no. 4 (2008): 648-656.
29. Esau, Christine, Scott Davis, Susan F. Murray, Xing Xian Yu, Sanjay K. Pandey, Michael Pear, Lynnetta Watts et al. "miR-122 regulation of lipid metabolism revealed by in vivo antisense targeting." Cell metabolism 3, no. 2 (2006): 87-98.
30. Chang, Jinhong, Ju-Tao Guo, Dong Jiang, Haitao Guo, John M. Taylor, and Timothy M. Block. "Liver-specific microRNA miR-122 enhances the replication of hepatitis C virus in nonhepatic cells." Journal of virology 82, no. 16 (2008): 8215-8223.
31. Jopling, C. L., K. L. Norman, and P. Sarnow. "Positive and negative modulation of viral and cellular mRNAs by liver-specific microRNA miR-122." In Cold Spring Harbor symposia on quantitative biology, vol. 71, pp. 369-376. Cold Spring Harbor Laboratory Press, 2006.
32. Tlili, Chaker, Lakshmi N. Cella, Nosang V. Myung, Vivek Shetty, and Ashok Mulchandani. "Single-walled carbon nanotube chemoresistive label-free immunosensor for salivary stress biomarkers." Analyst 135, no. 10 (2010): 2637-2642.
33. Wallace, R. Bruce, J. Shaffer, R. F. Murphy, J. Bonner, T. Hirose, and K. Itakura. "Hybridization of synthetic oligodeoxyribonucleotides to ΦX 174 DNA: the effect of single base pair mismatch." Nucleic acids research 6, no. 11 (1979): 3543-3558.

34. Wanunu, Meni, Tali Dadosh, Vishva Ray, Jingmin Jin, Larry McReynolds, and Marija Drndić. "Rapid electronic detection of probe-specific microRNAs using thin nanopore sensors." Nature nanotechnology 5, no. 11 (2010): 807-814.
35. Labib, Mahmoud, Nasrin Khan, Shahrokh M. Ghobadloo, Jenny Cheng, John Paul Pezacki, and Maxim V. Berezovski. "Three-mode electrochemical sensing of ultralow microRNA levels." Journal of the American Chemical Society 135, no. 8 (2013): 3027-3038.
36. Khan, Nasrin, Jenny Cheng, John Paul Pezacki, and Maxim V. Berezovski. "Quantitative analysis of microRNA in blood serum with protein-facilitated affinity capillary electrophoresis." Analytical chemistry 83, no. 16 (2011): 6196-6201.
37. Zhang, Guo-Jun, Jay Huiyi Chua, Ru-Ern Chee, Ajay Agarwal, and She Mein Wong. "Label-free direct detection of MiRNAs with silicon nanowire biosensors." Biosensors and Bioelectronics 24, no. 8 (2009): 2504-2508.
38. Qavi, Abraham J., and Ryan C. Bailey. "Multiplexed Detection and Label-Free Quantitation of MicroRNAs Using Arrays of Silicon Photonic Microring Resonators." Angewandte Chemie International Edition 49, no. 27 (2010): 4608-4611.
39. Zahir, Farhana, Shamim J. Rizwi, Soghra K. Haq, and Rizwan H. Khan. "Low dose mercury toxicity and human health." Environmental toxicology and pharmacology 20, no. 2 (2005): 351-360.
40. Dieguez-Acuña, Francisco J., William W. Polk, Maureen E. Ellis, P. Lynne Simmonds, John V. Kushleika, and James S. Woods. "Nuclear factor κB activity determines the

sensitivity of kidney epithelial cells to apoptosis: implications for mercury-induced renal failure." Toxicological sciences 82, no. 1 (2004): 114-123.

41. Dolbec, J., D. Mergler, C-J. Sousa Passos, S. Sousa De Morais, and J. Lebel. "Methylmercury exposure affects motor performance of a riverine population of the Tapajos river, Brazilian Amazon." International Archives of Occupational and Environmental Health 73, no. 3 (2000): 195-203.
42. Tchounwou, Paul B., Wellington K. Ayensu, Nanuli Ninashvili, and Dwayne Sutton. "Review: Environmental exposure to mercury and its toxicopathologic implications for public health." Environmental Toxicology 18, no. 3 (2003): 149-175.
43. Dales, Loring G. "The neurotoxicity of alkyl mercury compounds." The American journal of medicine 53, no. 2 (1972): 219-232.
44. Selin, Noelle E. "Global biogeochemical cycling of mercury: a review." Annual Review of Environment and Resources 34, no. 1 (2009): 43.
45. Boening, Dean W. "Ecological effects, transport, and fate of mercury: a general review." Chemosphere 40, no. 12 (2000): 1335-1351.
46. Kodaira, Hiroe, Kohachiro Ohno, Naoko Fukase, Midori Kuroda, Shiki Adachi, Motohiro Kikuchi, and Yoshinobu Asada. "Release and systemic accumulation of heavy metals from preformed crowns used in restoration of primary teeth." Journal of oral science 55, no. 2 (2013): 161-165.
47. Pigatto, Paolo D., Claudio Minoia, Anna Ronchi, and Gianpaolo Guzzi. "Mercury in saliva and scalp hair from dental amalgam." Journal of hazardous materials 179, no. 1 (2010): 1166-1167.

48. Lemos, Valfredo Azevedo, and Liz Oliveira dos Santos. "A new method for preconcentration and determination of mercury in fish, shellfish and saliva by cold vapour atomic absorption spectrometry." Food chemistry 149 (2014): 203-207.
49. Fernandez, C., Antonio CL Conceição, R. Rial-Otero, C. Vaz, and J. L. Capelo. "Sequential flow injection analysis system on-line coupled to high intensity focused ultrasound: Green methodology for trace analysis applications as demonstrated for the determination of inorganic and total mercury in waters and urine by cold vapor atomic absorption spectrometry." Analytical chemistry 78, no. 8 (2006): 2494-2499.
50. Cai, Yong. "Speciation and analysis of mercury, arsenic, and selenium by atomic fluorescence spectrometry." TrAC Trends in Analytical Chemistry 19, no. 1 (2000): 62-66.
51. de Torres, Amparo Garcia, Jose M. Cano Pavón, and Enrique Rodriguez Castellon. "Automated on-line separation–preconcentration system for inductively coupled plasma atomic emission spectrometry and its application to mercury determination." Journal of Analytical Atomic Spectrometry 13, no. 4 (1998): 243-248.
52. Yantasee, Wassana, Yuehe Lin, Kitiya Hongsirikarn, Glen E. Fryxell, Raymond Addleman, and Charles Timchalk. "Electrochemical sensors for the detection of lead and other toxic heavy metals: the next generation of personal exposure biomonitors." Environmental Health Perspectives (2007): 1683-1690.
53. Zhou, Yaoyu, Lin Tang, Guangming Zeng, Chen Zhang, Yi Zhang, and Xia Xie. "Current progress in biosensors for heavy metal ions based on DNAzymes/DNA

molecules functionalized nanostructures: A review." Sensors and Actuators B: Chemical 223 (2016): 280-294.

54. Vashist, Sandeep Kumar, Dan Zheng, Khalid Al-Rubeaan, John HT Luong, and Fwu-Shan Sheu. "Advances in carbon nanotube based electrochemical sensors for bioanalytical applications." Biotechnology advances 29, no. 2 (2011): 169-188.
55. Sarkar, Tapan, Yingning Gao, and Ashok Mulchandani. "Carbon nanotubes-based label-free affinity sensors for environmental monitoring." Applied biochemistry and biotechnology 170, no. 5 (2013): 1011-1025.
56. Gong, Ji-Lai, Tapan Sarkar, Sushmee Badhulika, and Ashok Mulchandani. "Label-free chemiresistive biosensor for mercury (II) based on single-walled carbon nanotubes and structure-switching DNA." Applied physics letters 102, no. 1 (2013): 013701.
57. Li, Tao, Shaojun Dong, and Erkang Wang. "Label-free colorimetric detection of aqueous mercury ion (Hg2+) using Hg2+-modulated G-quadruplex-based DNAzymes." Analytical chemistry 81, no. 6 (2009): 2144-2149.
58. Tanaka, Yoshiyuki, Shuji Oda, Hiroshi Yamaguchi, Yoshinori Kondo, Chojiro Kojima, and Akira Ono. "15N-15N J-coupling across HgII: Direct observation of HgII-mediated TT base pairs in a DNA duplex." Journal of the American Chemical Society 129, no. 2 (2007): 244-245.
59. Tlili, Chaker, Lakshmi N. Cella, Nosang V. Myung, Vivek Shetty, and Ashok Mulchandani. "Single-walled carbon nanotube chemoresistive label-free immunosensor for salivary stress biomarkers." Analyst 135, no. 10 (2010): 2637-2642.

60. Tang, Xiaowu, Sarunya Bansaruntip, Nozomi Nakayama, Erhan Yenilmez, Ying-lan Chang, and Qian Wang. "Carbon nanotube DNA sensor and sensing mechanism." Nano Letters 6, no. 8 (2006): 1632-1636.
61. Wong, David T. "Salivary diagnostics." Journal of the California Dental Association 34, no. 4 (2006): 283.
62. Feldötö, Zsombor, Torbjörn Pettersson, and Andra Dedinaite. "Mucin-electrolyte interactions at the solid-liquid interface probed by QCM-D." Langmuir 24, no. 7 (2008): 3348-3357.

CHAPTER 6

Conclusions

6.1. Summary

Large-area single-crystalline graphene films with grain size >200 μm were synthesized utilizing ambient-pressure chemical vapor deposition (CVD). By using ultralow methane concentration (90 ppm) and varying growth parameters such as C/H ratio in precursor feed and duration of growth−samples with either isolated single crystals, or large-area polycrystalline films of single-layer graphene (SLG) and twisted bilayer graphene (tBLG) were synthesized using copper as a growth substrate. The quality of graphene was determined using material characterization techniques including high-resolution transmission electron microscopy (HR-TEM), electron diffraction patterns, Raman spectroscopy and x-ray photoelectron spectroscopy (XPS). Further, the extent of inter-layer coupling and twist angle-dependent vibrational properties of tBLG were analyzed using Raman spectroscopy as an experimental tool and large scale molecular dynamics simulations to study the low-frequency phonon dispersion as a function of twist angle.

In order to mitigate the issues related to high power dissipation and hot spot formation which lead to degradation of electrical performance in Si-based devices, one of the potential solutions is integration of graphene−a high thermal conductivity material−into chip design, either as the channel material, or as device interconnects. The thermal conductivity *K* of SLG films synthesized using AP-CVD was determined using opto-

thermal Raman technique. For a suspended graphene sample (size ~ 7.5 µm), the measured value of K was ~1800 W/mK. Due to scattering of phonons from grain boundaries and defects introduced during transfer process, the thermal conductivity of CVD graphene is lower than mechanically exfoliated graphene but still two orders of magnitude higher than a silicon thin-film. Further, the effects of point defects on thermal conductivity of graphene were explored. Briefly, the suspended SLG films were irradiated with low energy electron beams and Raman spectroscopy was used to quantify the density of defects ND was based on the ID/IG ratio. For the small defect densities, $N_D < 1.2 \times 10^{11}$ cm^{-2}, the thermal conductivity decreased with increasing ND. At the defect density of $N_D \sim 1.5 \times 10^{11}$ cm^{-2}, one can see an intriguing saturation behavior was observed. The saturation behavior was explained by presence of single and double vacancy type defects using MD simulations and confirmed based on the $I_D/I_{D'}$ peak ratio.

The electrical properties including sheet resistance, carrier mobility and I_{ON}/I_{OFF} ratio of CVD grown SLG were studied by fabrication of large-area graphene field-effect transistors (FETs). The transfer characteristics exhibited ambi-polar electric field effect with carrier mobilities of ~2000 cm^2/Vs and V_{cnp} shifted to positive voltages (15-20 V), indicating p-doped nature of as-grown SLG. The I_{ON}/I_{OFF} ratio was negligible (~2) due to the absence of a bandgap. Graphene nanoribbons (GNR) were fabricated using two different top-down techniques to engineer a bandgap in graphene. GNR-FET devices fabricating using electron-beam lithography (EBL) resulted in an array of ribbons of widths between 60-200 nm. Since FET-based applications require nanopatterning down to sub-10 nm, the I_{ON}/I_{OFF} ratio of the GNR-FET with ribbon width of 60 nm was found to be low

(~4). A novel technique for nanopatterning ribbons with widths from 8-20 nm was developed using superlattice nanowire pattern (SNAP) transfer process. Briefly, an array of Pt NWs was fabricated to act like an etch mask and graphene was etched using RIE. The preliminary attempts, though promising, were not successful and require optimization of device fabrication steps. The edge defects in GNRs which are introduced during the RIE process, and are responsible for degradation of carrier mobility and increase in off-state current, were characterized using Raman spectroscopy and x-ray photoelectron spectroscopy. Thermal annealing treatment was used to reduce the concentration of these defects. Finally, the fabricated GNR-FET device was used as a gas sensor for dynamic sensing of NO_2 gas. The GNR-FET showed a significant increase in sensitivity compared to its graphene counterpart.

Analogous to GNRs, semiconducting single-walled carbon nanotubes (SWNTs) were used to fabricate FET/chemiresistive-based electrical nano chemical/bio-sensors. Using microRNA-122a−a biomarker for liver cancer−as the model target, a SWNT biosensor was developed using a p19 protein as the receptor for label-free electrical detection of microRNAs. The sensor was able to detect microRNA concentrations from 1 aM to 10 fM in the presence of a million-fold excess of total RNA and other miRNA sequences. A similar chemiresistive biosensor was developed for sensitive, selective and facile detection of divalent mercuric (Hg^{2+}) and monomethyl mercury (CH_3Hg^+) ions in simulated saliva. The detection mechanism was based on structure-switching of polyT oligonucleotides upon specific interactions with mercury ions to induce dehybridization of polyA oligonucleotides from a preformed polyT:polyA duplexes at the SWNT surface. The

biosensor exhibited good selectivity and sensitivity for CH_3Hg^+ and Hg^{2+} ions in simulated saliva with a linear detection range of 1 nM to 500 nM.

6.2. Suggestions for future work

The absence of a bandgap in graphene is a serious limitation which limits its potential applications as a channel material in field-effect transistors. Bandgap engineering of graphene requires nanopatterning down to sub-10 nm, which is extremely challenging with conventional techniques. The SNAP process discussed in this dissertation is a promising solution for fabrication of GNR arrays with narrow widths. However, this process still requires optimization of the device fabrication steps including deposition of a uniformly thin (~10 nm) layer of epoxy on a substrate and removal of graphene between Pt NWs using anisotropic etching. In particular, the etching of graphene is a critical step since it introduces defects along the edges of the GNR. These defects are responsible for degradation of carrier mobility and large currents in off-state. Most plasma etching methods rely on O_2-based RIE, which leads to functionalization of edge carbon atoms with oxygen-functional groups. Studies have shown that etching based on hydrogenation/fluorination techniques leads to GNRs with significantly lesser edge roughness and higher I_{ON}/I_{OFF} ratios of devices.

Apart from graphene, there is a large library of two-dimensional (2D) van der Waals (vdW) materials including transition metal dichalcogenides (TMDs) and hexagonal boron nitride (h-BN), that have gathered increasing interests in the research community owing to their intriguing electrical and optical properties. TMDs, chemically abbreviated as MX_2, where M is a transition metal (Mo, W, etc.) and X is a chalcogen (S, Se, Te, etc.),

exhibit a wide range of electrical properties from insulating or semi-conducting to metallic depending upon the crystalline phase. One such TMD that has attracted significant interest is molybdenum disulfide (MoS_2), which exhibits an indirect band gap of 1.2 eV in its bulk state but transitions to a direct band gap of 1.8 eV for single-layer MoS_2. Due to this sizable band gap, field-effect transistors (FETs) fabricated with MoS_2 as the channel exhibit high on/off ratios in the range of 10^4-10^6 and very low power consumption in static mode. However, MoS_2 by itself may not be ideal for digital applications due to low carrier mobility (~1−100 cm^2/Vs). Additionally, due to the presence of a high Schottky barrier between metal-MoS_2 contacts, the transport in channel is dominated by high contact resistance. These issues can be overcome by fabricating graphene−MoS_2 heterostructures that can utilize the superior properties of the individual materials such as high carrier mobility from graphene, sizable band gap from MoS_2 and eliminating Schottky contacts due to tunable work function of graphene. Thus, by artificially stacking different vdW materials, the properties of the resultant heterostructure can be tailored for desired applications. Such vdW heterostructures have been explored for a wide range of applications including thin film transistors (TFTs), flexible electronic devices, photovoltaics, light emitting diodes (LEDs), photodetectors and sensors.

APPENDIX A

Phonon dispersion in twisted bilayer graphene: Molecular Dynamics simulations

The tBLG supercell (i.e. the primitive cell of the commensurate twisted bilayer graphene) was constructed as described in ref. 1. A commensurate unit cell with twist angle, θ=9° is shown in Fig. 1. We performed a systematic study of the phonon dispersion and density of modes (DOM) of tBLG, as a function of twist angle, θ, using an anharmonic MD method as implemented in LAMMPS (Large-scale Atomic/Molecular Massively Parallel Simulator) using suitable interaction parameters.[1] All of the MD simulations were performed within the framework of the isothermal-isobaric ensemble (NPT), with a fixed number of atoms N, constant pressure P, constant temperature T, and a time step of 0.8 femtosecond (fs). Periodic boundary conditions were applied in all directions and the crystal was initially equilibrated at a predefined temperature via a velocity scaling routine. Prior to sampling the dynamical matrix, all simulations ran for 200,000 time steps using a

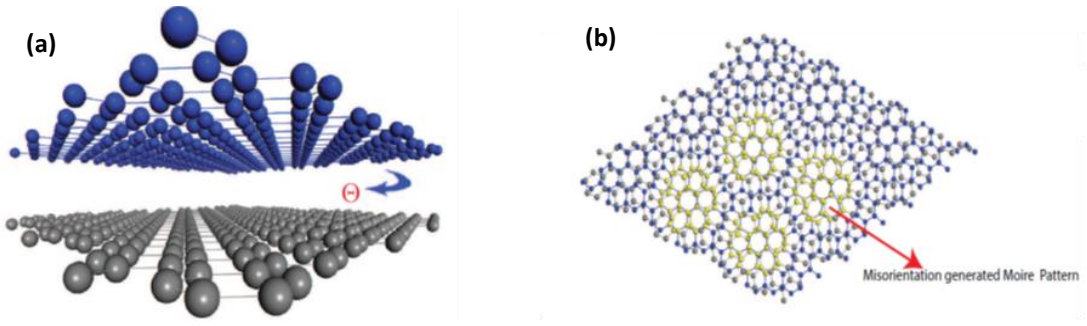

Figure 1. (a) Simulated models of twisted bilayer graphene (tBLG) system; **(b)** Top view of tBLG system illustrating Moire pattern

Noose-Hoover thermostat under NPT ensemble at 300K. Pressure was maintained at 1 bar. Following equilibration, constant number, volume, and energy (NVE) integration was performed along with the application of a Langevin thermostat. The dynamical matrix was then sampled 500,000 times at intervals of 5 time steps. The friction and random force provided by the Langevin thermostat allowed for faster convergence of the dispersion relations, although comparable results were achieved with longer NVE simulations without a Langevin thermostat.

Since the quality of phonon frequencies depends on the in-plane and out-of-plane C-C interactions, the potentials defining these interactions need a systematic validation. In order to identify suitable force field that could describe both the interactions, we calculated phonon dispersions for a SLG and a BLG using Tersoff,[2] adaptive intermolecular reactive bond order (AIREBO),[3] and long-range carbon bond order potential (LCBOP),[4] and compare them with the more accurate but computationally expensive first principle methods.[5] Since one of the objectives of this study is to reproduce and provide some theoretical understanding of experimentally observed G-peak of tBLG, the potential verification is focused at optical frequencies at around G point of BZ. In general, all three potentials produce qualitatively similar phonon spectra for a SLG. However, the Tersoff potential overestimates the maximum optical frequencies (TO and LO) at zone-center G by 35% when compared to the first principle calculation. The discrepancies in the optical frequencies is mainly due to the use of parameters that are reproduced by fitting the bulk modulus of graphite, while ignoring long-range interactions. Similar limitation of this potential was also identified during a recent study, where the temperature dependent

phonon dispersion and transport was compared against experiment and first principle calculations.[6] AIREBO potential also overestimates the maximum optical frequencies (TO and LO) at G-zone center, though only by 30%. Although AIREBO is an extension of the Tersoff potential, this potential does include torsional interaction.[4] The incapability of early BOPs to properly describe multilayer graphitic materials was noted by Los and Fasolino.[7]

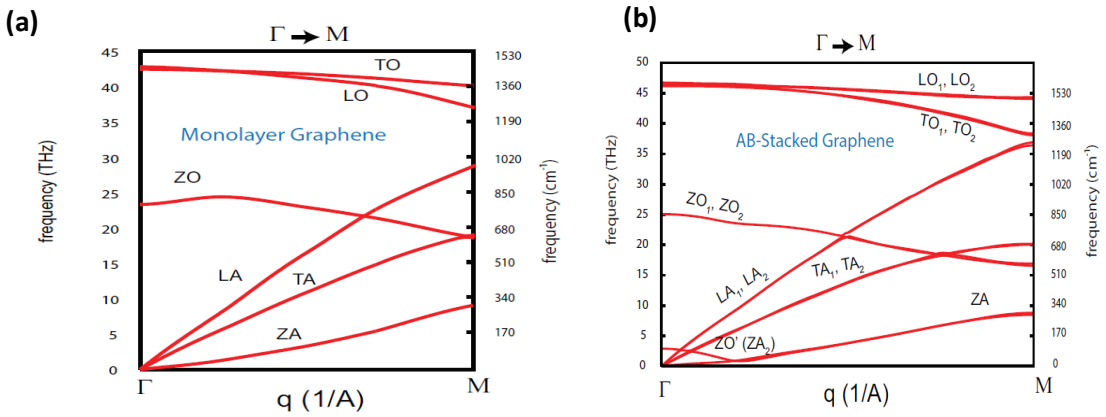

Figure 2 Numerically calculated phonon dispersion for **(a)** single layer graphene (SLG), and **(b)** AB-stacked bilayer graphene system.

However, the maximum optical frequencies obtained by LCBOP potentials (1450 cm^{-1}) are only off by 9%, as compared to the experimentally observed maximum optical frequency (1600 cm^{-1}), as shown in Fig. 2(a). LCBOP is an appropriately parameterized mix of a short-range Brenner-like bond order potential and a long-range radial potential [4]. The inclusion of long-range interactions provides a good description of the interlayer properties over a range of interlayer distances, as compared to experimental and/or ab-initio data. Since the parameters for the LCBOP potential were initially parameterized for the interlayer interaction over the range of interlayer distances in a graphitic system, this could also provide an adequate description of the modulating vdW-gap in the tBLG system

[8, 9]. To validate this, we have calculated the phonon dispersion of an AB-stacked graphene bilayer system using this potential, as shown in Fig. 2(b). All the phonon modes, including degenerate modes in AB-stacked bilayer system, are labelled accordingly. As in the SLG phonon dispersion, LO/TO modes are optical modes, and LA/TA modes are acoustic modes.

With a finite twist angle θ, the tBLG unit cell size increases. Consequently, the total number of phonon modes increases by a factor of 3N, where N is the number of atoms in the commensurate unit cell. Increasing the size of the unit cell adds to the complexity of the dispersion curves due to the folded phonon spectrum at the Γ point of the BZ. The relative twist or misorientation between the graphene layers influences the phonon spectra of tBLG owing to two reasons: (i) modification of the weak van der Waals interlayer interaction and (ii) alteration of BZ size leading to phonon momentum change. To gain an initial understanding of misorientation on the phonon frequencies, we consider the smallest tBLG supercell consisting of 28 atoms, which occurs when the top and bottom layers are misoriented with a relative θ=21.78° (Fig. 3). To separate the effect of misorientation from

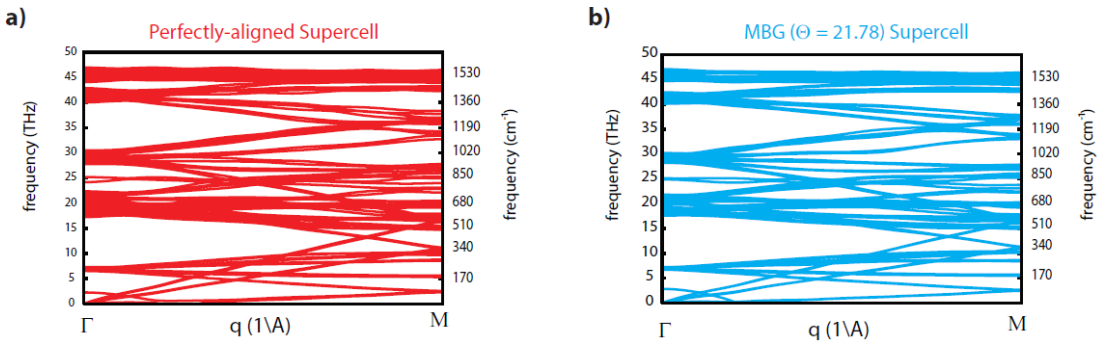

Figure 3 Numerically calculated phonon dispersion for **(a)** perfectly aligned supercell, and **(b)** tBLG (θ = 21.78°) with the equal number of lattice sites.

the effect of increased unit cell size, we calculated the phonon dispersion of AB-stacked graphene using the same supercell as that of the θ=21.78° tBLG. The two ω-q dispersions are shown side-by-side in Fig. 3. Qualitatively, there is little difference between the two sets of dispersions. Quantitatively, the ZO' mode frequency for the tBLG slightly decreases by 1.9 cm^{-1} compared to that of the AB-aligned supercell.

References

1. Plimpton S. 1995 *J. Comput. Phys.* 117 1-19.
2. Tersoff J. 1988 *Phys. Rev. B* 37 6991.
3. Stuart S J, Tutein A B and Harrison J A 2000 *J. Chem. Phys.* 112 6472-86.
4. Los J H and Fasolino A 2003 *Phys. Rev. B* 68 024107.
5. Giannozzi P, Baroni S, Bonini N, Calandra M, Car R, Cavazzoni C, Ceresoi D, Cococcioni G L, Dabo I and Dal Corso A 2009 *J. Phys. Condens. Matter*. 21 395502.
6. English T S, Kenny T W, Smoyer J L, Baker C H, Le N Q, J. C. Duda, Norris P M and Hopkins P E 2012 *InASME 2012 Heat Transfer Summer Conference collocated with the ASME 2012 Fluids Engineering Division Summer Meeting and the ASME 2012 10th International Conference on Nanochannels, Microchannels, and Minichannels* 617-24.
7. Los J H and Fasolino A 2002 *Comput. Phys. Commun.* 147 178-81.
8. Neupane M R 2015 *Ph. D. Thesis, University of California, Riverside*.
9. Elder R M, Neupane M R and Chantawansri T L 2015 *Appl. Phys. Lett.* 107 073101.

APPENDIX B

Thermal conductivity dependence on defect density: Molecular Dynamics simulations

Boltzmann transport equation approach

In order to analyze the experimental data, we used the BTE approach with the relaxation time approximation. In the framework of this BTE–RTA approach the thermal conductivity can be written as:[1,2]

$$K_{\mathrm{G}} = \frac{1}{4\pi k_{\mathrm{B}} T^2 h} \sum_{s=\mathrm{LA,TA,ZA}} \int_0^{q_{\max}} \left\{ \left[\hbar\omega_s(q) \frac{\mathrm{d}\omega_s(q)}{\mathrm{d}q} \right]^2 \tau_{\mathrm{tot}}(s,q) \times \frac{\exp[\hbar\omega_s(q)/k_{\mathrm{B}}T]}{[\exp[\hbar\omega_s(q)/k_{\mathrm{B}}T]-1]^2} q \right\} \mathrm{d}q$$

where h = 0.335 nm is the graphene layer thickness, and the summation is performed over all acoustic phonon branches s = LA, TA or ZA, ω_s is the phonon frequency of the s-th phonon branch, q is the phonon wave number, $\tau_{tot}(s,q)$ is the total phonon relaxation time, T is the absolute temperature, $\hbar$ and k_B are Plank's and Boltzmann's constant, respectively. The scattering rates for the three main phonon relaxation processes, phonon–phonon Umklapp (U) scattering, phonon – rough-edge scattering (B) and phonon – point-defect (PD) scattering, are given by:

$$1/\tau_{\mathrm{B}}(s,q) = (\nu_s/L)((1-p)/(1+p)),$$
$$1/\tau_{\mathrm{PD}}(s,q) = S_0 \Gamma q_s {\omega_s}^2/(4\nu_s),$$
$$\tau_{\mathrm{U},s} = \frac{1}{{\gamma_s}^2} \frac{M{\nu_s}^2}{k_{\mathrm{B}}T} \frac{\omega_{s,\max}}{\omega^2}.$$

Here $v_s = d\omega_s/dq$ is the phonon group velocity, p is the specularity parameter introduced above, S is the surface per atom, $\omega_{s,max}$ is the maximum cut-off frequency for a given branch, γ_s is an average Gruneisen parameter of the branch s, M is the mass of an unit cell, $\Gamma = \zeta(N_D/N_G)$ is the measure of the strength of the point defect scattering and $N_G = 3.8 \times 10^{15}$ cm^{-2} is the concentration of carbon atoms.

Molecular dynamics

Simulations are performed on a pristine graphene sheet of size 319.5 nm × 54.1 nm containing 660 000 carbon (C) atoms. Defects (single and double vacancies) are introduced in the structure by randomly selecting and removing carbon atoms. The C–C interactions are described using the optimized Tersoff potential for thermal transport in graphene.[3] Periodic boundary conditions are employed in all directions. The simulations are carried out with the LAMMPS package.[4] The graphene structure is energy minimized and subsequently simulated under the isothermal–isobaric (NPT) ensemble using the Nose–Hoover thermostat at 300 K and barostat at 0 MPa for 4 ns, followed by equilibration in canonical (NVT) ensemble for 4 ns using the Nose–Hoover thermostat at 300 K. The coupling time for thermostats are 0.1 ps and that for barostat is 1 ps. The thermodynamic constraints are removed and the structure is simulated under the microcanonical (NVE) ensemble for 3 ns to ensure equilibration. Subsequently, thermal conductivity is computed using the reverse non-equilibrium MD technique.[5,6] The time step of integration used in all the simulations is 1 fs.

References

1. D. L. Nika, E. P. Pokatilov, A. S. Askerov and A. A. Balandin, Phys. Rev. B: Condens. Matter, 2009, 79(15), 155413.
2. D. L. Nika, S. Ghosh, E. P. Pokatilov and A. A. Balandin, Appl. Phys. Lett., 2009, 94(20), 203103.
3. L. Lindsay and D. A. Broido, Phys. Rev. B: Condens. Matter, 2010, 81(20), 205441.
4. S. J. Plimpton, Comput. Phys., 1995, 117(1), 1–19.
5. F. Müller-Plathe, J. Chem. Phys., 1997, 106(14), 6082–6085.
6. G. Balasubramanian, I. K. Puri, M. C. Böhm and F. Leroy, Nanoscale, 2011, 3(9), 3714–3720.